NASA/CR–2014-218510

Investigation of Advanced Radar Techniques for Atmospheric Hazard Detection with Airborne Weather Radar

Andrew L. Pazmany
ProSensing, Inc., Amherst, Massachusetts

August 2014

NASA STI Program . . . in Profile

Since its founding, NASA has been dedicated to the advancement of aeronautics and space science. The NASA scientific and technical information (STI) program plays a key part in helping NASA maintain this important role.

The NASA STI program operates under the auspices of the Agency Chief Information Officer. It collects, organizes, provides for archiving, and disseminates NASA's STI. The NASA STI program provides access to the NASA Aeronautics and Space Database and its public interface, the NASA Technical Report Server, thus providing one of the largest collections of aeronautical and space science STI in the world. Results are published in both non-NASA channels and by NASA in the NASA STI Report Series, which includes the following report types:

- TECHNICAL PUBLICATION. Reports of completed research or a major significant phase of research that present the results of NASA Programs and include extensive data or theoretical analysis. Includes compilations of significant scientific and technical data and information deemed to be of continuing reference value. NASA counterpart of peer-reviewed formal professional papers, but having less stringent limitations on manuscript length and extent of graphic presentations.

- TECHNICAL MEMORANDUM. Scientific and technical findings that are preliminary or of specialized interest, e.g., quick release reports, working papers, and bibliographies that contain minimal annotation. Does not contain extensive analysis.

- CONTRACTOR REPORT. Scientific and technical findings by NASA-sponsored contractors and grantees.

- CONFERENCE PUBLICATION. Collected papers from scientific and technical conferences, symposia, seminars, or other meetings sponsored or co-sponsored by NASA.

- SPECIAL PUBLICATION. Scientific, technical, or historical information from NASA programs, projects, and missions, often concerned with subjects having substantial public interest.

- TECHNICAL TRANSLATION. English-language translations of foreign scientific and technical material pertinent to NASA's mission.

Specialized services also include organizing and publishing research results, distributing specialized research announcements and feeds, providing information desk and personal search support, and enabling data exchange services.

For more information about the NASA STI program, see the following:

- Access the NASA STI program home page at *http://www.sti.nasa.gov*

- E-mail your question to help@sti.nasa.gov

- Fax your question to the NASA STI Information Desk at 443-757-5803

- Phone the NASA STI Information Desk at 443-757-5802

- Write to:
  STI Information Desk
  NASA Center for AeroSpace Information
  7115 Standard Drive
  Hanover, MD 21076-1320

NASA/CR–2014-218510

Investigation of Advanced Radar Techniques for Atmospheric Hazard Detection with Airborne Weather Radar

Andrew L. Pazmany
ProSensing, Inc., Amherst, Massachusetts

National Aeronautics and
Space Administration

Langley Research Center
Hampton, Virginia 23681-2199

Prepared for Langley Research Center
under Contract NNL12AA44C

August 2014

Available from:

NASA Center for AeroSpace Information
7115 Standard Drive
Hanover, MD 21076-1320
443-757-5802

Contents

Contents

INVESTIGATION OF ADVANCED HAZARD DETECTION CAPABILITIES WITH MULTIFREQUENCY RADAR

Andrew L. Pazmany, Ph.D.
ProSensing Inc., Amherst, MA

EXECUTIVE SUMMARY

Current state of the art Aircraft Weather Radars (AWRs) are scanning, X-band, single polarization (H-pol) and coherent with Doppler measurement capability. The measured radar parameters include reflectivity and Doppler velocity mean and standard deviation. The X-band (~9.4 GHz) operating frequency offers the optimum compromise between available transmit power, antenna gain with a moderate size aperture, receiver sensitivity (front-end losses and LNA noise figure) and acceptable attenuation in moderate liquid precipitation. The Doppler velocity standard deviation measurements are effective in identifying turbulence in precipitation.
However, current X-band AWRs have the following shortcomings:

1. Insufficient sensitivity in low reflectivity hazard conditions, such as:
    a. Super-cooled, high liquid water content drizzle and clouds.
    b. High ice water content, high altitude clouds.
2. Inability to correct for rain attenuation, resulting the under estimation of severe weather cores.
3. Limited measurement range in highly attenuating heavy liquid precipitation.

There are several possible design options that can be considered in the next generation of AWRs, but unfortunately there is no single design solution to improve detection in all the above listed hazard conditions. The following are the recommendations of this report, in order of increasing complexity and cost.

Recommendation #1: Add Radiometer Measurement Capability to AWRs
The addition of radiometric measurement capability to future AWRs should cost very little and can have potentially significant impact on detecting and avoiding inflight icing hazard, especially in super-cooled liquid clouds and drizzle that are often below the detection threshold of AWRs. The radiometric brightness temperature measurements can be used directly to identify the "coolest" direction with the least amount of liquid water path. Or if some assumptions can be made on drop size distribution (e.g., stratified precipitation), the radiometer measurements can be combined with the radar reflectivity profiles to quantify some cloud and precipitation parameters and thus the potential hazard.

Recommendation #2: Support the Development of Dual-Polarized AWR Antennas to Enable Polarimetric Measurement Capability

The use of polarimetry for characterizing precipitation (rain rate) and severe weather (hail detection) and correcting for attenuation has been well documented ([1-8]). The cost of upgrading the current AWRs to dual-polarized capability is relatively simple and inexpensive. The transmitted pulse has to be equally divided to the Vertical and Horizontally polarized antenna ports and a second receiver has to be added to the radar. The signal processing is computationally modest and polarimetric radar parameters, such as differential reflectivity (Zdr) and specific differential phase shift (Kdp) can be effectively used to correct for attenuation in moderate to heavy rain conditions. The only missing (enabling) technology is a dual-pol antenna, similar in quality to the current standard flat plate waveguide array.

Recommendation #3: Develop Dual-Frequency (X/C-band) AWRs for Severe Weather Prone Regions

In severe weather conditions X-band attenuation can be severe, resulting in underestimating dangerous weather cores, and worse, diminishing the received signal below the detectable threshold. By shifting to a lower frequency, attenuation quickly decreases and thus improves the probability of detection. A dual-frequency X/C-band system would have the higher sensitivity to smaller scatterers at X-band but the ability to penetrate highly attenuating (high rain rate) regions.

1 Introduction

Most AWRs (aircraft weather radars) operate at X-band (8-12 GHz) using magnetron tube or solid state amplifier transmitters and slotted waveguide array antennas. These X-band radars provide an optimal tradeoff between sensitivity, size, weight and cost, but are susceptible to severe attenuation in heavy rain and have limited or no ability to help pilots detect and quantify icing potential. This vulnerability of AWRs to attenuation and their inability to characterize and quantify precipitation has been a contributing factor in numerous aircraft incidents.

Undetected peak convective cells, hidden by attenuation, led to the forced landing and resulting fatalities of Southern Airways flight 242 on April 4, 1977. If attenuation information was available from AWR, or if the radar signal was less attenuated, the peak convective region would have been correctly identified and likely avoided. Newer AWRs with Doppler capability attempt to work around this attenuation problem by measuring the radar signal spectrum width. Hazardous convective severe weather cores are almost always highly turbulent and thus cause a broadening of the Doppler signal spectrum. Furthermore spectrum width measurements are theoretically unbiased by attenuation, as long as the received signal is above the detection threshold. So the spectrum width technique can effectively detect convective severe weather, but attenuation can still diminish measurement range to impractically short distances. Since attenuation of atmospheric water droplets is approximately proportional to the square of the radar frequency, a potential solution to severe attenuation is multi-frequency AWR with a lower frequency channel. A second radar channel at C-band for example, would have a significantly lower rate of attenuation in heavy rain than at X-band, and consequently could better penetrate and more reliably detect severe weather. The multi-frequency radar technique is investigated in Section 4. Other methods to improve measurement sensitivity are discussed in Section 5.

Some hazardous atmospheric conditions however do not have elevated turbulence or wind sheer, and radar backscatter intensity is not necessarily a good metric of hazard potential, such as freezing drizzle and rain. On October 31, 1993, undetected or under estimated freezing rain caused the crash of American Eagle flight 4184. Other icing related aircraft incidents are listed in http://www.skybrary.aero/index.php/In-Flight_Icing. Icing hazard potential is related to the total volume of supercooled liquid along the flight path and drop size (larger drops can cause enhanced surface roughness and can have larger areas of impingement, sometimes beyond the ice protection system). A technique not yet utilized with AWRs for better measurement of severe weather precipitation or freezing rain is radar polarimetry. The quantitative measurement of rain with S-band (~ 3 GHz) polarimetric ground-based weather radars was successfully developed in the 1990s and by 2010 the polarimetric upgrade of the US network of 159 ground-based weather radars began and is scheduled to be completed by the end of 2013 [1][2]. Moreover, new ground based radars are almost never built without polarimetric measurement capability. The initial low-frequency polarimetric rain retrieval techniques have been modified and validated for C and X-band [10] [15], but have not yet

been implemented with AWRs. One of the recommendations of this report is to upgrade future AWRs with polarimetric measurement capability for better characterization of rain in convective severe thunderstorms and in freezing rain. Weather radar polarimetry and its implementation with AWRs are discussed in Section 3.

Supercooled clouds and drizzle can contain a large amount of liquid water comprised of small droplets, making them undetectable by most weather radars, yet still an icing threat to smaller aircraft. Higher frequency radars have better sensitivity to small droplets but also have a higher rate of attenuation in high liquid water conditions, making them actually less sensitive at the ranges that are needed from an aircraft, than the current X-band AWRs (see Section 0). Radiometers however have been effectively used to measure drizzle and cloud liquid for many decades and AWRs already have a receiver that can be used for brightness temperature measurements. This "passive", receive-only measurement concept involves scanning ahead of the aircraft in azimuth while pointing in elevation above the horizon. The observed brightness temperature (or measured noise power) is the attenuation weighted, physical temperature along the antenna beam can be approximated as (see Eq. (5))

$$T_B \approx T_{eff}\left[1-e^{-4.34\alpha_T}\right] \quad \textbf{(1)}$$

where

α_T is the total atmospheric attenuation along the antenna beam in dB, and

T_{eff} is the effective physical temperature of the attenuating cloud or precipitation layer.

Since microwave attenuation due to small (relative to the wavelength) water droplets is directly proportional to the total liquid water, when the total liquid water along the beam is low, very low brightness temperature would be observed. If the total attenuation is high, the radiometer measurement will saturate, observing the physical temperature of the cloud or precipitation. But the total path attenuation can be controlled to some degree by pointing the beam up in elevation, to cut through a highly attenuating region at a steeper angle, thereby reducing the attenuating distance, and thus reduce the chance of saturation (Figure 1). If the propagation length through the cloud or precipitation can be approximated, then the average liquid density can be also estimated. But even without any knowledge of the propagation distance, by scanning the beam in azimuth at a constant elevation angle, the "coolest" direction can be found that corresponds to the safest path with the least amount of total liquid (Figure 2). This radiometric measurement technique is presented and analyzed next, in Section 0.

2 Radiometry

The addition of radiometric measurement capability to future AWRs should cost very little and can have a potentially significant impact on detecting and avoiding inflight icing hazard, especially in super-cooled liquid clouds and drizzle that are often below the detection threshold of AWRs. The radiometric brightness temperature measurements can be used directly to identify the "coolest" direction with the least amount of liquid water path. Or if some assumptions can be made on drop size distribution, like in stratified precipitation, the radiometer measurements can be combined with the radar reflectivity profiles to quantify some cloud and precipitation parameters and thus the potential hazard.

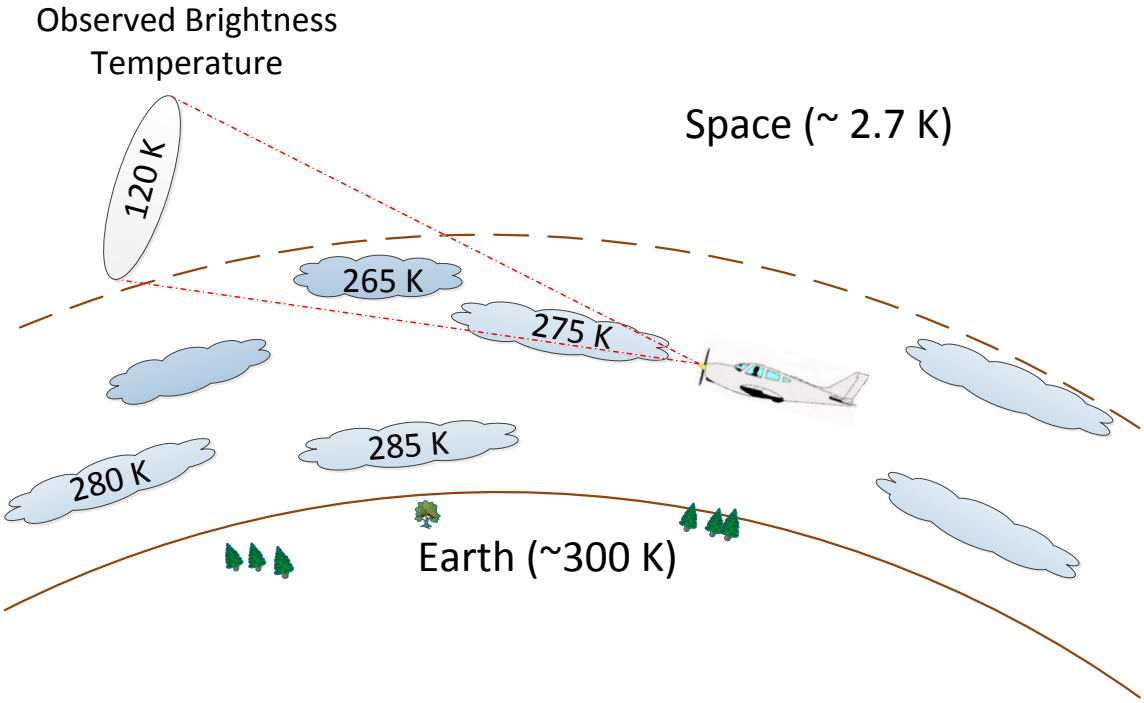

Figure 1. Side view of an aircraft radiometer measuring a cloudy scene. As long as the antenna is pointed slightly above the horizon, the background is the cold space, making the observed brightness temperature highly sensitive to attenuation and therefore to the total liquid along the antenna beam.

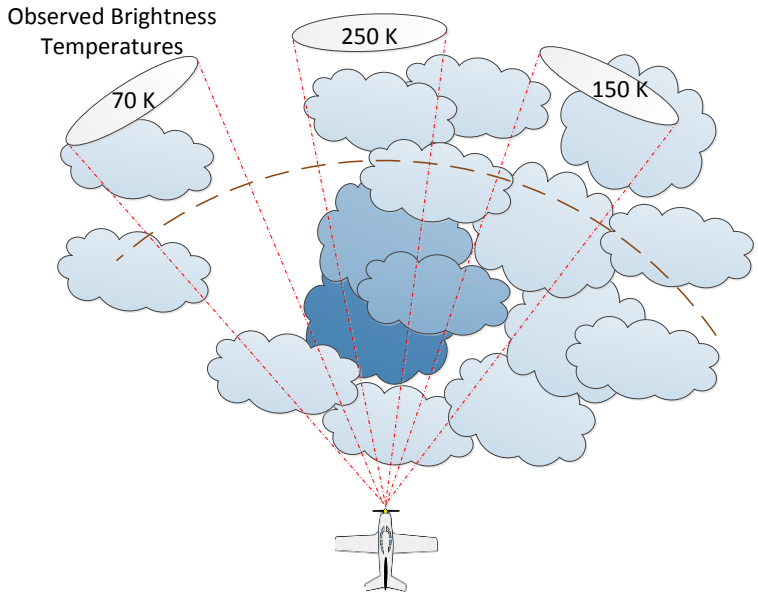

Figure 2. Top view of an aircraft radiometer measuring the brightness temperature of a cloud-filled scene. The radiometer can scan in azimuth, slightly above the horizon, to look for the "coolest" direction with the least amount of total (supercooled) liquid.

Radiometric Brightness Temperature Seen From Aircraft

Figure 3 shows an aircraft flying at altitude, A, above the earth. Located in the nose of the aircraft is a radiometer that senses the brightness temperature, T_B in degree Kelvin (K), of Planck emission from the atmosphere and from objects in front of the aircraft. In the direction defined by vector, $\bar{P}$, the radiometric brightness temperature, T_B, of the atmosphere can be computed as [3],

(2)
$$\boldsymbol{T_B = \int_0^{P_M} \kappa_T(P) \cdot T_{AT}(P) \cdot e^{-\tau(0,P)}\, dP \;\; + \;\; T_{BG} \cdot e^{-\tau_T}}$$

where,

$\theta_P =$ (see Figure 3),

$\theta_E = \theta_P - 90° =$ elevation angle associated with $\bar{P}$,

$P =$ distance from the aircraft along the vector, $\bar{P}$,

$P_M =$ maximum distance along $\bar{P}$ thru the atmosphere (see text below), $\kappa_T(P) = \kappa_L(P) + \kappa_V(P) + \kappa_O(P)$, total extinction (Np/km) at point P,

$\kappa_L(P) =$ extinction (Np/km) due to liquid water droplets (e.g., clouds and rain),

$\kappa_V(P) =$ extinction (Np/km) due to water vapor,

$\kappa_O(P) =$ extinction (Np/km) due to oxygen,

$T_{AT}(P) =$ air physical temperature (K),

$T_{BG} =$ background temperature (K) (see text below),

and,

(3) $$\tau(a,b) = \int_a^b \kappa_T(y)\, dy$$

(4) $$\tau_T = \tau(0, P_M) = \int_0^{P_M} \kappa_T(P)\, dP$$

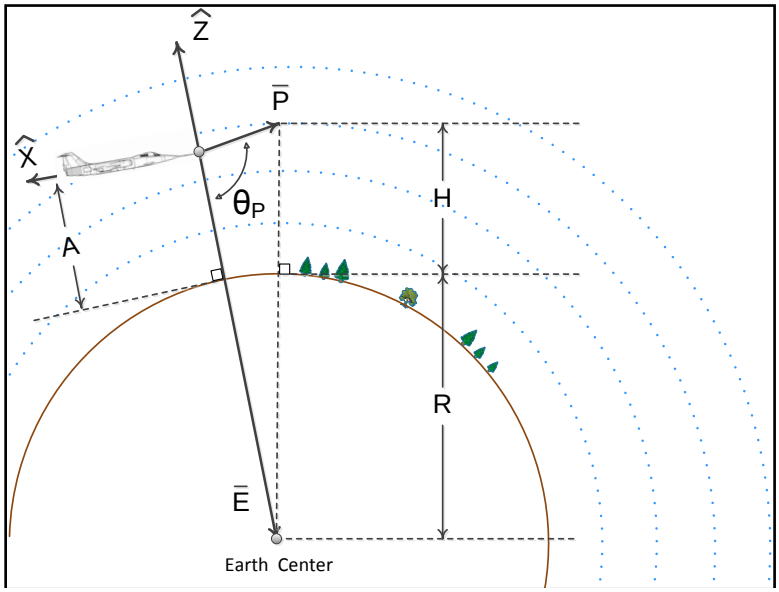

Figure 3. Geometry of aircraft flying at altitude, A, above the Earth.

Note that τ_T (Np) is the total atmospheric attenuation along the path defined by $\bar{P}$. Sometimes, (2) is approximated as [3],

(5) $$T_B \approx T_{eff} \cdot [1 - e^{-\tau_T}] + T_{BG} \cdot e^{-\tau_T} \quad ,$$

where T_{eff} in degree K, is an effective physical temperature for the atmosphere.

The integration in (2) along the path defined by $\bar{P}$ generally intersects many layers of the spherically-stratified Earth atmosphere. When $\bar{P}$ is tilted up from horizontal, this integration ends at the top of the atmosphere, and P_M is the distance from the aircraft (along $\bar{P}$) to the top of the atmosphere. However, when $\bar{P}$ is tilted down from horizontal, the integration path can end either at the top of the atmosphere or on the Earth surface. When the integration path ends at the top of the atmosphere then T_{BG} is equal to the cosmic background temperature (~2.7 *K*). When the integration path ends on the Earth surface then T_{BG} is equal to the Earth brightness temperature, and P_M is the distance from the aircraft (along $\bar{P}$) to the Earth surface. Earth brightness temperature varies over roughly 100-300 *K*, depending on surface composition, observation angle, and radiometer measurement frequency/polarization.

Clearly, the proposed radiometer measurements should be conducted with the cold 2.7 K cosmos as the background to be sensitive to atmospheric path attenuation. So the antenna has to be pointed above the horizon. But, by how much? The next section (0) formulates a model for the gain pattern of a typical antenna and presents an example of measured earth surface bias as a function of elevation angle with a 1' diameter AWR antenna in section 0.

The Radiometer Measurement

The radiometer measurement is called antenna brightness temperature, $T_A\ (K)$. It is defined [3] as a spatially weighted average of T_B with weights derived from the antenna power-receive pattern, G_A. Here, the following calculation for T_A will be used.

(6) $$\boldsymbol{T_A = \int_0^{2\pi}\int_0^{\pi} G_A\left(\theta - \frac{\pi}{2},\ \varphi - \pi\right)\cdot T_B\ d\Omega}$$

where, $d\Omega = \sin(\theta)\, d\theta\, d\varphi$, $\int_0^{2\pi}\int_0^{\pi} G_A\, d\Omega \equiv 1$, and (θ, φ) are spherical coordinate system angles associated with the axes shown in Figure 3. Here, it is also assumed that,

(7) $$\boldsymbol{G_A \propto \left[\frac{\sin(\alpha_1)}{\alpha_1}\cdot\frac{\sin(\alpha_2)}{\alpha_2}\right]^2,\ \alpha_1 = \frac{\theta-\frac{\pi}{2}}{0.36\,\theta_B},\ \alpha_2 = \frac{\varphi-\pi}{0.36\,\theta_B}},$$

where $\theta_B\ (rad)$ is the antenna half-power beamwidth.

Antenna beamwidth causes the radiometer field-of-view (FOV) to be a conical region. For the airborne radiometers shown in Figure 4, this conical FOV is depicted by the red-colored lines. Note that FOV for the radiometer on aircraft #1 makes visible the T_B of trees and soil on the Earth's surface. For the radiometer on aircraft #2, the FOV does not contain the Earth but does make visible the sun, aircraft #3, and radar transmissions from aircraft #3. Here, the T_B associated with Earth, sun, and other aircraft are considered interference, since only atmospheric T_B is of interest. As suggested by Figure 4, there are strategies for avoiding this interference. For example, flying higher or pointing the radiometer antenna above horizontal can reduce interference from the Earth and from man-made transmissions (radars) located on the Earth. Solar interference can be avoided by pointing the radiometer antenna away from the sun. Software is available for determining sun location and can be used when the sun is obscured by clouds. Hence, with knowledge of aircraft altitude, heading, and pitch/roll, much of the radiometer interference can be greatly reduced via repointing of the radiometer antenna or mitigated by flagging the data. Finally, radiometers themselves can determine when the T_A measurement is corrupted by man-made signals. These interference detection techniques are described in [4] and [5].

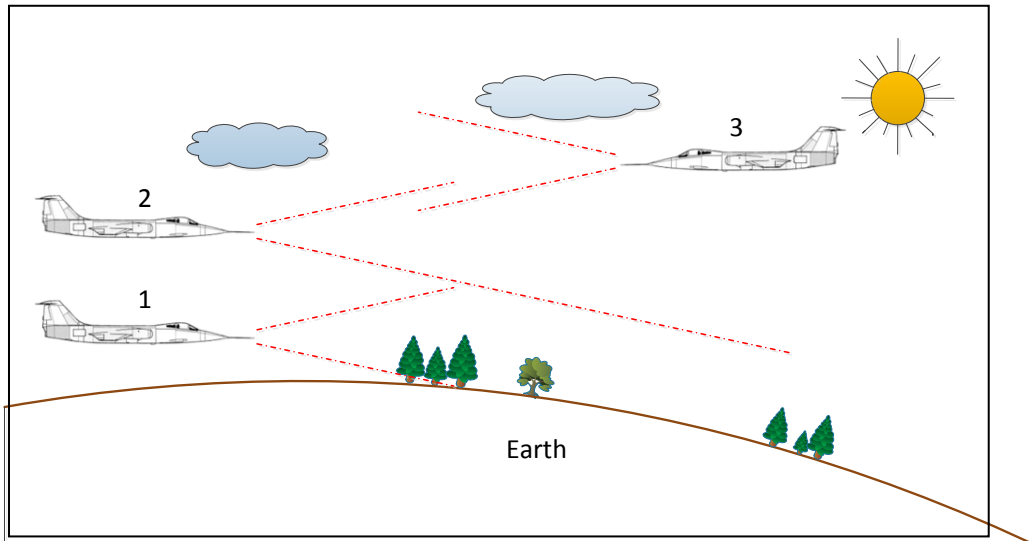

Figure 4. Field-of-view (red boundaries) for radiometers aboard three aircraft.

Radiometer for Severe Weather Avoidance

With the background of the previous sections in-hand, the radiometer's role in severe weather avoidance can now be explained. First, note that radars can sometimes fail to detect severe weather because of intervening water-laden atmosphere that is both heavily attenuating (i.e., large κ_T) and weakly reflective. This radar problem is shown pictorially in Figure 5 where the heavily attenuating atmosphere and severe weather (shown in red) has obscured radar returns from areas further in range (indicated by pink arrows). However, as described below, the radiometer views the same scene much differently than the radar and would probably not be "blind" to the areas indicated by pink arrows.

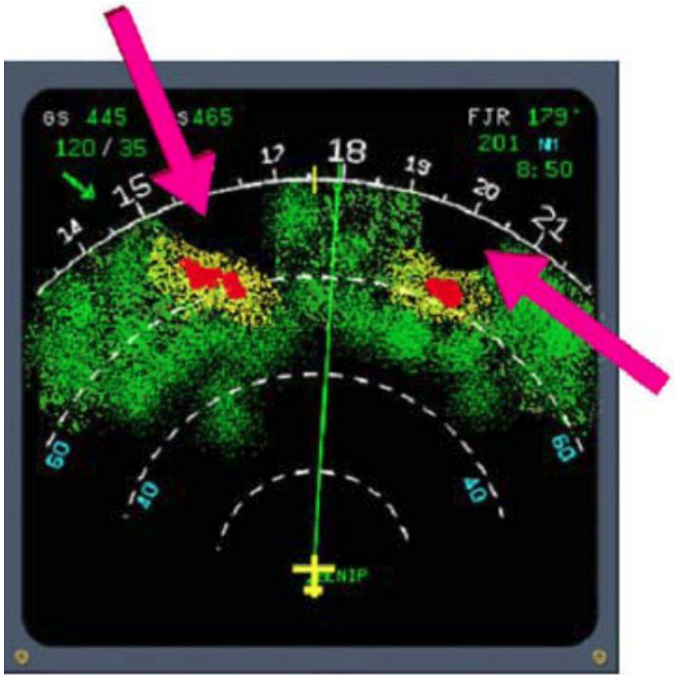

Figure 5. Radar return showing two severe weather cells (red) that obscure returns from areas further in range (pink arrows).

Note from (2) that when the atmosphere has no attenuation (i.e., $\kappa_T \sim 0$ in (2) or $\tau_T \sim 0$ in (5)) then $T_B \sim T_{BG}$. That is, without interference, the radiometer sees the cold background ($T_{BG} \sim 2.7\ K$) of outer space. However, when the atmosphere has high attenuation (i.e., $\kappa_T \sim \infty$ in (2) or $\tau_T \sim \infty$ in (4)), then $T_B \sim T_{eff} \sim 250\ K$. As long as T_B lies between T_{BG} and T_{eff}, then the radiometer measurement is said to be "not saturated" and a value of τ_T can, in principle, be derived from T_B using (5). As shown in the sections to follow, an X-band radiometer measurement is seldom saturated in the proposed configuration.

Radiometers cannot replace radars as a tool for severe weather detection, since radiometers cannot directly provide weather-distance (i.e., range) information. The following discussion elaborates on this point. Note from (4) that the value of the total attenuation (τ_T) derived from the radiometer measurement is the total or integrated value along the entire atmospheric path defined by $\bar{P}$ in Figure 3. Information in addition to the radiometer measurement is needed to determine whether the total attenuation (τ_T) results from a very deep weather cell having low attenuation rate (small κ_T) or a thin weather cell having high κ_T. Severe weather (e.g., heavy rain) is more strongly correlated with high κ_T than high τ_T. Hence, for severe weather detection, it is more useful to know how κ_T varies along $\bar{P}$ rather than simply knowing τ_T. The range information provided by radar measurements can be used to transform radiometer measurements of τ_T into values of κ_T. A novel method of deriving rough estimates of κ_T using only the radiometer data is discussed in section 0.

However, should the radar fail, a novel all-radiometer severe weather avoidance strategy is possible. This strategy is implied by Figure 2 and consists of scanning the area forward of the aircraft to find the region of minimum observed brightness temperature. The aircraft then flies towards this region since minimum brightness temperature implies minimum path attenuation as well as minimum liquid path (integrated rain rate) and thus (hopefully) the safest direction.

Atmospheric Attenuation Details

It appears most cost effective to upgrade existing X-band AWRs with either or both a radiometer mode and a dual-linear polarization (V and H) antenna. Hence, the focus here is on atmospheric attenuation at 9.3GHz for both V and H polarization. Before starting, we make clear the distinction between total atmospheric attenuation, in units of Nepers (Np) or decibel (dB), and atmospheric extinction (Np/km or dB/km). As shown in (3), the integral over distance of extinction produces attenuation. The units of extinction can be either Np/km or dB/km, where the conversion is $4.34\ \mathrm{dB/km} = 1.0\ \mathrm{Np/km}$

Plotted in Figure 6. is the calculated value of extinction caused by water vapor and oxygen in the US Standard Atmosphere (i.e., $\kappa_V + \kappa_O$ in (2)) [3]. This calculation depends on altitude above the Earth because the density of both water vapor and oxygen thins with altitude and, to a lesser extent, because physical temperature at altitude has an effect.

At the frequencies of interest in this report, dry-atmosphere extinction (i.e., $\kappa_V + \kappa_O$) is typically much smaller than the extinction caused by rain and clouds. Rain and clouds can both be characterized as collections of liquid water droplets. The basis for extinction, κ_L, caused by liquid water comes from Mie theory [3][6], which is considered exact when the droplets have spherical shape. The spherical shape approximation is accurate for small droplets and the smallest of these remain suspended in the air as clouds. However, as shown in Figure 7, the larger droplets will fall through the air at significant velocity as rain. The air resistance at these fall velocities can change the droplet shape from spherical to oblate-spheroid. When the drop diameter nears 0.005 m, the fall velocity can cause sufficient air resistance/turbulence to break the droplet apart [7]. The oblate-spheroid shape of the droplets causes the extinction of rain to be polarization dependent. Convenient formulas that take this polarization dependence into account are given by [8]. These formulas were used to calculate the rain extinction at both V-pol and H-pol experienced by a 9.3 GHz wave traveling in the horizontal direction thru rain. Results of these calculations are plotted in Figure 6..

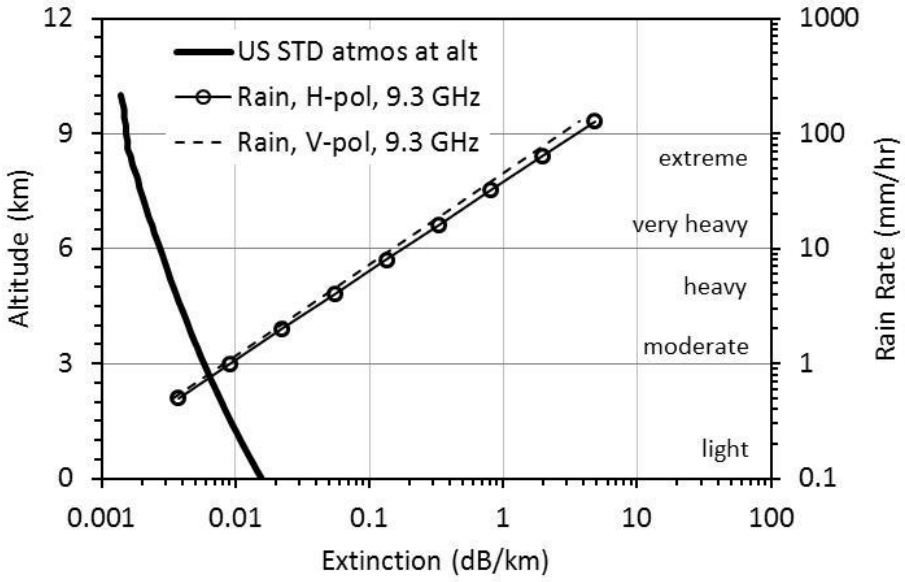

Figure 6. Extinction at 9.3 GHz for rain and for the rain-free US Standard Atmosphere

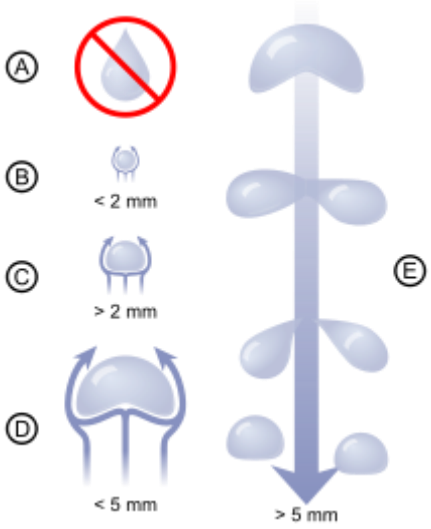

Figure 7. Raindrop shape depends on size and fall velocity. Drops larger than 5mm in diameter often break into smaller drops [7].

Simulated Radiometer Measurements in Severe Weather

Software was developed to compute values of T_A that are seen by an airborne radiometer. The software uses formulas from sections 0 and 0 and can account for the following factors:

- radiometer operating frequency
- antenna beamwidth and gain pattern
- antenna pointing (elevation angle)
- aircraft flight altitude
- round Earth effects

- Earth surface brightness temperature
- atmospheric physical temperature, pressure, water vapor (all functions of altitude)
- rain rate
- rain height
- rain storm radius
- aircraft location within the rain storm

Here, calculations from the software are used to determine what conditions (if any) cause the radiometer measurement to saturate at T_{eff} as discussed in section 0. The following notes apply to these calculations.

1. The radiometer operating frequency is 9.3 GHz, which is the operating frequency of many airborne weather radar (AWR).
2. Antenna beamwidth of $\theta_B = 7.5° = 0.13$ rad is used and is typical for a medium sized AWR antenna.
3. The rain height is $3 - 4$ km, which is typical for many mid-latitude storms. Rain height is also referred to as the height of the melting/freezing layer. Above this height, the water is in its frozen state. Frozen water causes much less attenuation than the liquid water located below the rain height [3].

Results of our first calculations are plotted in Figure 8 and are for a small severe weather cell, similar in size to a small thunderstorm. In particular, this weather cell has a rain height of $3\ km$ and the rain-filled region of the cell extends to a range of 12 km in front of the radiometer/aircraft. The Figure 8 (a) data results when the radiometer antenna is pointed straight ahead (i.e., $\theta_E = 0°$). The three curves in this plot correspond to three separate flight altitudes, with the lower (1 km) and upper (5 km) altitudes being below and above the rain height respectively. The Figure 8 (b) data results when the antenna is pointing up by about one-half of the antenna beamwidth (i.e., $\theta_E = 4°$). For these calculations, $T_{eff} \sim 280$ K and represents the T_A saturation value. Note that T_A saturation is observed when the radiometer is flying below the rain height and only when rain rates are extreme (> 60 mm/hr). Also note the differences between Figure 8 (a) and Figure 8 (b) at low rain rates, which are due to differences in θ_E. That is, for the slight up-tilt of the antenna in Figure 8 (b), T_A becomes less biased (corrupted) by the Earth brightness temperature (here assumed to be 288 K).

Results of our second calculations are plotted in Figure 9 and are for a large thunderstorm. For this storm, rain height is 4 km and the rain-filled region of the cell extends to a range of 35 km in front of the radiometer/aircraft. As in Figure 8, $T_{eff} \sim 280$ K and Earth brightness temperature is 288 K. Unlike Figure 8, the flight altitudes of 1 km and 3 km are now both below the rain height. Also note that, due to the larger extent of the storm, T_A saturation occurs when rain rates are very-heavy (> 30 mm/hr) instead of extreme.

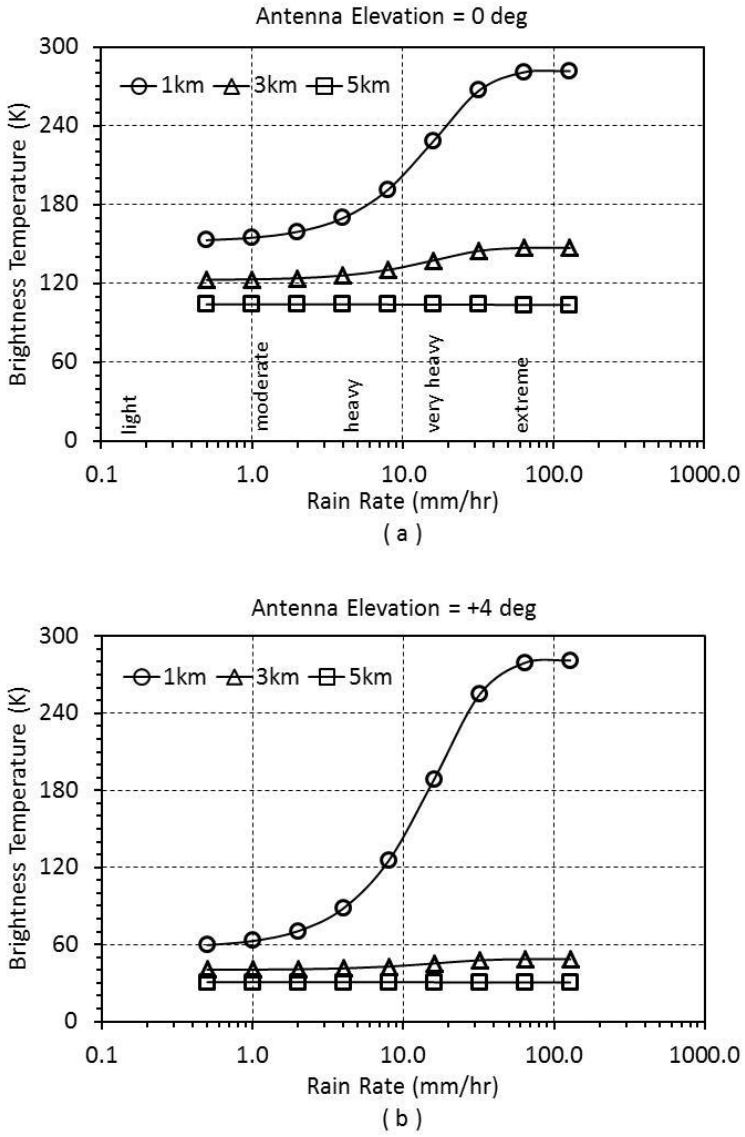

Figure 8. Computed brightness temperature of a SMALL thunderstorm for antenna elevation angles of (a) 0deg and (b) 4deg and for flight altitudes of 1km, 3km, and 5km. The rain height is 3 km.

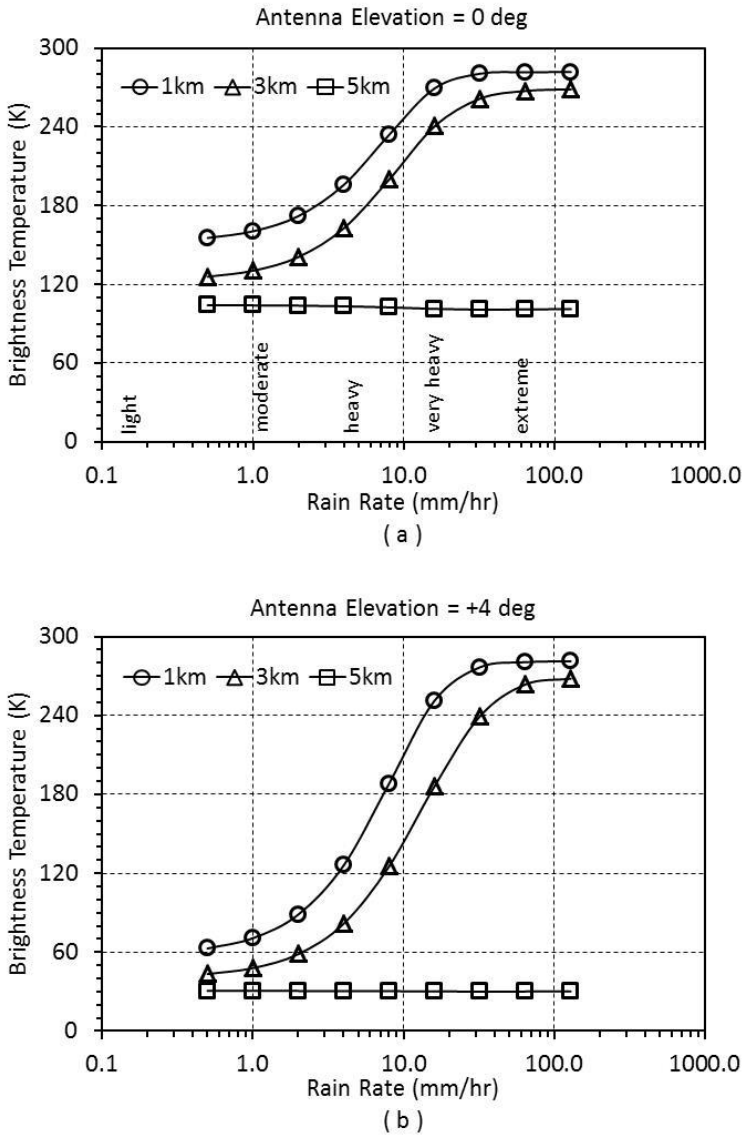

Figure 9. Computed brightness temperature of a LARGE thunderstorm for antenna elevation angles of (a) 0deg and (b) 4deg and for flight altitudes of 1km, 3km, and 5km. The rain height is 4 km.

Retrieving Total Atmospheric Attenuation from Radiometer Data

In (5), the substitution, $L_T = e^{-\tau_T}$, is used to give (9) where L_T is interpreted as total loss of the atmosphere.

(8) $$\boldsymbol{T_B \approx \ T_{eff} \cdot [1 - \ L_T \,] \ + \ T_{BG} \cdot L_T}$$

Straightforward manipulation of (8) gives the following solution for L_T.

(9) $$\boldsymbol{L_T = \frac{T_B - T_{eff}}{T_{BG} - T_{eff}}}$$

The precision, ΔL, associated with a retrieval of L_T from T_B using (9) depends on the measurement precision (NEDT), ΔT, for T_B. See Section 0, for further discussion on ΔT. The relationship between ΔL and ΔT can be derived from (8) as,

(10)
$$\Delta L = \frac{\Delta T}{\left|\frac{\partial T_B}{\partial L_T}\right|} \approx \frac{\Delta T}{T_{eff} - T_{BG}}.$$

Using $T_{eff} = 280K$, $T_{BG} = 2.7K$, and two values of ΔT (NEDT), ΔL can was calculated from (10) and plotted in Figure 10.

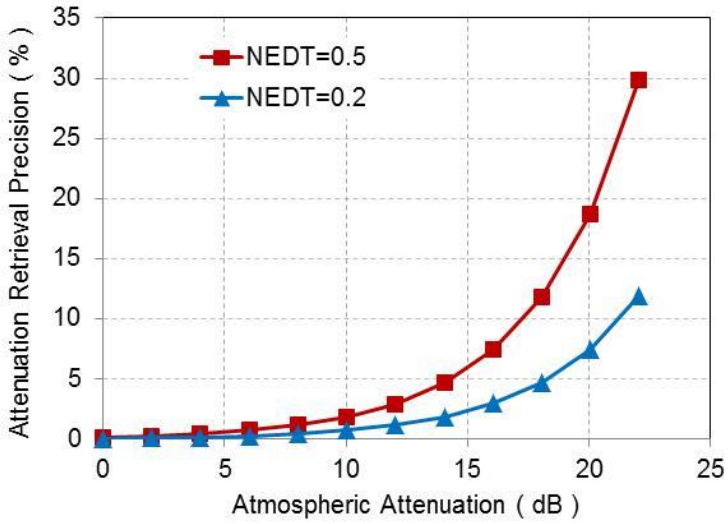

Figure 10. Atmospheric attenuation retrieval precision caused by radiometer NEDT.

However, ΔL can also be affected by errors in T_{eff}. For example, using a value of T_{eff} that is either too high or too low by 1% (~3 K) will bias the retrieved value of L_T as shown in Figure 11. When reviewing Figure 11, note that a 100% error in L_T is also a 3 dB error in L_T. Thus, for example, when actual $L_T \approx 20$ dB, a 100% bias in L_T implies either 23 dB or 17 dB. In principle, when the radiometer antenna is pointing at small elevation angles, the physical temperature of air near the radiometer/aircraft should serve as an accurate estimate for T_{eff}.

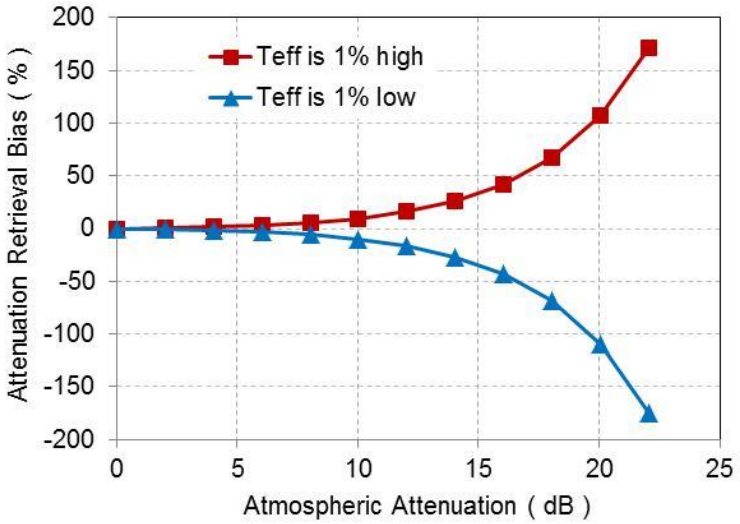

Figure 11. Atmospheric attenuation retrieval bias caused by error in T_{eff}.

Retrieving Rain-Rate and Rain-Depth from Radiometer Data

As discussed in section 0, radiometer measurements are typically used to estimate total path attenuation, $\tau_T = -\ln(L_T)$. However, estimates of attenuation rate, κ_T are more useful for severe weather detection. Knowing κ_T is equivalent to knowing both rain rate, R (mm/hr), and rain depth, d_R (km). Here, a novel method is presented for estimating R and d_R from only measurements of the radiometer.

Using the relationship in (5), the V-pol and H-pol measurements of a radiometer that is viewing rain of depth, d_R, can be approximately calculated as,

(11) $$\boldsymbol{T_B(p) \approx T_{eff} \cdot \left[1 - e^{-\kappa_L(p) \cdot d_R}\right]} \ .$$

Where p is the polarization, commonly V (vertical) or H (horizontal).

From [8], one finds that at 9.3GHz,

(12) $$\boldsymbol{\kappa_L(p) = \kappa_p \cdot R^{\alpha_p} \ , \ p = (V, H)} \ ,$$

where, V − pol: $(\kappa_V, \alpha_V) = (0.00792, 1.265)$

and H − pol: $(\kappa_H, \alpha_H) = (0.00881, 1.296)$.

Hence, T_B(V) and T_B(H) represent two equations of the form shown by (11) that contain two unknowns, R and d_R. The closed-form solution for R is given by,

(13) $$\boldsymbol{R = \left[\frac{\kappa_H}{\kappa_V} \cdot \frac{ln\left(\frac{T_{eff}}{T_{eff} - T_B(V)}\right)}{ln\left(\frac{T_{eff}}{T_{eff} - T_B(H)}\right)}\right]^{\frac{1}{\alpha_V - \alpha_H}}} \ .$$

Once a value of R is computed from (13), it can be substituted into (11) to solve for d_R. Note that the condition, $\alpha_V \neq \alpha_H$, makes the solution for both R and d_R possible. When $\alpha_V = \alpha_H = \alpha_0$, then there is effectively only the one unknown, $d_R \cdot R^{\alpha_0}$, and separate solutions for d_R and R are not possible.

Further analysis shows that the solutions for d_R and R from 9.3 GHz radiometer data described above are quite sensitive to ΔT. Retrieval error in d_R and R for $\Delta T = 1$ K in both T_B(V) and T_B(H) was computed and is shown in Figure 12. As seen in these plots, retrieval error depends on the actual values for d_R and R.

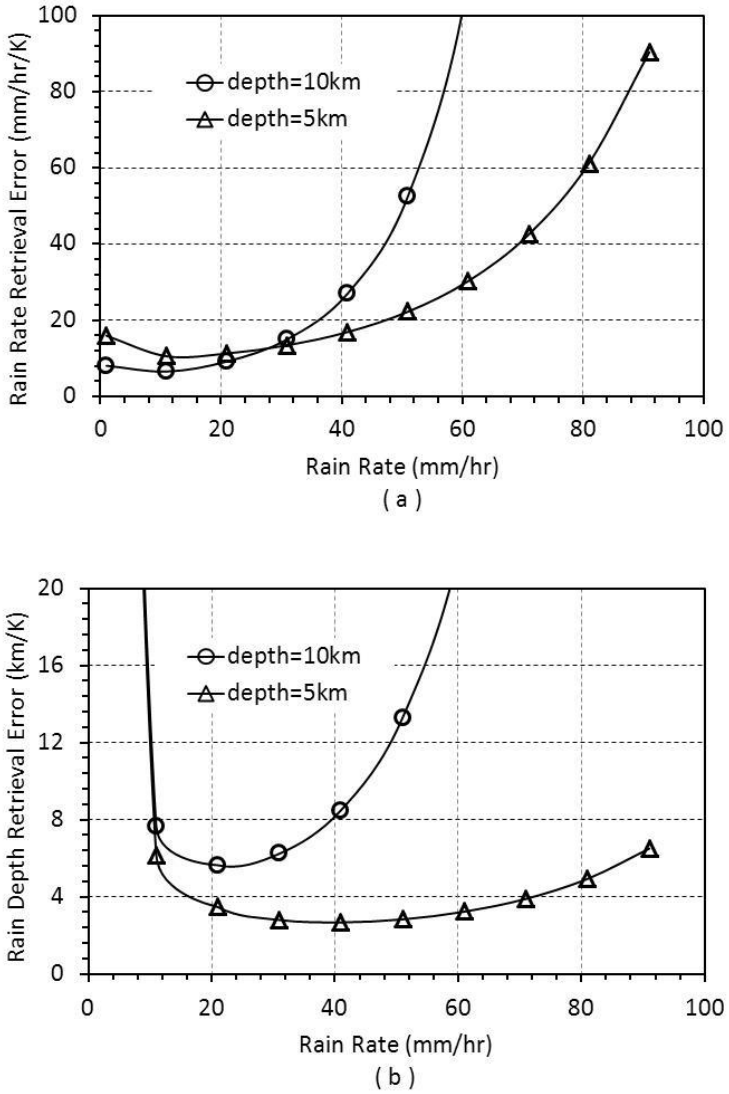

Figure 12. Retrieval error for (a) rain rate and (b) rain-depth when raw radiometer measurement error is 1.0 K.

Brassboard Radiometer Description

For experimental purposes, a simple radiometer (i.e., brassboard) was constructed. The radiometer is described by the block diagram in Figure 13 and by the photo in Figure 14. The radiometer antenna was made by Cobham (part# 460386) and is commonly used by aircraft weather radar. Receiver components were housed in a Styrofoam enclosure to help stabilize receiver physical temperature and reduce radiometer calibration drift. Data acquisition from the radiometer utilized an Agilent Technologies spectrum analyzer, part# E4440A. The radiometer was calibrated using commercially-available calibrated noise sources and microwave absorbing material. Calibration data is shown in Figure 15.

Error! Reference source not found.**Brassboard radiometer receiver.**

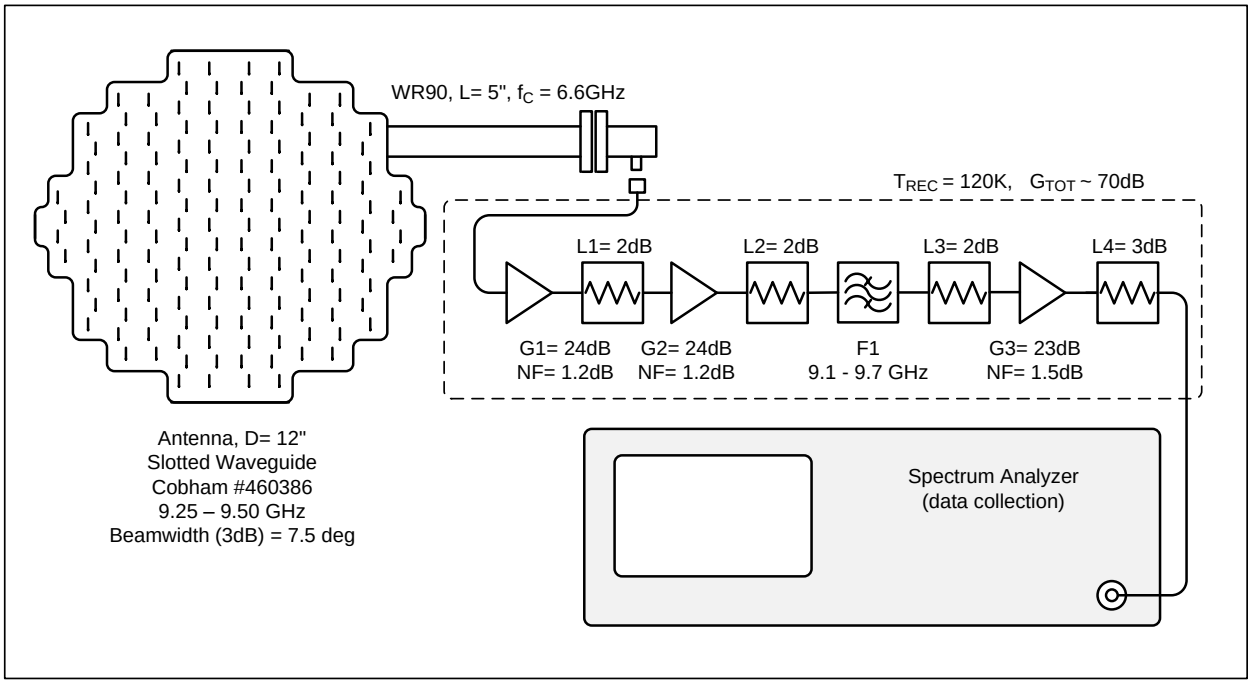

Figure 13. Block diagram of the brassboard radiometer.

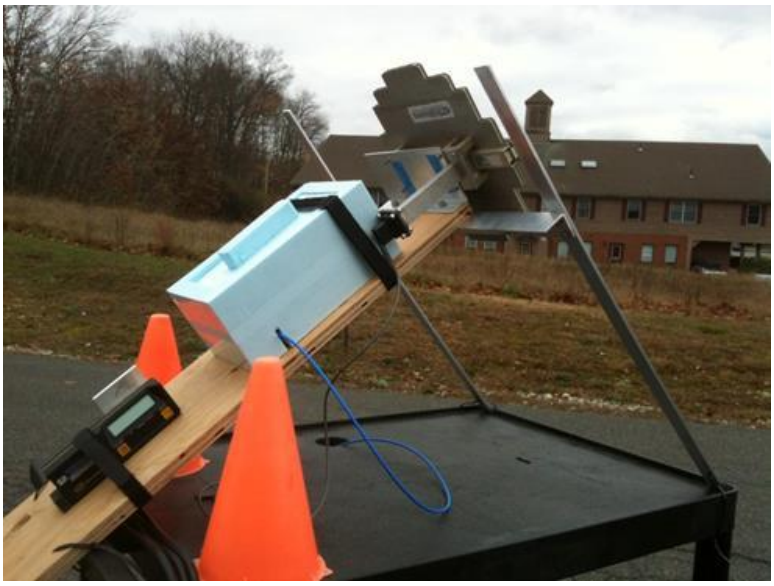

Figure 14. Brassboard radiometer.

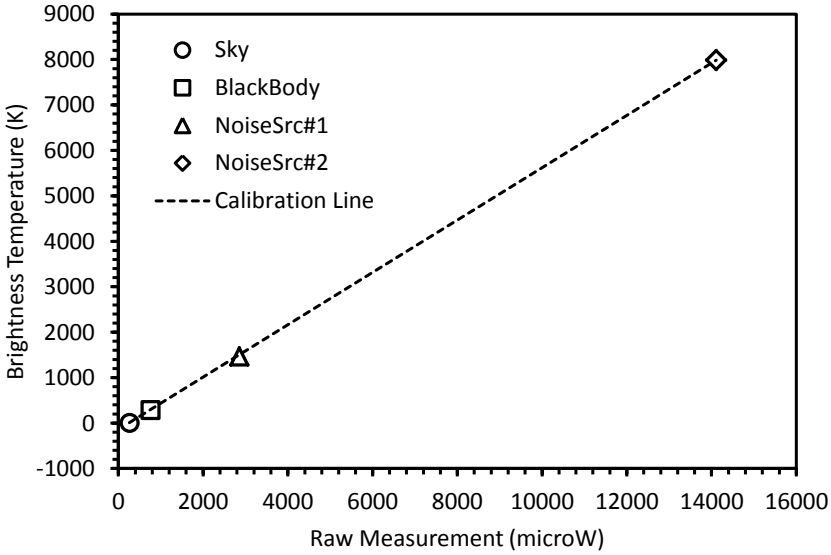

Figure 15. Calibration curve for the brassboard radiometer.

Brassboard Radiometer Experiment

The brassboard radiometer described in the previous section was used to validate our theoretical description of the radiometer measurement (T_A) given in sections 0 and 0. More specifically, data was collected from the ground-based brassboard radiometer as it was tilted to scan from Earth to the sky across the horizon. The effective horizon during this experiment was the top of the wide building shown in Figure 14. Measured and calculated values of T_A for this experiment are shown in Figure 16. First, note that the horizon for this experiment was measured to be at an elevation angle of 5°. Thus, when the radiometer antenna was scanned to $\theta_E = 5°$ then half of its antenna beam observes the Earth and half observes clear sky. Hence, the measured T_A at $\theta_E = 5°$ is seen to be about half-way between the clear sky value of ~ 3 K and the Earth value of

~250 K. Calculations plotted as a solid line in Figure 16 used the actual radiometer antenna beamwidth of $\theta_B = 7.5° = 0.13$ rad. These calculated values of T_A agree well with the measured data, giving us confidence with our modeling. The dashed-line calculations shown in Figure 16 used $\theta_B = 0°$ and can be interpreted as the T_B-profile of the scene. As discussed in Section 0, the brassboard radiometer T_A measurements represent an antenna-beam weighted average of this T_B-profile. These results indicate that an AWR antenna only needs to be pointed up in elevation by less than the beamwidth to prevent loss of sensitivity from earth surface radiation.

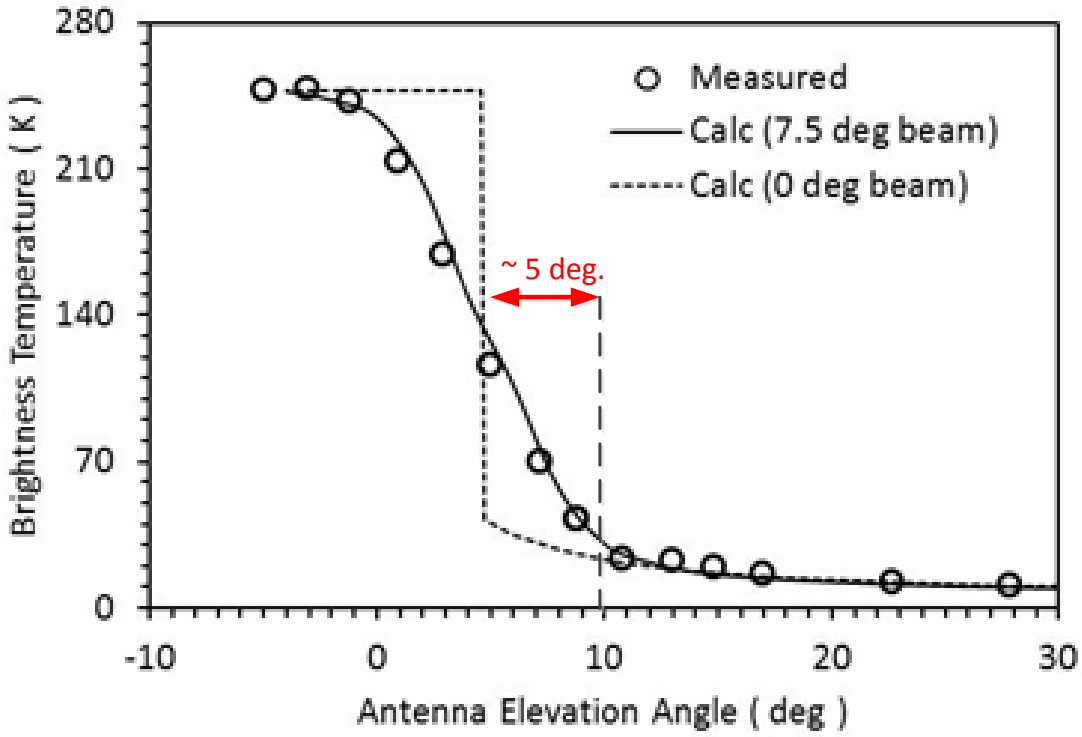

Figure 16. Measured brightness temperature as a function of elevation angle. This shows that a 7.5 deg beamwidth (1' diameter) antenna has to be pointed in elevation a minimum of about 5 deg above the horizon to prevent significant earth surface radiation interference. A larger antenna with narrower beamwidth could be pointed even closer to the horizon.

Combined Radar/Radiometer Retrieval

In some cases co-located radar and radiometer measurements can be made. Here "co-located" emphasizes that a similar range interval is sampled and detected by the radar and that the same range interval contributes most of the path attenuation and thus the radiometer measured brightness temperature. The next analysis shows how such co-located radar and radiometer measurements might be combined to better characterize liquid precipitation.

The general radiometric transfer equation for the radiometer observed brightness temperature is given by [24], Vol. 3, Ch. 17, pp. 1331, Eq. 17.80 as

$$T_B = \int_0^\infty \kappa_T(P) T_{AT}(P) e^{-\int_0^\infty \kappa_T(P')dP'} dP + T_{BG} e^{-\int_0^\infty \kappa_T(P)dP} \quad \textbf{(14)}$$

where

T_{BG} is the background radiation ,

θ is the Zenith angle (θ = 90 –> pointing towards the horizon),

κ_T is the total atmospheric absorption coefficient in units of nepers per unit distance at distance *P* from the radar, and

T_{AT} is the temperature of the atmosphere at *P*.

In a stratified cloud/precipitation, where uniform physical temperature and drop size distribution can be assumed, the observed brightness temperature can be approximated with the following much simpler expression [24] Vol. 3, Ch. 17, pp. 1331, Eq. 17.83 :

$$T_B = T_{BG} e^{-\kappa_\circ \Delta P} + \widehat{T}_{AT}\left[1 - e^{-\kappa_\circ \Delta P}\right], \quad \textbf{(15)}$$

where

$\widehat{T}_{AT}$ is the effective (or mean) radiating atmospheric temperature, and

ΔP is the extent of the cloud/precipitation layer along the antenna beam direction .

The exponential attenuation factor, $e^{-\kappa_\circ \Delta P}$ through the cloud-precipitation along the antenna beam can be defined as the *total loss factor*, $L_T \equiv e^{-\kappa_\circ \Delta P}$, and since the comic background radiation is a negligible 2.7 K, the observed brightness temperature can be simply approximated as

$$T_B \approx (1 - L_T) T_{AT} . \quad \textbf{(16)}$$

So if the mean cloud/precipitation physical temperature can be estimated from in situ measurements and extrapolated into the cloud/precipitation layer, then from the observed brightness temperature, the *total loss factor* can be calculated. L_T can be also expressed as a function of the more commonly used *attenuation coefficient*, α in units of dB/km, where κ_a (nepers/km) = 0.23α (db/km)

$$L_T = e^{-0.23\alpha\Delta P} . \quad \textbf{(17)}$$

From the radar measurements, the cloud/precipitation path length (ΔP) can be directly measured and then the path attenuation rate α can be calculated.

The attenuation rate is directly proportional to the liquid water content for hydrometeors that are much smaller than the radar wavelength, Rayleigh scatterers (when $\left| n 2\pi r / \lambda \right| < 0.5$, where *n* is the index of refraction, *r* is the cloud/precipitation drop radius and λ is the radar wavelength) [3]:

$$\alpha = m_v f^{1.95} \exp\left[-6.866\left(1 + 4.5\times10^{-3} T\right)\right], \quad \textbf{(18)}$$

where

m_V = liquid water content (g/m^3),

f is the radar frequency and T is the cloud/precipitation temperature.

So from the radiometer observed brightness temperature and radar measured cloud/precipitation path length, the attenuation rate and then mean liquid water content can be estimated.

$$m_v = \frac{4\pi}{3}\sum_{i=1}^{N}\left(\frac{D_i}{2}\right)^3 = \frac{\pi}{6}N_V D_V^3 \quad , \tag{19}$$

where

D_i is the i[th] cloud/precipitation scatterer diameter, D_V is an equivalent volume diameter and N_V, the equivalent volume number density.

The radar received power for Rayleigh scatterers is proportional to the sixth moment of the drop size distribution (see section 4.1.2, equation (68):

$$P_r = \frac{P_t A n_A^2 c\tau}{32 r^2}\sum_{i=1}^{N}\frac{\pi^5 |K|^2 D_i^6}{\lambda^4} \tag{20}$$

And similarly, defining an equivalent volume diameter, D_V, and number density, N_V, the radar measured power can be written simply as

$$P_r = \frac{P_t A n_A^2 c\tau \pi^5 |K|^2}{32 r^2 \lambda^4} N_V D_V^6 \tag{21}$$

By combining the radiometer measured liquid water content with the radar received backscattered power, the equivalent volume diameter and number density can be estimated:

$$\frac{P_r}{m_V} = \frac{3P_t A n_A^2 c\tau \pi^4 |K|^2}{16 r^2 \lambda^4} D_V^3 \quad , \tag{22}$$

so

$$D_V = \sqrt[3]{\frac{P_r 16 r^2 \lambda^4}{m_V 3 P_t A n_A^2 c\tau \pi^4 |K|^2}} \tag{23}$$

and

$$N_V = \frac{6 m_V}{\pi D_V^3} m_v \quad . \tag{24}$$

A measure of drop size and liquid water content are important parameters for characterizing the hazard potential of super-cooled precipitation. Higher liquid water content clearly presents an increased hazard potential, because there is more liquid available to freeze on the aircraft wing. But drop size is also important, because larger drops shatter on impact and can cause enhanced surface roughness and have larger areas of impingement, sometimes beyond the ice protection system.

Adding Radiometer Mode to a Weather Radar System

New-model, digital-output, AWR (e.g. Rockwell RTA-4100) can cost $150,000. Old-model, digital-output AWR (e.g., Honeywell PRIMUS-440) cost $80,000 for a new system and used systems cost about $30,000. Digital-output AWR have mostly replaced the older analog-output AWR. However, some analog-output AWR are still utilized and have a used price of roughly $5,000-$15,000. Major manufacturers of aircraft weather radar (AWR) are currently:

- Rockwell-Collins
- Honeywell
- Bendix-King
- TelePhonics
- Garmin

To permit planning for the addition of a radiometer mode to an AWR, technical information was requested from some of these AWR manufacturers. However, the contacted manufacturers required a non-disclosure agreement from us before providing any technical information. This disclosure agreement seemed inappropriate at this early planning stage. So, detailed AWR technical information was not obtained. However, as shown below, many aspects of joint AWR/radiometer operation can still be investigated.

The method of using a radiometer to assist the AWR with severe weather avoidance was described in sections 0 and 0. For this application, moderate measurement accuracy ($\sim 5\,\mathrm{K}$) is required from the radiometer. In principle, existing radar circuitry could be used to make the radiometer measurements and achieve this accuracy after some simple hardware modifications. These hardware modifications consist of adding a switch and calibrated noise source to the AWR front-end electronics as shown in Figure 17. Note that noise source is used as a warm load calibration unpowered, and as a hot load when the power to the noise source is turned ON. The radar receiver is then reprogrammed to occasionally toggle both the new switch, S2, and the noise source power so that data can be collected from the noise source in both ON and OFF state. This noise source data is then used for radiometer calibration in the manner described by Figure 15. As shown in Figure 18, operation of the AWR is also modified so that the transmit (TX) pulse is absent or blanked immediately before radiometer data collection. Following the blanked-pulse, all the range-gate data samples collected over the pulse-repetition-interval (PRI) can be averaged and used as radiometer data.

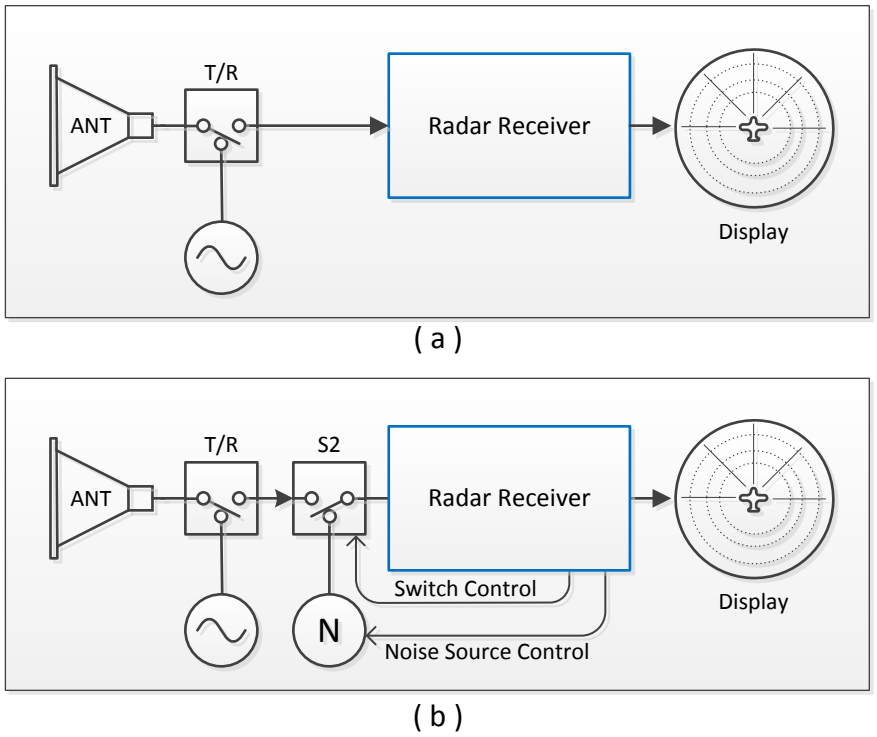

Figure 17. Aircraft weather radar (a) before and (b) after radiometer mode modification.

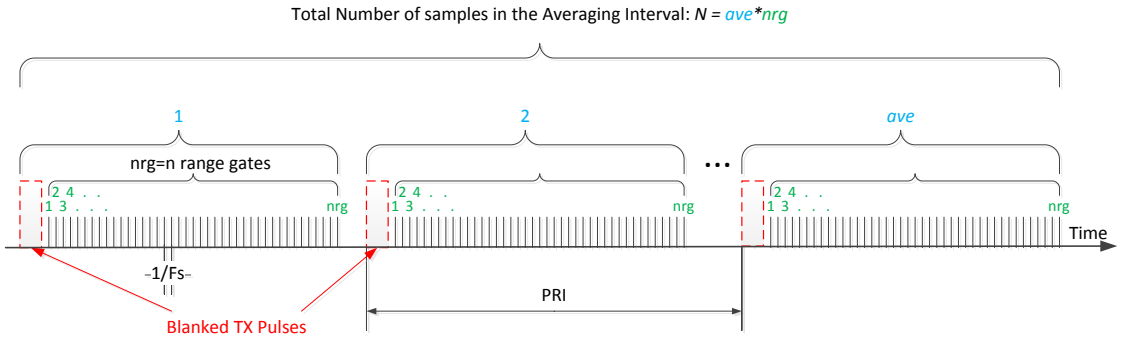

Figure 18. Blanking the transmit (TX) pulses for the radar permits radiometer data collection.

With this overview in hand, details of radiometer operation and performance can now be discussed. Precision, ΔT (K), of the radiometer measured T_A can be estimated from [3],

(25) $$\Delta T = \frac{T_A + T_{REC}}{\sqrt{B_{IF} \cdot t_A}}$$

where T_{REC} (K) is the receiver noise temperature, B_{IF} (Hz) is the bandwidth of the receiver, and t_A (s) is the time interval over which the data is averaged. As shown in Table 1, modern AWR typically have T_{REC}~290 K and B_{IF}~520,000 Hz. When T_A is near 280 K, calculation (25) shows that achieving ΔT~5 K will require t_A~0.025 s. Further, if the radar scans a 90° (azimuth) × 30°(elevation) sector forward of the aircraft with a 7.5° wide antenna beam, then about $(90/7.5) \times (30/7.5) = 48$ separate radiometer measurements are needed. Since each measurement takes 0.025 s, a total of $48 \times 0.025 = 1.2$ s will be required to perform a complete

scan. Thus, the aircraft pilot would have severe weather updates from the radiometer at a rate of about once a second.

However, surely the radar receiver bandwidth could be opened up to at least 5 MHz, and modern data acquisition system can easily process data at that sample rate. So repeating the above calculation, the approximate update rate with this more realistic receiver bandwidth would decrease to 0.4 sec, yielding two scan updates per second.

Table 1 Specifications of a modern aircraft weather radar.

Design Parameters		Derived Parameters	
Frequency (MHz)	9500	Wavelength (cm)	3.16
Pulse Width (μs)	2	Receiver Bandwidth (MHz)	0.52
Pulse Repeat Freq (kHz)	6	Maximum Range (km)	25
Rcvr Noise Figure (dB)	3	Rcvr Noise Temperature (K)	290

Radiometer Summary and Conclusions

Adding a radiometer mode to conventional aircraft weather radar (AWR) will improve hazardous weather detection/avoidance by overcoming some radar deficiencies (e.g., insufficient sensitivity in liquid cloud and drizzle conditions, severe weather blind-spots) and assisting the radar to determine atmospheric attenuation.

Radiometer measurements can be processed into estimates of total atmospheric attenuation (dB). However, as discussed in section 0, atmospheric extinction ($\mathrm{dB/km}$) is a more useful indicator of severe weather than atmospheric total attenuation. Radiometer measurements can be combined with radar measurements to derive atmospheric extinction. A novel method for roughly estimating extinction using only radiometer data was presented in Section 0. However, it is generally more accurate to use the combined measurements from radar and radiometer to estimate extinction.

A novel radiometer-only strategy for severe weather avoidance was presented in section 0. This all-radiometer strategy consists of flying towards the area of least atmospheric attenuation and should help overcome radar blind-spots. It was calculated that radiometer blind-spots (i.e., saturation) occur only under the unusual conditions of extreme rain rates that extend more than 12 km in front of the aircraft. Tilting the antenna further up in elevation reduces the chance of saturation even in severe conditions..

Radiometer measurements can be contaminated by interference from the sun, Earth, other aircraft, and man-made transmissions (e.g., radar). However, most of this interference can be avoided or flagged by monitoring and controlling the antenna pointing. Much of the remaining interference can be self-detected by the radiometer.

A brassboard radiometer was constructed and used to collect data during a horizon-scanning experiment. Radiometeric measurements and calculations from this experiment show excellent agreement and give confidence in our modeling. Furthemore, the measurements demonstrated that an AWR antenna only has to be pointed above the horizon by less than the antenna beamwidth to prevent loss of sensitivity due to earth surface radiation.

Although we have not been able to obtain detailed technical information from vendors of AWR, planning the addition of a radiometer mode to a typical X-band AWR was investigated. Calculations show that severe weather updates from this radiometer can be obtained at a minimum rate of about 2 Hz for 48 separate cells in $90°\ (\mathrm{azimuth}) \times 30°(\mathrm{elevation})$ sector forward of the aircraft.

3 Polarimetry

Review of Weather Radar Polarimetry

Current aircraft weather radars collect radar reflectivity (power) and Doppler velocity mean and standard deviation (changes in signal phase) at horizontal linear polarization. Hazardous weather conditions are identified by high reflectivity and/or by elevated velocity standard deviation (high turbulence or sheer). Reflectivity however is unreliable in severe weather conditions, because rain attenuation can mask severe weather cores and icing hazard (freezing rain) for example is not necessarily accompanied by elevated spectrum width. Dual-polarization radar can measure additional radar parameters that can be used to correct for signal attenuation in rain and can identify mixed phase precipitation such as hail (and the melting layer).

The polarization of a radar system refers to the orientation of the electric field oscillations, perpendicular to the transverse wave's direction of propagation. Current weather radars operate using horizontally polarized antennas, so when the radar is pointed towards the horizon, the electric field oscillates in the horizontal plane as shown in the first (left) graphics of Figure 19. The transmitted field of dual-polarization radar, shown in the second (right) graphics of Figure 19, uses both horizontal and vertical polarized fields. The horizontally polarized filed scattering most influenced by the horizontal cross section of particles, while the vertical polarization "sees" the vertical dimension. Small raindrops are close to perfect spheres due to the surface tension, but larger deform and often modeled as oblate spheroid. This deformation is illustrated in Figure 20. When only small hydrometeors are present in a range cell of polarimetric radar, the backscattering, attenuation and phase propagation is approximately same at H and V polarization. But when larger raindrops are present, the H-pol radar pulse will reflect stronger, attenuate more and phase propagation will be slower than V-pol. Consequently, the received power ratio (Z_{dr}) and the relative phase (Φ_{pd}) between H and V-polarized received signal contain information on hydrometeor size. The phase center of mixed phase and non-water particles also different at V and H-polarization, so mixed phase precipitation (hail and melting band) and ground debris can be effectively detected and differentiated from rain and drizzle using H and V signal correlation (ρ_{HV}). The following sections describe the polarimetric radar parameters commonly used for characterizing precipitation.

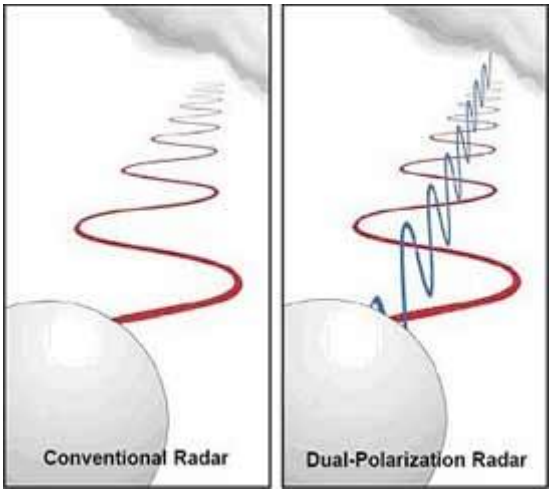

Figure 19. Dual polarization technology gives additional information on hydrometeor size, shape and composition to allow the estimation of rain rate, signal attenuation and the detection of hail. Source: NOAA

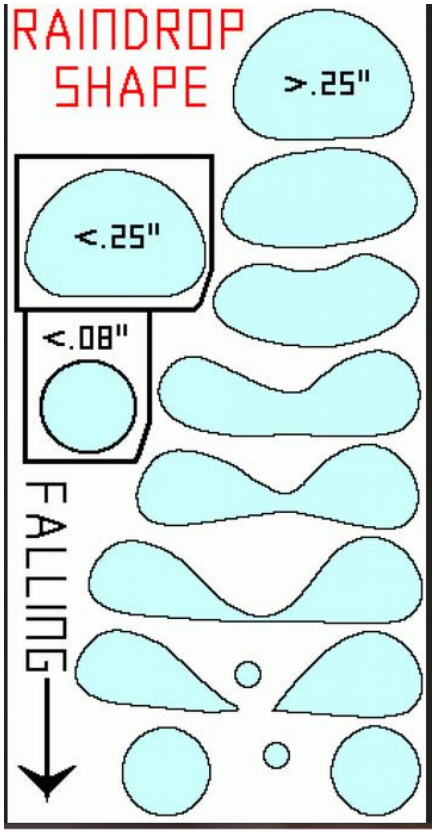

Figure 20. Raindrop shape primarily depends on size. Larger raindrops also have significant shape oscillations and often break apart.

3.1.1 DIFFERENTIAL PHASE SHIFT (Φ_{DP})

Φ_{DP} is the difference in the returned phase of the vertical and horizontal returns. The difference in return phase is greater from areas of large oblate spheroid drops because the horizontal pulses are slowed slightly more than the vertical pulses. This slight difference is enhanced by range from the radar. It is generally regarded that Φ_{DP} is best used in its range derivative form: K_{DP}.

3.1.2 SPECIFIC DIFFERENTIAL PHASE SHIFT (KDP)

K_{DP} is the range derivative of Φ_{DP} in units of deg/km. It is generally immune to large hail and thus is considered a useful indicator of actual rain rates and thus attenuation. Larger values indicate higher rain rates and higher attenuation. Light rain containing smaller, non-oblate spheroids results in very little return phase differences.

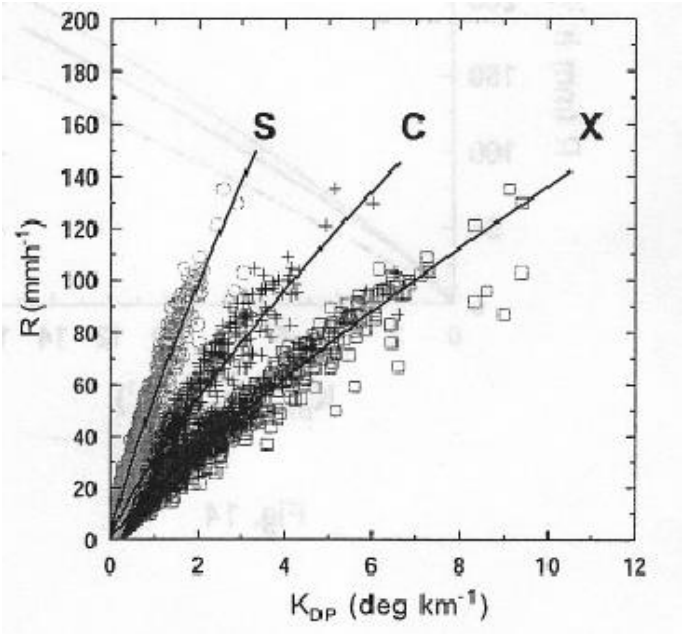

Figure 21. Dependence of Rain Rate - K_{dp} relations on radar frequency, (from Park, S.-G., Maki, M., Iwanami, K., Bringi, V.N., Chandrasekar, V., 2005. Correction of radar reflectivity and differential reflectivity for rain attenuation at X band. Part I: theoretical and empirical basis. *J. Atmos. Ocean. Tech.*. 22, 1621–1632.).

3.1.3 DIFFERENTIAL REFLECTIVITY (Z_{DR})

Z_{DR} is ten times the log of the ratio of the horizontal and vertical reflectivity return from a sample volume. Large drops are oblate spheroids and have increasingly larger returns from the horizontal pulses compared with the vertical pulses. For Z_{DR} over 6 dB, the drop diameters are exceeding 8 mm. Drops with diameters under about 0.5 mm have Z_{DR} about zero. Unfortunately, hail also has a Z_{DR} of around zero. Generally, snow has a low Z_{DR} independent of shape due to its small dielectric constant. Z_{DR} is sensitive to drop size, but inversely to propagation through rain with larger raindrops. So the observed Z_{DR} first has to be corrected for differential attenuation and then usually combined with K_{dp} (specific differential phase shift and/or Z (reflectivity) to estimate rain rate/attenuation. The linear reflectivity ratio is usually differentiated from the LOG ratio by using lower case "dr":

$$Z_{DR} = 10\log_{10}\left(Z_{dr}\right) \quad \textbf{(26)}$$

3.1.4 CORRELATION COEFFICIENT (ρ_{HV})

ρ_{HV} is a measure of the correlation of the returned power from the horizontal and vertical pulses. Typical meteorological values are near unity with a very small variation. In regions of non-uniform scatterers, such as mixed phase areas (i.e. – melting layers), the ρ_{HV} is lower. Ground clutter and airborne debris also have lower values as shown in middle image in the top row of Figure 22. ρ_{HV} is rather used for scatterer identification than quantitative retrieval.

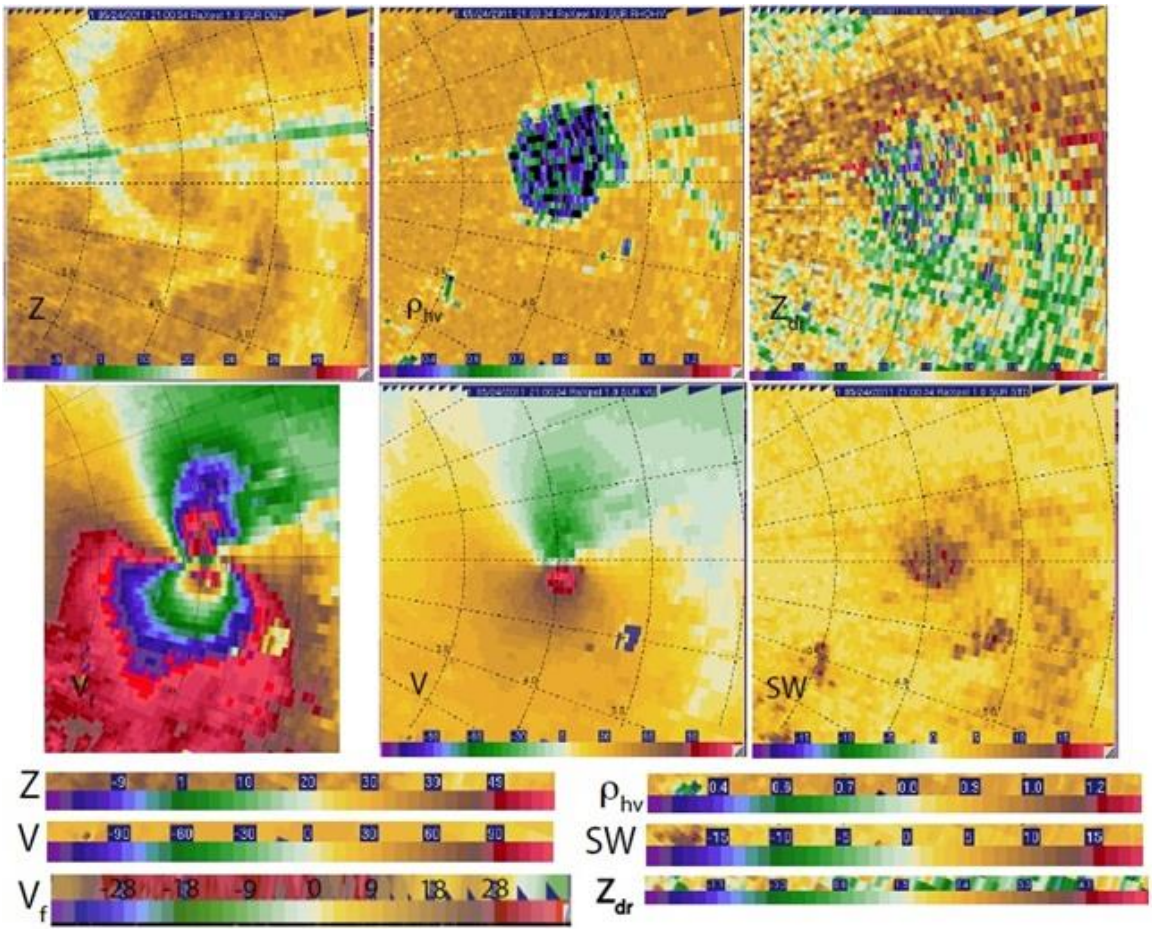

Figure 22. Example of X-band polarimetric radar data collected at low elevation angle in a tornado: Reflectivity (top-left), ρ_{hv} debris signature (top-middle), spectrum width (top-right), Doppler velocity folded (bottom-left and) and un-folded (bottom-middle), Z_{DR} (bottom-right).

Rain Rate Estimation from X-band Polarimetric Radar Parameters

Rain rate is highly correlated with attenuation, so existing models for estimating rain rate from X-band polarimetric radar parameters can be used to correct for attenuation.

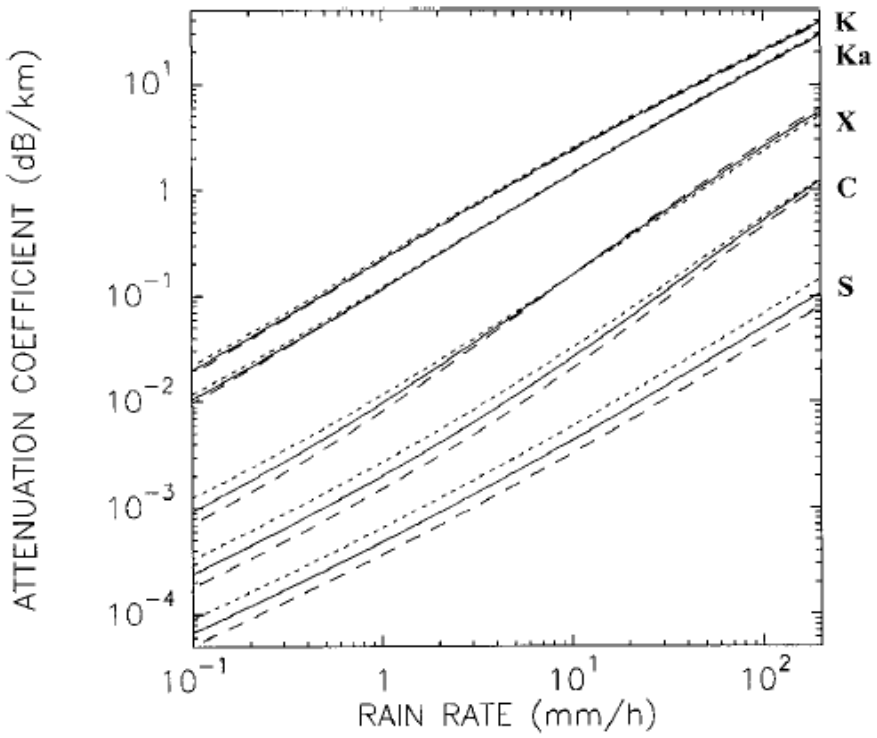

Figure 23. examples of k–R relationships established using Mie theory (spherical raindrops) for the K- (0.86 cm), Ka- (1.15 cm), X- (3.2 cm), C- (5.6 cm), and S-band (10 cm) wavelengths and the for raindrop temperatures T=0˚C (dotted line), T=10˚C (continuous line), and T=20˚C (dashed line). From [12].

3.1.5 Rain Rate – Z Estimator

$$R = 100 Z_{eh}^{1.76} \quad \textbf{(27)}$$

from [13] **,**

where R is rain rate in mm/hr, and

Z_{eh} is equivalent reflectivity factor at horizontal polarization, in units of mm^6/m^3.

3.1.6 Rain Rate – K_{dp} Estimator

(28)
$$R = aK_{DP}^{b},$$

where

K_{dp} is the specific differential phase shift in units of deg/km, and

a = ~16.5 and b = ~ 0.75 but slightly dependent on drop size distribution.

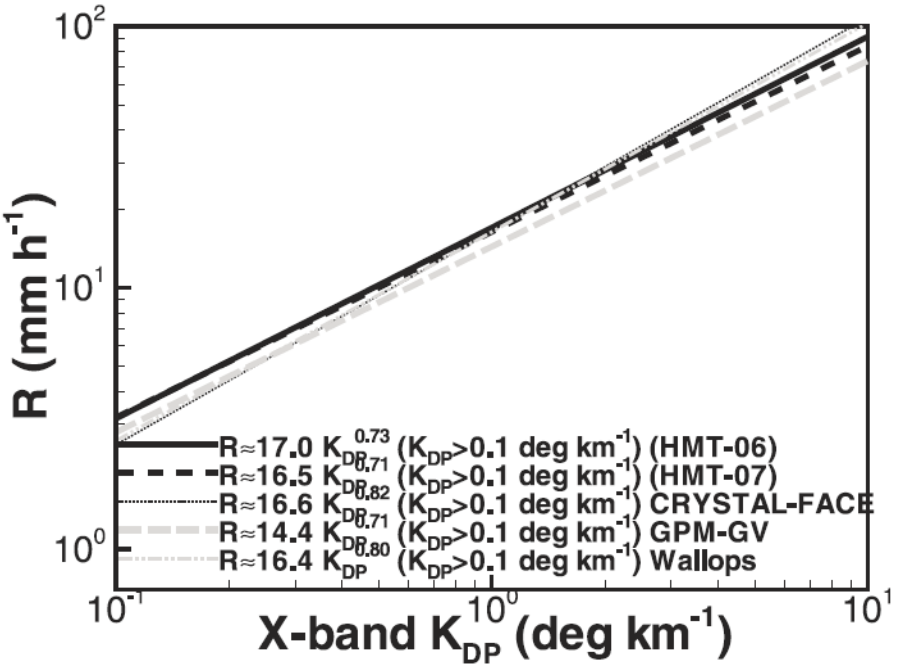

Figure 24. R – Kdp power-law fit relations using size distributions collected in various field campaigns. From [14].

3.1.7 Rain Rate – Z, Zdr Estimator

(29)
$$R = 0.0039 Z_{eh}^{1.07} Z_{dr}^{5.97},$$

(from [18])

where

Z_{dr} is differential reflectivity in linear units; $Z_{DR} = 10\log_{10}(Z_{dr})$.

3.1.8 Rain Rate – Z, Z_{dr}, K_{dp} Estimator

$$R = a \cdot K_{dp}^{b} \cdot 10^{c \cdot Z_{eh} + d \cdot Z_{DR}} \quad \textbf{(30)}$$

(from [19])

where the a, b, c, d coefficients are given in Table 2.

Table 2. Coefficients of Equation (30) rain rate estimator *(K_{DP}, Z, Z_{DR})*.

Rain type	a	B	C	D
Stratiform	0.009	−0.173	0.103	−0.653
Convective	0.198	0.4405	0.035	−0.036

3.1.9 Comparison of various rain rate estimators

The various rain rate estimators are compared in Figure 25 for sensitivity to variability in drop size distribution. As expected, the reflectivity only estimator is very poor in conditions anything other than the lowest rain rates. The estimation improves, as more parameters are included with reflectivity. But only error free parameters are considered in these simulated results, while Z and Z_{dr} are susceptible to error due to unaccounted for attenuation and differential attenuation. K_{dp} on the other hand is a much easier to measure accurately, so the upper right rain rate estimator plot is closer to what can be realistically expected than the two lower row plots of the more complex models.

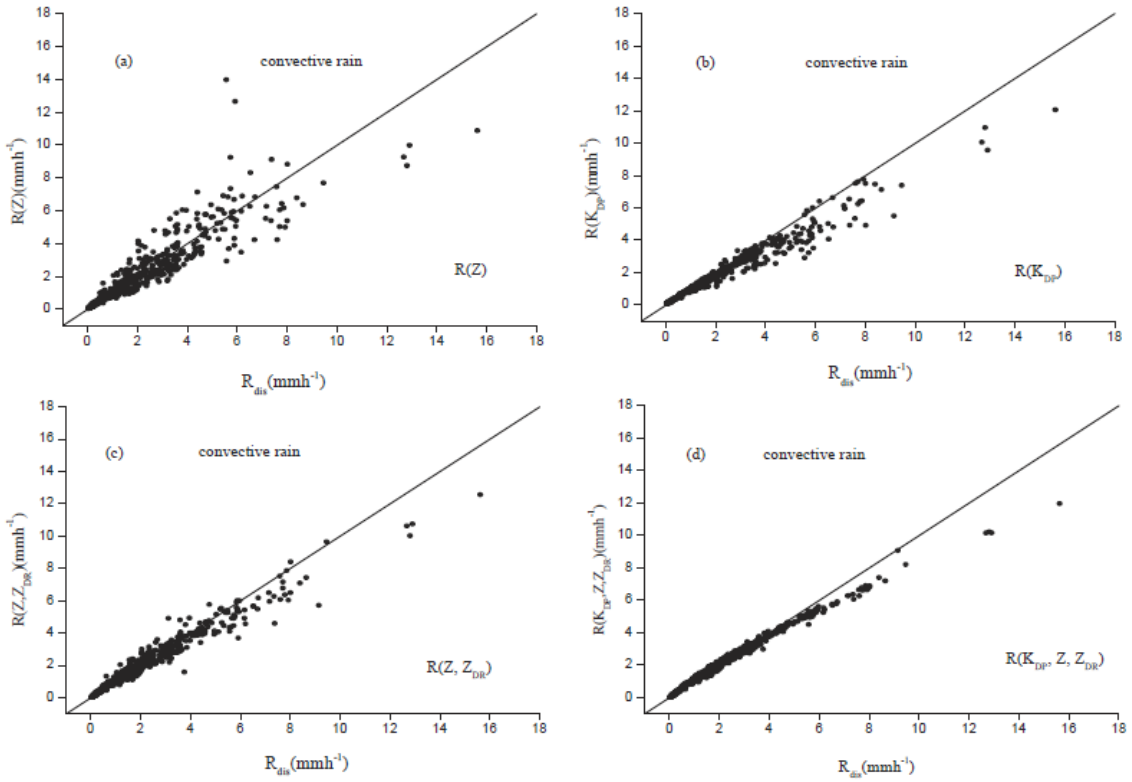

Figure 25. Scatter plots of rain rain calculated from measured drop size distribution and estimated from four types of rain rate estimators a) R(Z), b) R(Z, Zdr), c) R(Kdp), d) R(Kdp, Z, Zdr). From [19].

Dual Polarized Aircraft Weather Radar Antenna.

The cost of upgrading current AWRs to dual-polarized capability is relatively inexpensive. The transmitted pulse has to be equally divided to the Vertical and Horizontally polarized antenna ports and a second receiver has to be added to the radar. The signal processing is well-documented and straight forwards and polarimetric radar parameters, such as differential reflectivity (Z_{dr}) and specific differential phase shift (K_{dp}) can be effectively used to correct for attenuation in moderate to heavy rain conditions. The only missing (*enabling*) technology is a dual-pol antenna, similar in quality to the current standard flat plate waveguide array. A dual-pol slotted waveguide array antenna has been patented by Rockwell Collins: http://www.google.com/patents/US8098189 but performance data was not available to assess potential polarimetric measurement accuracy, at the time of this report.

Past aircraft weather radars used magnetron transmit sources that required waveguide antenna array technology to be able to transmit high peak power. Modern weather radars use lower peak power solid state transmitters, which opens up the possibility of using microstrip antenna arrays. Some attempts have been made to develop lightweight dual-pol X-band microstrip antennas. In 2001 a design study was conducted by Antenna Design Associates to develop a Multi-Frequency (X, Ka and W-band) and dual-pol at X-band aircraft weather radar antenna. It concluded that a two-layer aperture coupled microstrip array technology (shown in Figure 26) could be used to develop a 1' to 2' diameter, medium power (<10 kW peak power) flat, lightweight X-band aircraft weather radar antenna. Larger antennas with narrower beam-width would be also possible, but without much improvement in gain due to increasing losses, with

increasing antenna size, in the microstrip substrate. More recently, a small experimental dual-pol microstrip array (~5" diameter, 25 deg beam width, 19 dB gain) was developed by [26].

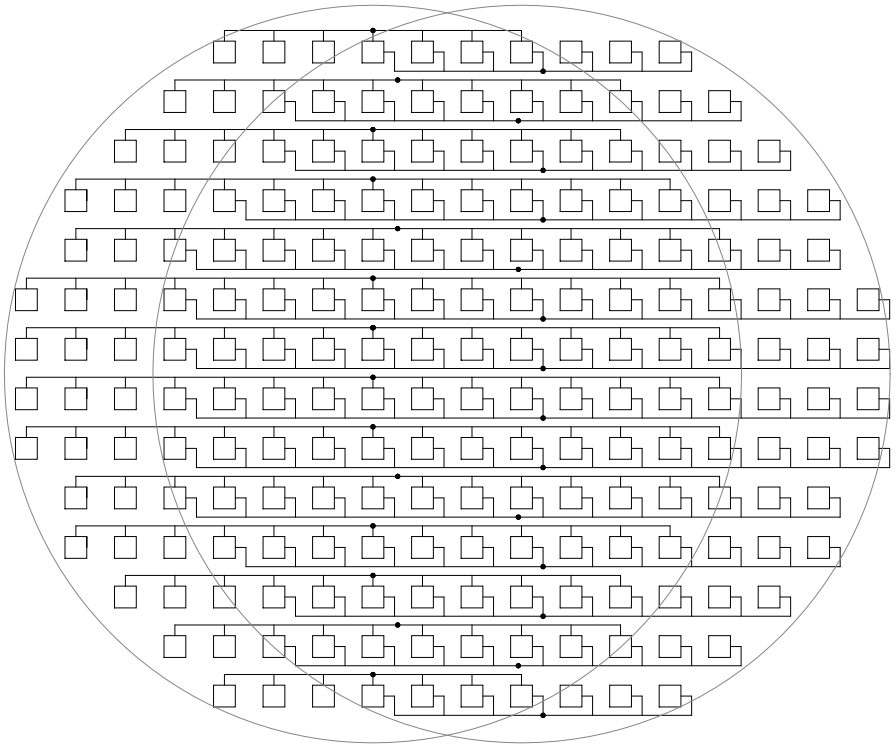

Figure 26. Dual-polarized X-band microstrip antenna array with interleaved coplanar feed (coax feed points are shown as solid circles; offset = 6.96 cm = 0.202D). This design also incorporates a 0.2D V-H aperture offset for spaced antenna transverse wind measurement. A waveguide power divided network is also required in the rear of the antenna.

3.1.10 Antenna requirements

Current airborne weather radars use flat plate (or box-horn) array antennas, like shown in the left pane of Figure 27. These antennas are ideal for airborne radar applications due to their light weight, low profile and excellent electrical properties (low loss and low sidelobes), but are not available in dual-polarization version (no information is available on the Rockwell Collins patent of a dual-pol slotted waveguide array, http://www.google.com/patents/US8098189). Microstrip antennas are also relatively light weight and have low profile, but can be developed with dual polarization capability, so they might be a potential candidate for future dual-polarized aircraft weather radars. The following discussion is on the required specifications of a dual-pol AWR antenna for hydrometeor classification and implementation of polarimetric rain retrieval algorithms.

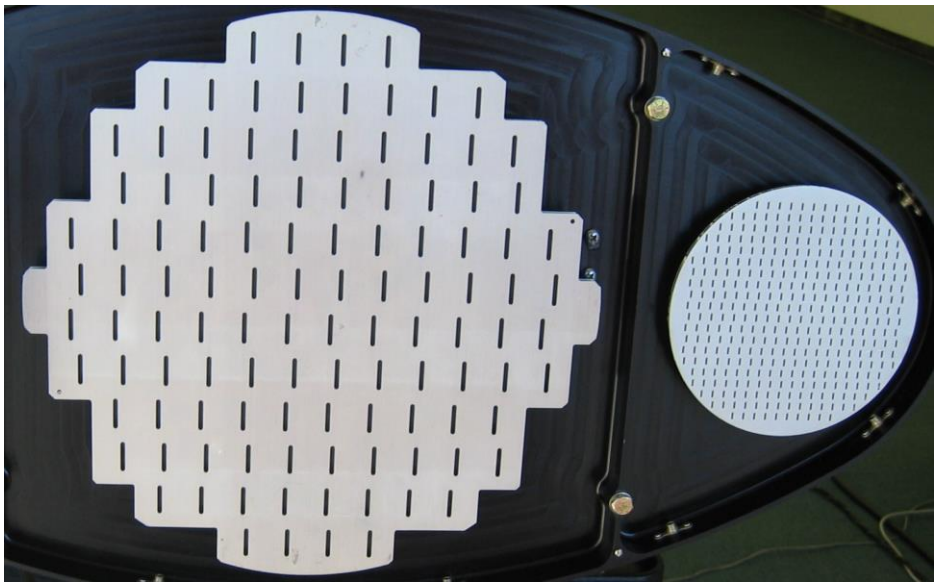

Figure 27. Various size flat plate (box-horn) waveguide array antennas.

An ideal weather radar antenna has low loss, low sidelobes, close to the ratio of wavelength (λ) and antenna diameter (D), λ/D (rad) half power beamwidth (high gain for a given diameter) and if polarimetric, then the orthogonally polarized ports have high isolation, but co-located beams. The high gain is important for sensitivity. The low sidelobes (>25 dB one way) are important to ensure confidence in the location of the source of the measurements. Sidelobe return from a strong reflectivity core can severely bias an observation. Fortunately most well designed antennas have at least 20-25 dB first sidelobe levels and sidelobes further from the main beam quickly drop. But more importantly, with single antenna radar, the antenna is used for transmission and reception, so interference from a precipitation core is attenuated by twice the sidelobe suppression level in dB. Consequently an antenna with a 25 dB sidelobe will suppress return from the direction of that sidelobe by 50 dB. Since most airborne weather radars rarely measure above 50 dB signal to noise ratio, a 25 dB first sidelobe level is usually sufficient.

Co-located V and H-pol beams are essential for useful ρ_{HV} measurements, with correlations varying from 0.99 in light rain and drizzle to 0.90 in hail and as low as 0.80 in mixed phased precipitation (melting layer / bright band). Consequently the vertical and horizontally polarized beam patterns of a dual-pol antenna should be 99% co-located (overlapped).

Quantifying the effect of polarization isolation on the measurement accuracy of polarimetric radar parameters and consequently on the quality of the retrieved rain rate or attenuation is more complicated. Wand and Chandrasekar investigated this problem [21], but only plots of the results were published, not the complete expressions. Consequently the effect of finite antenna isolation on rain and attenuation estimation required us to re-examine the problem:

The received field of simultaneous V and H radar transmission can be described as

(31)
$$[R] = [A]^T [P][S][P][A] \begin{bmatrix} 1 \\ e^{j\theta_T} \end{bmatrix},$$

where

θ_T is transmitter phase difference between the V and H channels, and [*A*] is the antenna distortion matrix, accounting for antenna polarization isolation, *I*, V-channel phase shift and coupling phase shifts θ_{HV} and θ_{VH}:

$$[A]=\begin{bmatrix} 1 & \sqrt{I}e^{j\theta_{HV}} \\ \sqrt{I}e^{j\theta_{VH}} & e^{j\theta_{VV}} \end{bmatrix}, \tag{32}$$

[S] is the target scattering matrix:

$$[S]=\begin{bmatrix} S_{HH} & S_{HV} \\ S_{VH} & S_{VV} \end{bmatrix}, \tag{33}$$

and *[P]* is the propagation distortion matrix, accounting for differential phase shift (Ψ_{dp}):

$$[P]=\begin{bmatrix} 1 & 0 \\ 0 & e^{-j\Psi_{dp}/2} \end{bmatrix}. \tag{34}$$

The resulting received voltages from the H and V antenna ports are:

$$R_H = \begin{array}{c} S_{HH}\left(1+\sqrt{I}e^{j\theta_{HV}}e^{j\theta_T}\right)+S_{HV}e^{-j\Psi_{dp}/2}\left(e^{j\theta_{VV}}e^{j\theta_T}+\sqrt{I}e^{j\theta_{VH}}\right)+ \\ S_{VH}e^{-j\Psi_{dp}/2}\sqrt{I}e^{j\theta_{HV}}\left(1+\sqrt{I}e^{j\theta_{HV}}e^{j\theta_T}\right)+S_{VV}e^{-j\Psi_{dp}}\sqrt{I}e^{j\theta_{HV}}\left(e^{j\theta_{VV}}e^{j\theta_T}+\sqrt{I}e^{j\theta_{VH}}\right) \end{array} \tag{35}$$

and

$$R_V = \begin{array}{c} S_{HH}\sqrt{I}e^{j\theta_{VH}}\left(1+\sqrt{I}e^{j\theta_{HV}}e^{j\theta_T}\right)+S_{HV}\sqrt{I}e^{j\theta_{VH}}e^{-j\Psi_{dp}/2}\left(e^{j\theta_{VV}}e^{j\theta_T}+\sqrt{I}e^{j\theta_{VH}}\right)+ \\ S_{VH}e^{j\theta_{VV}}e^{-j\Psi_{dp}/2}\left(1+\sqrt{I}e^{j\theta_{HV}}e^{j\theta_T}\right)+S_{VV}e^{j\theta_{VV}}e^{-j\Psi_{dp}}\left(e^{j\theta_{VV}}e^{j\theta_T}+\sqrt{I}e^{j\theta_{VH}}\right) \end{array} \tag{36}$$

These expressions can be simplified by eliminating the second order terms with $\left(\sqrt{I}\right)^2$, $S_{VH}\sqrt{I}$ and $S_{HV}\sqrt{I}$:

$$R_H = S_{HH}\left(1+\sqrt{I}e^{j\theta_{HV}}e^{j\theta_T}\right)+S_{HV}e^{-j\Psi_{dp}/2}e^{j\theta_{VV}}e^{j\theta_T}+S_{VV}e^{-j\Psi_{dp}}\sqrt{I}e^{j\theta_{VV}}e^{j\theta_T}e^{j\theta_{HV}} \tag{37}$$

$$R_V = S_{VV}e^{-j\Psi_{dp}}e^{j\theta_{VV}}\left(e^{j\theta_{VV}}e^{j\theta_T}+\sqrt{I}e^{j\theta_{VH}}\right)+S_{VH}e^{-j\Psi_{dp}/2}e^{j\theta_{VV}}+S_{HH}\sqrt{I}e^{j\theta_{HV}}e^{j\theta_T} \tag{38}$$

The resulting becomes a simplified expression for the observed radar reflectivity factor $\hat{Z}$ by assuming that co-pol scattering is uncorrelated with cross-pol backscatter:

(39) $$R_H = S_{HH}\left(1+\sqrt{I}e^{j\theta_{HV}}e^{j\theta_T}\right)+S_{HV}e^{-j\Psi_{dp}/2}e^{j\theta_{VV}}e^{j\theta_T}+S_{VV}e^{-j\Psi_{dp}}\sqrt{I}e^{j\theta_{VV}}e^{j\theta_T}e^{j\theta_{HV}}$$

(40) $$R_V = S_{VV}e^{-j\Psi_{dp}}e^{j\theta_{VV}}\left(e^{j\theta_{VV}}e^{j\theta_T}+\sqrt{I}e^{j\theta_{VH}}\right)+S_{VH}e^{-j\Psi_{dp}/2}e^{j\theta_{VV}}+S_{HH}\sqrt{I}e^{j\theta_{HV}}e^{j\theta_T}$$

(41) $$\hat{Z}_H \propto \left\langle |R_H|^2 \right\rangle \approx Z_H\left(\begin{array}{l}1+\sqrt{I}\left(e^{j(\theta_{HV}+\theta_T)}+e^{-j(\theta_{HV}-\theta_T)}\right)+\\ \rho_{HV}\sqrt{\dfrac{I}{z_{dr}}}\left(e^{-j\Psi_{dp}}e^{j\theta_{VV}}e^{j\theta_T}e^{j\theta_{VH}}+e^{+j\Psi_{dp}}e^{-j\theta_{VV}}e^{-j\theta_T}e^{-j\theta_{VH}}\right)\end{array}\right),$$

and the complex exponentials combined to simplify:

(42) $$\hat{Z}_H \approx Z_H\left[1+2\sqrt{I}\cos\left(\theta_{HV}+\theta_T\right)+2\rho_{HV}\sqrt{\frac{I}{z_{dr}}}\cos\left(\Psi_{dp}-\theta_{VV}-\theta_T-\theta_{VH}\right)\right],$$

where z_{dr} is the differential reflectivity in linear units $z_{dr}=\dfrac{Z_H}{Z_V}$; $Z_{DR}=10\log_{10}\left(z_{dr}\right)$.

So the error factor bound of the measured reflectivity, E_{Z_H}, is

(43) $$E_{Z_H}=1\pm 2\sqrt{I}\left(1+\frac{\rho_{HV}}{\sqrt{zdr}}\right),$$

and similarly for the vertically polarized reflectivity:

(44) $$\hat{Z}_V \approx Z_V\left[1+2\sqrt{I}\cos\left(\Psi_{dp}-2\theta_{VV}-\theta_T+\theta_{VH}\right)+2\rho_{HV}\sqrt{I\times z_{dr}}\cos\left(\Psi_{dp}-2\theta_{VV}+\theta_{HV}\right)\right]$$

(45) $$E_{Z_V}=1\pm 2\sqrt{I}\left(1+\rho_{HV}\sqrt{z_{dr}}\right).$$

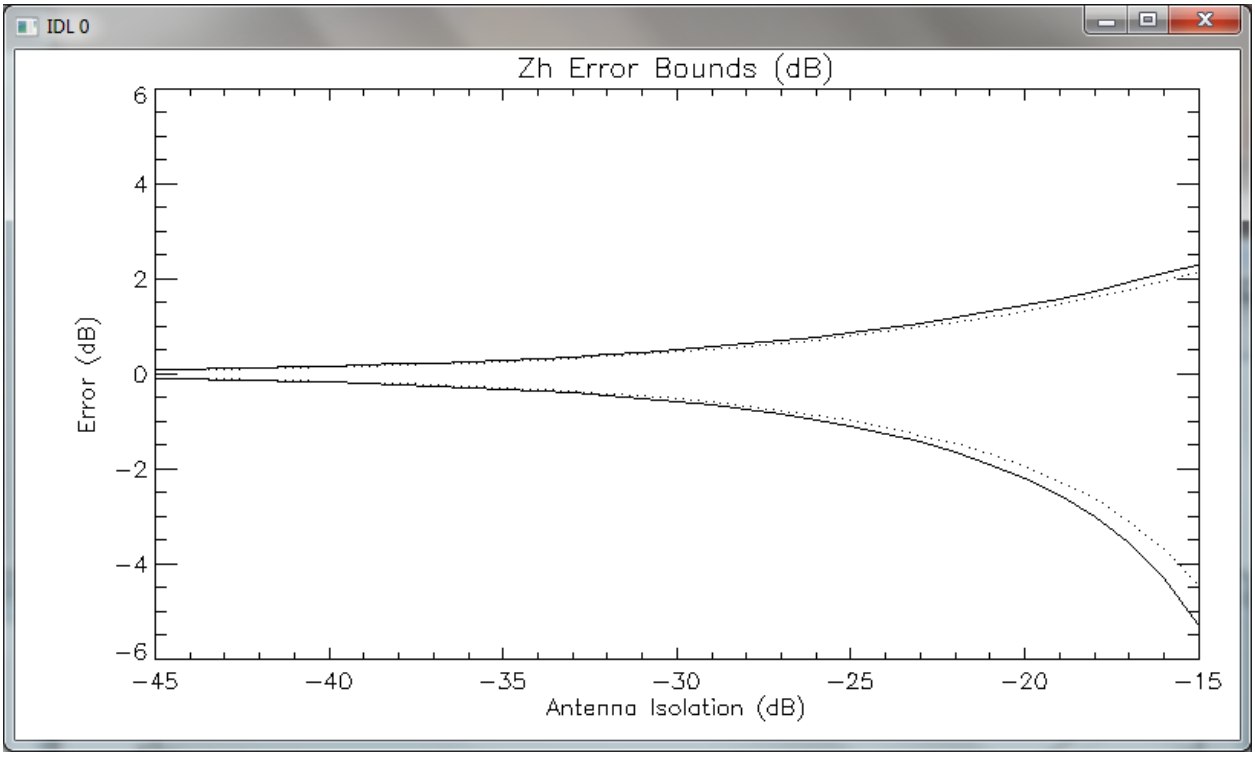

Figure 28. Estimated reflectivity error bounds as a function of antenna polarization isolation. Solid lines are for rain (ρ_{HV} = 0.98) and dashed lines for mixed phase (ρ_{HV} = 0.9).

The differential reflectivity, z_{dr}, is the ratio of the H and V reflectivity factor (assumed that $\theta_{HV} = \theta_{VH}$ to simplify):

$$\widehat{z}_{dr} = z_{dr} \frac{1 + 2\sqrt{I}\cos\left(\theta_{HV} + \theta_T\right) + 2\rho_{HV}\sqrt{\frac{I}{z_{dr}}}\cos\left(\Psi_{dp} - \theta_{VV} - \theta_T - \theta_{VH}\right)}{1 + 2\sqrt{I}\cos\left(\Psi_{dp} - 2\theta_{VV} - \theta_T + \theta_{VH}\right) + 2\rho_{HV}\sqrt{I \times z_{dr}}\cos\left(\Psi_{dp} - 2\theta_{VV} + \theta_{HV}\right)} \quad \textbf{(46)}$$

and so the z_{dr} error factor range without phase control over the transmitted field,

$$\frac{1 - 2\sqrt{I}\left(1 + \frac{\rho_{HV}}{\sqrt{zdr}}\right)}{1 + 2\sqrt{I}\left(1 + \rho_{HV}\sqrt{z_{dr}}\right)} < E_{z_{dr}} < \frac{1 + 2\sqrt{I}\left(1 + \frac{\rho_{HV}}{\sqrt{zdr}}\right)}{1 - 2\sqrt{I}\left(1 + \rho_{HV}\sqrt{z_{dr}}\right)}. \quad \textbf{(47)}$$

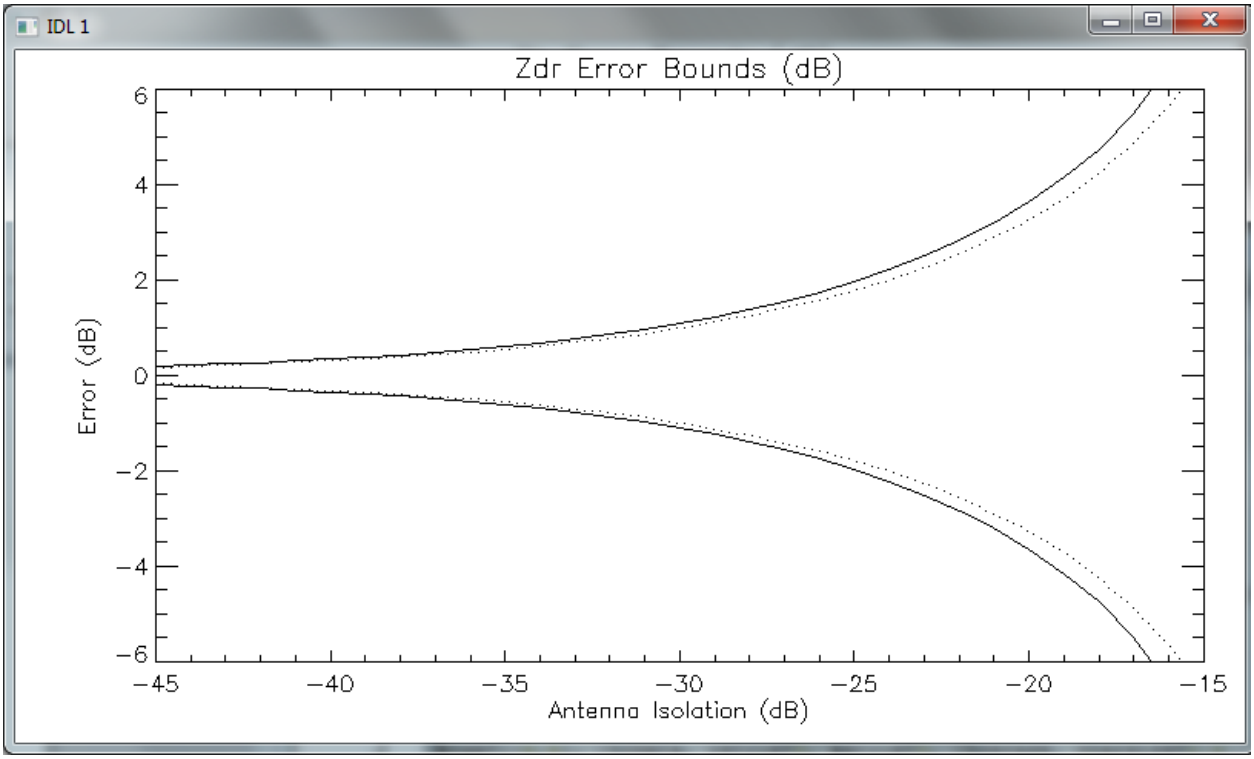

Figure 29. Estimated differential reflectivity error bounds as a function of antenna polarization isolation for rain (solid; ρ_{HV} = 0.98) and mixed phase precipitation (dashed; ρ_{HV} = 0.8).

Note that if the antenna leakage and propagation phase shifts are the same ($\theta_{VH} = \theta_{HV} = \theta_{VV} = 0$) and if the differential phase shift is small, then the error can be dramatically reduced by transmitting the V and H field components 90 deg out of phase:

$$\hat{Z}_H \approx Z_H \left[1 + 2\sqrt{I}\cos\left(\pi/2\right) + 2\rho_{HV}\sqrt{\frac{I}{z_{dr}}}\cos\left(\pi/2\right) \right] = Z_H \tag{48}$$

$$\widehat{z}_{dr} \approx z_{dr} \frac{1 + 2\sqrt{I}\cos\left(\pi/2\right) + 2\rho_{HV}\sqrt{\frac{I}{z_{dr}}}\cos\left(\pi/2\right)}{1 + 2\sqrt{I}\cos\left(\pi/2\right) + 2\rho_{HV}\sqrt{I \times z_{dr}}\cos\left(\pi/2\right)} = z_{dr} \tag{49}$$

Differential $\left(\Psi_{dp}\right)$ and Specific Differential Phase $\left(K_{dp}\right)$ are defined as:

$$\Psi_{dp} = \arg\left[R_H R_V^*\right] \tag{50}$$

and

$$K_{dp} = \frac{d\Psi_{dp}}{dr}, \tag{51}$$

where *r* is range.

The measured Differential Phase $\widehat{\Psi}_{dp}$ can be expressed as a sum of the measurement error $\left(\Delta\Psi_{dp}\right)$ and Ψ_{dp}:

$$\widehat{\Psi}_{dp} = \Psi_{dp} + \Delta\Psi_{dp}. \tag{52}$$

Similarly, the measured $\widehat{K}_{dp}$ can be written as:

$$\widehat{K}_{dp} = \frac{d\widehat{\Psi}_{dp}}{dr} = \frac{d\Psi_{dp}}{dr} + \frac{d\Delta\Psi_{dp}}{dr} = \frac{d\Psi_{dp}}{dr} + \frac{d\Delta\Psi_{dp}}{d\Psi_{dp}}\frac{d\Psi_{dp}}{dr} = K_{dp}\left(1 + \frac{d\Delta\Psi_{dp}}{d\Psi_{dp}}\right). \tag{53}$$

$$\widehat{\Psi}_{dp} = \arg\left[R_H R_V^*\right] \tag{54}$$

(55)

$$\widehat{\Psi}_{dp} = \arg\left[\left(S_{HH}\left(1+\sqrt{I}e^{j\theta_{HV}}e^{j\theta_T}\right)+S_{HV}e^{-j\Psi_{dp}/2}e^{j\theta_{VV}}e^{j\theta_T}+S_{VV}e^{-j\Psi_{dp}}\sqrt{I}e^{j\theta_{VV}}e^{j\theta_T}e^{j\theta_{HV}}\right)\times\right.$$
$$\left.\left(S_{VV}e^{-j\Psi_{dp}}e^{j\theta_{VV}}\left(e^{j\theta_{VV}}e^{j\theta_T}+\sqrt{I}e^{j\theta_{VH}}\right)+S_{VH}e^{-j\Psi_{dp}/2}e^{j\theta_{VV}}e^{j\theta_T}+S_{HH}\sqrt{I}e^{j\theta_{HV}}e^{j\theta_T}\right)^*\right]$$

By eliminating the second order terms and terms without Ψ_{dp}, and replacing $\left\langle S_{HH}\times S_{VH}^*\right\rangle = Z_H\sqrt{\frac{LDR}{N}}$, where *N* is the number of independent samples averaged and *LDR* is the linear depolarization ratio, the differential phase expression can be simplified as:

$$\widehat{\Psi}_{dp} \approx \arg\left\{Z_H\left[\begin{array}{l}\rho_{HV}e^{j\Psi_{dp}}e^{-j\theta_{VV}}\left(e^{-j\theta_{VV}}e^{-j\theta_T}+\sqrt{I}\left(e^{j\theta_{HV}}e^{j\theta_T}e^{-\theta_{VV}}e^{-j\theta_T}+e^{-j\theta_{VH}}\right)\right)+\\ \sqrt{\frac{LDR}{N}}e^{j\Psi_{dp}/2}e^{-j\theta_{VV}}e^{-j\theta_T}\left(1+\sqrt{\frac{1}{Z_{dr}}}\right)\end{array}\right]\right\} \tag{56}$$

If we can assume that the antenna cross-pol and co-pol phase shifts are the same, such that $\theta_{VH} = \theta_{HV} = \theta_{VV} = 0$, $\rho_{HV} \approx 1$ and $Z_{dr} \approx 1$ then

(57) $$\widehat{\Psi}_{dp} \approx \arg\left\{ e^{j\Psi_{dp}} e^{-j\theta_T} \left(1 + 2\sqrt{I} e^{j\theta_T} + 2\sqrt{\frac{LDR}{N}} e^{j^{-\Psi_{dp}/2}} \right) \right\}$$

(58) $$\widehat{\Psi}_{dp} \approx \arctan\left(\frac{\sin\left(\Psi_{dp} - \theta_T\right) + 2\sqrt{I}\sin\left(\theta_T\right) + 2\sqrt{\frac{LDR}{N}}\sin\left(-\Psi_{dp}/2\right)}{\cos\left(\Psi_{dp} - \theta_T\right) + 2\sqrt{I}\cos\left(\theta_T\right) + 2\sqrt{\frac{LDR}{N}}\cos\left(-\Psi_{dp}/2\right)} \right).$$

Assuming that $2\sqrt{I} << 1$ and $2\sqrt{\frac{LDR}{N}} << 1$, we can further simplify as

(59) $$\widehat{\Psi}_{dp} \approx \Psi_{dp} - \theta_T + 2\sqrt{I}\sin\left(\theta_T\right) + 2\sqrt{\frac{LDR}{N}}\sin\left(-\Psi_{dp}/2\right)$$

(60) $$\Delta\Psi_{dp} = \widehat{\Psi}_{dp} - \Psi_{dp} = -\theta_T + 2\sqrt{I}\sin\left(\theta_T\right) + 2\sqrt{\frac{LDR}{N}}\sin\left(-\Psi_{dp}/2\right)$$

(61) $$\widehat{K}_{dp} = K_{dp}\left(1 + \frac{d\Delta\Psi_{dp}}{d\Psi_{dp}}\right) = K_{dp}\left(1 + 2\sqrt{\frac{LDR}{N}}\cos\left(\Psi_{dp}/2\right)\right)$$

This result indicates that the Specific Differential Phase $\left(K_{dp}\right)$ error bounds are primarily affected by the target linear depolarization ratio (*LDR*) and averaging (*N*) as long as the antenna isolation is fairly good $\left(2\sqrt{I} << 1\right)$.

In most conditions $\widehat{\Psi}_{dp}$ will be small such that $\cos\left(\frac{\Psi_{dp}}{2}\right) \approx 1$, so the error is most likely positive:

(62) $$E_{K_{dp}} = 1 + 2\sqrt{\frac{LDR}{N}}$$

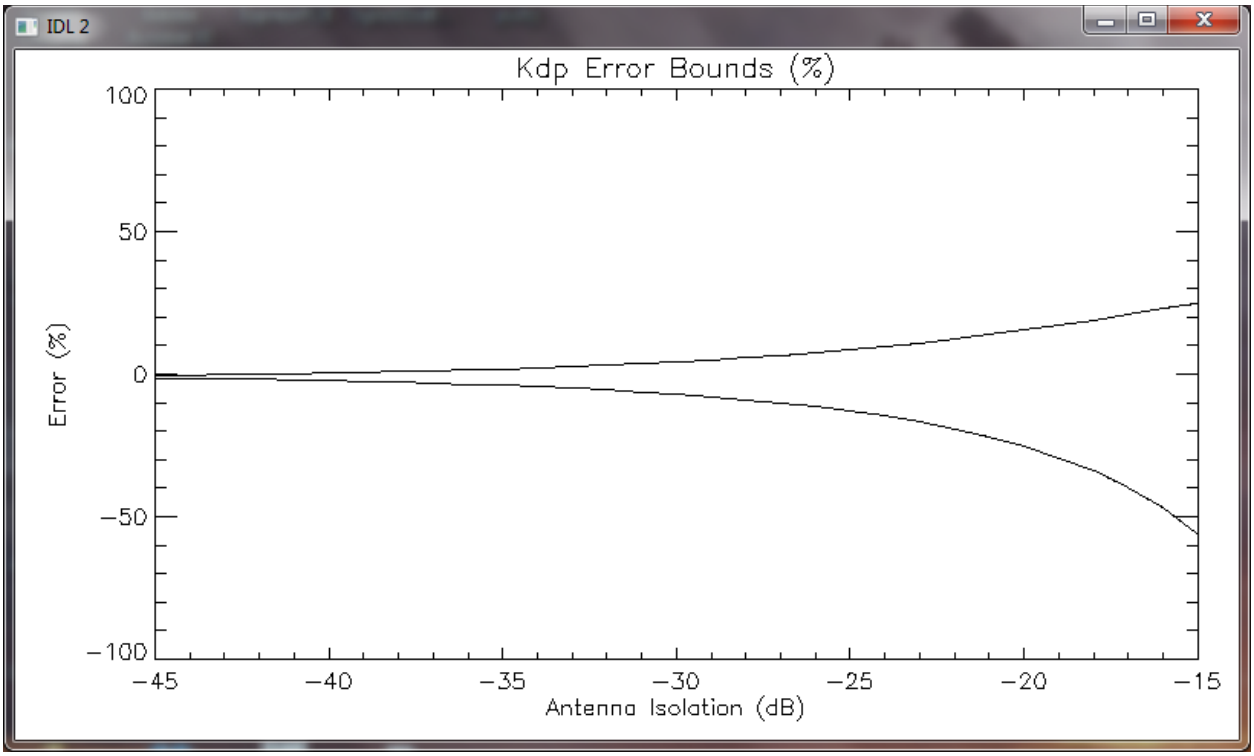

Figure 30. Estimated Kdp error bounds as a function of antenna isolation, using Equations (53 and (58. An LDR or 25 dB was used in the calculations.

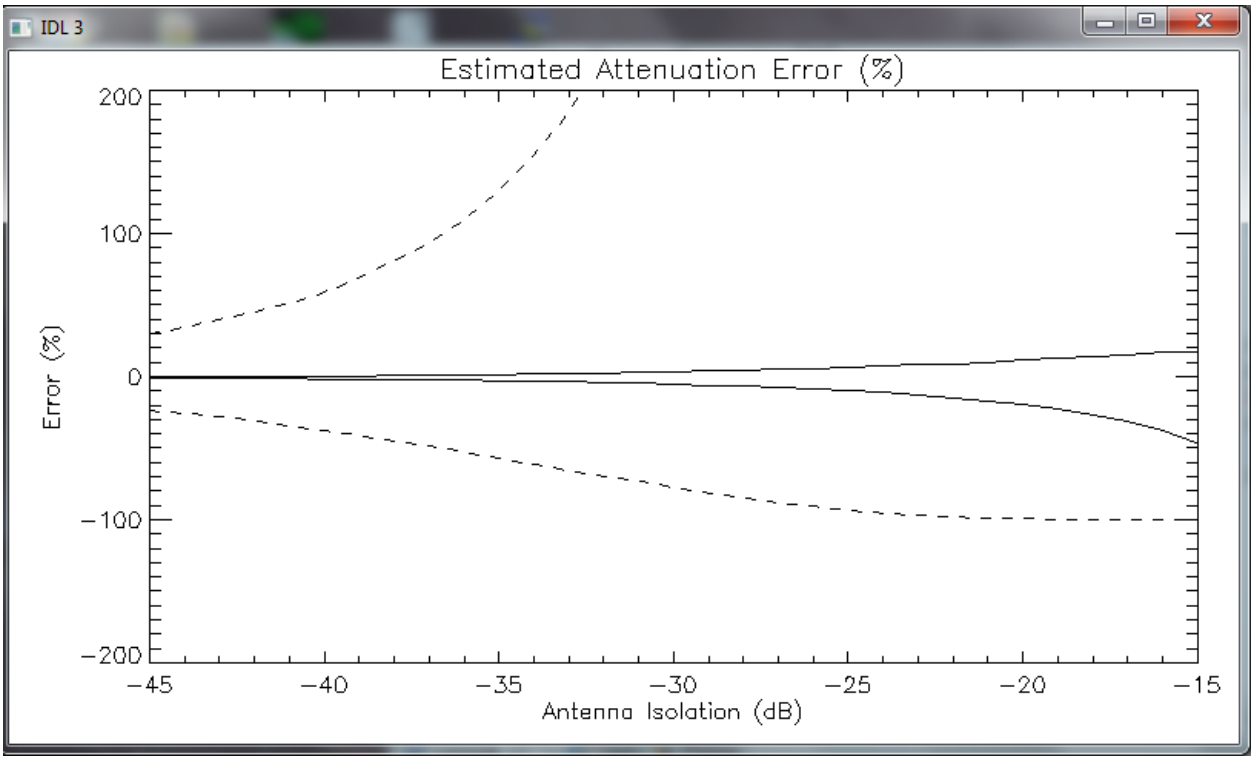

Figure 31. Estimated attenuation error bounds as a function of antenna isolation, based on the results of Figure 30, using Kdp (Equation (28 - solid lines) and Z-Zdr based estimators (Equation (29 – dashed lines).

The conclusion of the above analysis is that polarimetric antennas for airborne weather radars should have at least 25 dB (30 dB preferred) polarization isolation to be useful for estimating attenuation using the various retrieval methods. K_{dp}-based estimators can be effective with less isolation. The V and H components of the transmitted field should be phased close to 90˚ for best measurement quality.

4 Multi-Frequency Radar (MFR)

The task of adding another frequency to the current X-band AWR channel is significantly more complex and potentially more expensive than adding radiometric or polarimetric measurement capability. A second radar channel will likely require a separate antenna and radar electronics, although a dual frequency antenna, specific for airborne use, might be easier to develop than a lightweight, flat-plate dual-polarized X-band antenna. But most likely, only the data system and power supply sections could be shared. So why consider a second frequency?

The two most important frequency dependent factors influencing weather radar measurements are that backscattering efficiency of small scatterers increases as f^4 (Equation (80)) and attenuation coefficient as f^2 (Figure 48). Attenuation becomes more important with range so long-range weather radars are predominately lower frequency (relative to X-band) S-band (10 cm wavelength) in the US and C-band (5 cm) in Europe. On the other end of the weather radar spectrum, cloud research radars are usually Ka (1 cm) or W-band (3 mm) to maximize sensitivity at close range. A multi-frequency weather radar has two primary benefits:

1) A greater variety of weather conditions could be effectively measured. When the total path attenuation is high (due to long range and/or high attenuation rate), the lower frequency radar channel will be more effective, while higher frequency radar should have better sensitivity to small scatterers, when attenuation is less of a factor. Of course the availability of quality radar components and transmitter power are also important factors determining sensitivity at various frequencies.

2) The difference between radar parameters measured at two (or more) frequencies can be used to estimate cloud and precipitation properties. Particularly differential attenuation, derived from differential reflectivity gradient, can be highly correlated with attenuation and liquid water content, and can be used to better characterize weather hazards.

This section investigates the potential use of multiple frequencies with AWRs. First, sensitivity, back scattering efficiency and attenuation is investigated at a function of frequency. Then practical system parameters are considered along with a model of various cloud, drizzle and rain conditions, to simulate the frequency dependence of radar sensitivity, attenuation and measurement range in various weather conditions.

MFR Measurement Concept

4.1.1 Point Scattering

The transmitted power density, S, of a radar can be expressed as

$$S_t = \frac{P_t G}{4\pi r^2} \quad , (\mathrm{W/m^2}), \tag{63}$$

where P_t is the transmitted power in (W), G is the antenna gain and r is the distance to the point target

reflector in meters.

The power density captured by a point target and re-radiated towards the radar is

$$S_r = \frac{S_t \sigma}{4\pi r^2} = \frac{P_t G \sigma}{(4\pi)^2 r^4} \quad \text{, (W/m}^2\text{).} \tag{64}$$

The received power at the antenna feed is the product of the antenna effective aperture (A_{eff}) and the incident power density of the scattered field according to

$$P_r = A_{eff} S_r = A_{eff} \frac{P_t G \sigma}{(4\pi)^2 r^4} \quad , \tag{65}$$

and since

$$A_{eff} = G\lambda^2 / 4\pi \quad , \tag{66}$$

the received power can be written in the standard form of the radar range equation for a point target as

$$P_r = \frac{P_t G^2 \lambda^2 \sigma}{(4\pi)^3 r^4} \quad \text{, (W).} \tag{67}$$

The actual antenna aperture area, *A*, can be expressed as $A = A_{eff} n_A$ where n_A is the aperture efficiency so the radar range equation can be rewritten as:

$$P_r = \frac{P_t A^2 n_A^2 \sigma}{4\pi\lambda^2 r^4} \quad . \tag{68}$$

4.1.2 Volume Scattering

The radar range equation for a point target can be extended to a volume target by replacing σ with the product of volume reflectivity, η (m^2 / m^3) and the volume of a range cell, *V*. The range cell volume of a pulsed radar, with an approximately Gaussian shaped antenna pattern, may *be approximated as*

$$V = r^2 \frac{c\tau}{2} \int_0^{\pi} \int_0^{2\pi} f^2(\theta, \phi) \sin(\theta) d\theta d\phi = r^2 \frac{c\tau}{2} \pi \theta_{3dB}^2 / 8 \ln 2 \quad \text{, (} m^3\text{),} \tag{69}$$

where,

r is the range to the center of the volume cell in meters, θ and ϕ are azimuth and elevation angles

respectively, θ_{3dB} and ϕ_{3dB} are the half power antenna beamwidths in azimuth and elevation,

$$f = \exp(-\frac{4\ln(2)\theta^2}{\theta_{3dB}^2})\exp(-\frac{4\ln(2)\phi^2}{\phi_{3dB}^2}) \quad \textbf{(70)}$$

$c = 3\times10^8$ m/s, speed of light in free space,

$\tau =$ transmit pulse length (sec.).

For most weather radars, the antenna half power beamwidths in elevation and azimuth may be approximated to be equal so $\theta_{3db} = \phi_{3dB}$ (radians).

The resulting expression for the received power from a volume target is:

$$P_r = \frac{P_t A^2 n_A^2}{4\pi\lambda^2 r^4} V\eta \quad \textbf{(71)}$$

$$P_r = \frac{P_t A^2 n_A^2}{4\pi\lambda^2 r^4} \frac{r^2 c\tau\pi\theta_{3dB}^2}{16\ln 2}\eta \quad \textbf{(72)}$$

$$P_r = \frac{P_t A^2 n_A^2}{\lambda^2 r^2} \frac{c\tau\theta_{3dB}^2}{64\ln 2}\eta \quad \textbf{(73)}$$

since

$$\theta_{3db} \approx \sqrt{\sqrt{2}}\,\frac{\lambda}{D} = \sqrt{\sqrt{2}}\,\frac{\lambda}{\sqrt{A}}, \quad \textbf{(74)}$$

$$P_r = \frac{P_t A^2 n_A^2}{\lambda^2 r^2} \frac{c\tau\sqrt{2}\lambda^2}{64\ln 2A}\eta \quad \textbf{(75)}$$

$$P_r = \frac{P_t A n_A^2 c\tau\eta}{32 r^2} \quad \textbf{(76)}$$

This result shows that the radar received power from a volume target is a function of the power-aperture product, range squared, range resolution ($c\tau/2$) and volume reflectivity of the target. Volume reflectivity is dependent on frequency, polarization and beam pointing direction. This backscattering efficiency of small scatterers is dramatically higher (f^4) at higher frequency, as shown next. Note that the Signal to

Noise Ratio, SNR, usually increases as range resolution squared, because the noise power decreases with increasing pulse length (decreasing bandwidth) and thus range resolution.

The Volume reflectivity can be written as a sum of all the individual point scatterers in a unit volume:

(77) $$\eta = \sum_{i=1}^{N_v} \sigma_i .$$

If each scatterers can be approximated as a sphere, then the radar cross section can be estimated as the physical cross section $\frac{\pi D^2}{4}$ and an efficiency coefficient:

(78) $$\sigma = \frac{\xi \pi D^2}{4}$$

where ξ is the back scattering efficiency of a single scatterer and *D* is the diameter.

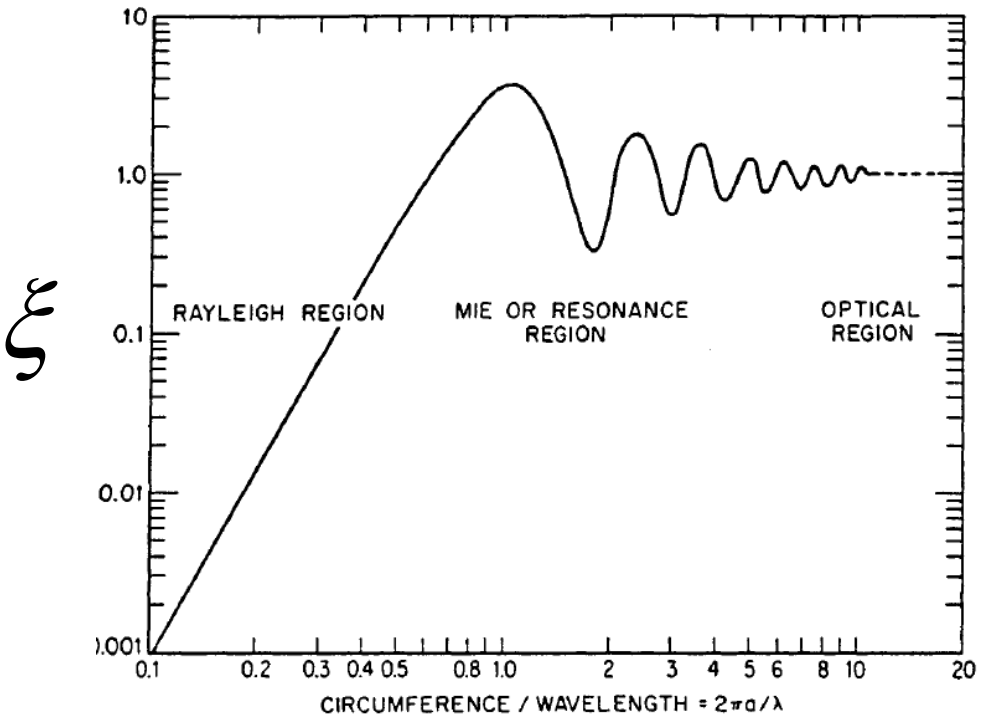

Figure 32. Radar backscattering efficiency (ξ) of a metal sphere as a function of radius (*a*) and radar wavelength (λ) (from: [3]).

In the Rayleigh region,

$$\xi \approx 4\left(\frac{\pi D}{\lambda}\right)^4 |K|^2 , \quad \textbf{(79)}$$

so

$$\sigma \approx \frac{\xi \pi D^2}{4} = \frac{\pi^5 D^6}{\lambda^4} |K|^2 , \quad \textbf{(80)}$$

where $K = \frac{n^2 - 1}{n^2 + 1}$, and n is the complex index of refraction.

at 9.4 GHz $|K|^2 \approx 0.97$; at 35 GHz $|K|^2 \approx 0.88$ and at 95 GHz $|K|^2 \approx 0.72$.

In the optical region, $\xi \approx 1$, so $\sigma \approx \frac{\pi D^2}{4}$, when $|n| >> 1$.

In the Rayleigh region:

$$P_r \propto \frac{P_t A \tau}{r^2 \lambda^4} \sum_{i=1}^{N_v} D_i^6 \quad \textbf{(81)}$$

In the Optical region:

$$P_r \propto \frac{P_t A \tau}{r^2} \sum_{i=1}^{N_v} D_i^2 \quad \textbf{(82)}$$

4.1.3 Attenuation

The attenuation (α) of liquid clouds and precipitation (liquid Rayleigh scatterers) is inversely proportional to wavelength squared and proportional to liquid volume **[24]**:

Liquid in the Rayleigh region:

$$\alpha \propto \frac{\sum_{i=1}^{N_v} D_i^3}{\lambda^{1.95}} \quad \textbf{(83)}$$

Attenuation of ice clouds is much lower and weaker related to wavelength:

Ice in the Rayleigh region:

$$\alpha \propto \frac{\sum_{i=1}^{N_v} D_i^3}{\lambda} \quad \textbf{(84)}$$

4.1.4 MRF Measurement Parameters

Ideally we would like to know the particle size distribution $f(D)$, but radar can only measure integrated parameters:

Reflectivity in the Rayleigh region: $\propto \int D^6 f(D)$ -> severely biased by the largest particles

Reflectivity in the Optical region: $\propto \int D^2 f(D)$ -> areal cross section

Attenuation in the Rayleigh region: $\propto \int D^3 f(D)$ -> liquid volume

Number density (N_V) is also an important physical parameter.

Let's assume a narrow size distribution such that

$$\eta = \sum_{i=1}^{N_v} \sigma_i = \frac{\pi^5}{\lambda^4} |K|^2 \sum_{i=1}^{N_v} D_i^6 \approx \frac{\pi^5}{\lambda^4} |K|^2 N_V D_e^6 \quad \textbf{(85)}$$

for Rayleigh scatterers,

and

$$\eta = \sum_{i=1}^{N_v} \sigma_i \approx \frac{\pi}{4} \sum_{i=1}^{N_v} D_i^2 = \frac{\pi}{4} N_V D_e^2 \quad \textbf{(86)}$$

for Optical scatterers.

where D_e is an *equivalent* particle diameter.

4.1.5 MFR Information Content

Two frequencies – both in Rayleigh and no differential attenuation (high altitude ice and ash with two radars):

$$P_{f1} \propto \frac{P_t A \tau}{r^2 \lambda_{f1}^4} N_V D_e^6 \quad \textbf{(87)}$$

$$P_{f2} \propto \frac{P_t A \tau}{r^2 \lambda_{f2}^4} N_V D_e^6 \quad \textbf{(88)}$$

Two linearly dependent equations, so there is no additional information by having two frequencies:

$$P_{f1} / P_{f2} \propto \frac{\lambda_{f2}^4}{\lambda_{f1}^4} \quad \rightarrow \quad \textbf{No New Information!} \quad \textbf{(89)}$$

Two frequencies – one Rayleigh, one Optical and no differential attenuation (high altitude ice and ash with radar and lidar sensor):

$$P_{f1} \propto \frac{P_t A \tau}{r^2 \lambda_{f1}^4} N_V D_e^6 \quad \textbf{(90)}$$

$$P_{f2} \propto \frac{P_t A \tau}{r^2} N_V D_e^2 \quad \textbf{(91)}$$

Two independent equations, two unknowns (D_e and N_V).

$$P_{f1} \Big/ P_{f2} \propto \frac{D_e^4}{\lambda_{f1}^4} \quad \textbf{(92)} \qquad \rightarrow \quad \textbf{Size Estimate}$$

From either power measurements, N_V can be also estimated. The above two cases (Rayleigh-Rayleigh without attenuation and Rayleigh-Optical) is well illustrated in Figure 41. The small, at both frequency (Rayleigh), cloud droplets form a flat line at 0 dB F-Zdr for the full range of LWC indicating that those radar measurements have no information content regarding LWC. On the other hand, the drizzle and rain points form an arcing line with high degree of correlation with liquid. Only scatterers in the Rayleigh to Optical transition, called Mie region would be difficult to measure.

Two frequencies – both in Rayleigh with differential attenuation (super-cooled liquid clouds and drizzle):

$$P_{f1} \propto \frac{P_t A \tau}{r^2 \lambda_{f1}^4} N_V D_e^6 \times \exp\left(-\alpha_{f1} \Delta r\right) \quad \textbf{(93)}$$

$$P_{f2} \propto \frac{P_t A \tau}{r^2 \lambda_{f2}^4} N_V D_e^6 \times \exp\left(-\alpha_{f2} \Delta r\right) \quad \textbf{(94)}$$

$$P_{f1} \Big/ P_{f2} \propto \frac{\lambda_{f2}^4}{\lambda_{f1}^4} \exp\left(\left(\alpha_{f2} - \alpha_{f1}\right) \Delta r\right) \quad \textbf{(95)}$$

$$\left(\alpha_{f2} - \alpha_{f1}\right) \propto N_V D_e^3 \left(\frac{1}{\lambda_{f2}^2} - \frac{1}{\lambda_{f1}^2} \right) \quad \textbf{(96)} \qquad \rightarrow \textbf{Liquid Water Content Information}$$

From either power measurement, N_V and D_e can also be estimated.

In practice, retrievals are more complicated because the drop size distributions can be broad, so

reflectivity measurements are dominated by larger particles than attenuation in the Rayleigh region. Also higher frequency radars will often operate in the Mie region (Rayleigh to Optical transition), where resonant scattering varies the backscattering efficiency rapidly as a function of D/λ. Nevertheless, even with wider drop size distribution, an approximate measure of drop size and number density can be estimated and used to improve hazard detection and characterization. Clearly, there is potential for additional information from dual frequency radar when the differential attenuation rate is sufficient to decouple the measurements. The logical next questions are: how much frequency separation is needed; and what is the overlapping detection range (sensitivity) of various frequency combinations, based on currently available radar components? These questions are addressed next.

MFR Components – Current Technology

4.1.6 Antennas

Airborne weather radar antennas are almost exclusively flat plate slotted arrays as shown in Figure 33. These antennas combine exceptional mechanical and electrical properties. Their light weight and narrow profile make them ideal for airborne use, the waveguide construction minimizes loss and thus improves efficiency and the absence of feed blockage leads to very low sidelobes and high beam efficiency. In size they range from 12" on the smaller commuter aircrafts to 20" and 30" in diameter on the mid- to larger aircrafts. This antenna type has been manufactured up to Ka-band frequency, but only available in single polarization. Dual-polarized microstrip arrays have been designed but their limited power handling capability makes them less attractive with weather radars.

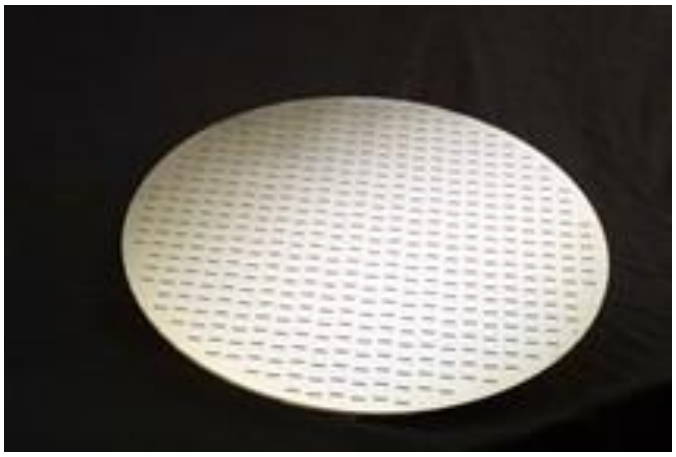

Figure 33. X-band flat plate slotted antenna array.

For the following multi-frequency radar simulations we will consider the 20" diameter antenna at the frequencies shown in Table 1.

Table 3. Approximate antenna half-power beamwidth and gain as a function of antenna diameter and frequency. Further analysis of this report will consider the optimistic 20" diameter antenna size for all frequencies.

Diameter	X	Ku	Ka	W
12"	7.5° (27 dB)	4.7° (31 dB)	2.0° (38 dB)	0.75° (47 dB)
20"	4.5° (31 dB)	2.8° (35 dB)	1.2° (43 dB)	0.44° (51 dB)
30"	3.0° (35 dB)	1.9° (38 dB)	0.8° (46 dB)	0.30° (55 dB)

4.1.7 Transmitters

Airborne weather radars primarily use magnetron power sources for their small size, high peak power. X-band magnetrons in the 10-25 kW peak power range have been manufactured in high volume for marine ship detection and airborne weather radar applications, resulting in per unit cost below $1000 – by far the least expensive high power source per unit output power. Figure **34** illustrates the peak power of various power sources as a function of frequency. Magnetrons are vacuum devices, available up to Ka-band at peak power ranging from about a 1kW to hundreds of kW, and 0.1% maximum duty. Other, usually higher average power vacuum tubes include Klystrons, Gyrotrons and Traveling Wave Tube amplifiers, but these typically require much larger modulators and power supplies, making them less attractive for airborne use. High duty solid state devices and microwave modules are sufficiently compact for airborne use and over the past decade have become available with average power comparable or exceeding that of magnetrons, but their peak power is low, and it is difficult to utilize more than 5% duty cycle with a single antenna radar system. Table 4 through Table 7 lists the various currently available transmit sources at various frequencies. For the sensitivity calculation 10 kW peak power was assumed at X, Ku and Ka bands and the optimistic (due to cost, size and weight) 1 kW Klystron peak power at W-band.

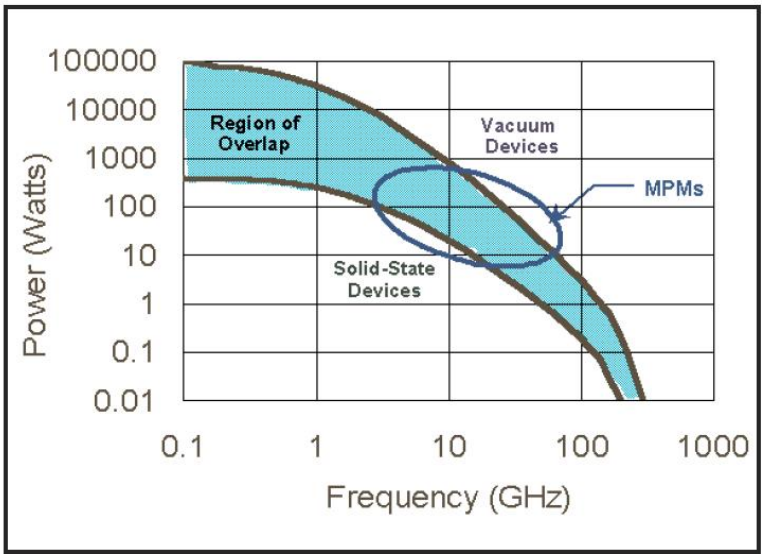

Figure 34**. Transmitter power versus frequency (from the Litton-L3 MPM web site).**

Table 4. X-band transmitters (8 – 12 GHz).

Type	Peak	Duty	Practical		Cost ($K)
			Peak	Average	
Magnetron	10-1000 kW	0.1%	10-20 kW	10-20 W	1
TWTA	0.1-150 kW	CW – 6%	-	-	100+
Klystron	0.5 – 3 kW	CW – 5%	-	-	100+
MPM	10-100 W	5% - CW	100 W	10 W	10
Solid State PA	20 W	5%-CW	20 W	2 W	10
Solid State Array (20x20)	0.1 W/element	5%-CW	40 W	4 W	10

Table 5. Ku-band transmitters (12 – 18 GHz).

Type	Peak	Duty	Practical		Cost ($K)
			Peak	Average	
Magnetron	10-1000 kW	0.1%	10-20 kW	10-20 W	1
TWTA	0.1-60 kW	0.1 – 30%	-	-	100+
Klystron	0.5 – 3 kW	5% - CW	-	-	100+
MPM	10-100 W	5% - CW	100 W	10 W	10
Solid State PA	20 W	5% - CW	20 W	2 W	10
Solid State Array (20x20)	0.1 W/element	5% - CW	40 W	4 W	10

Table 6. Ka-band transmitters (27 – 40 GHz).

Type	Peak	Duty	Practical		Cost ($K)
			Peak	Average	
Magnetron	10-100 kW	0.1%	20 kW	20 W	50
TWTA	0.1-60 kW	0.1 – 30%	-	-	100+
Klystron	2 kW	5%	2 kW	100 W	100+
MPM	10-100 W	5% - CW	100 W	10 W	10
Solid State PA	20 W	5% - CW	20 W	2 W	10
Solid State Array (20x20)	-	-	-	-	-

Table 7. W-band transmitters (75 – 110 GHz).

Type	Peak	Duty	Practical		Cost ($K)
			Peak	Average	
Magnetron	-	-	-	-	-
TWTA	0.05 - 3 kW	10 % – CW	-	-	100+
Klystron	1 kW	5% - CW	1 kW	50	100+
MPM	10-100 W	5% - CW	100 W	10 W	10
Solid State PA	20 W	5% - CW	20 W	2 W	10
Solid State Array (20x20)	0.1 W/element	5% - CW	40 W	4 W	10

MFR Detection

A cloud and precipitation model was used to predict detection (unity single pulse signal to noise ratio) using the following assumed radar specifications:

Table 8. List of radar parameters used in the sensitivity calculations.

	X	Ku	Ka	W
Peak Power (kW)	10	10	10	1
TX Loss (dB)	0.25	0.3	0.5	1
Antenna Gain (dB)	31	35	43	51
RX NF (dB)	1	1.5	3	6
RX Bandwidth (MHz)	2	2	2	1
RF Parts Cost (2013)	10k	?	100k	300k

Transmitted peak power: 10 kW at X, Ku, Ka and 1 kW at W-band.

Transmitter Loss: 0.25, 0.3, 0.5 dB and 1 dB at X, Ku, Ka and W-band respectively

Receiver Noise Figure: 1.0, 1.5, 3.0 and 6 dB at X, Ku, Ka and W-band respectively

Range Resolution: 150 m (1 MHz pulse bandwidth)

Receiver bandwidth: 2 MHz with X, Ku and Ka (twice the pulse bandwidth with magnetron radars); 1 MHz with W-band Klystron transmitter.

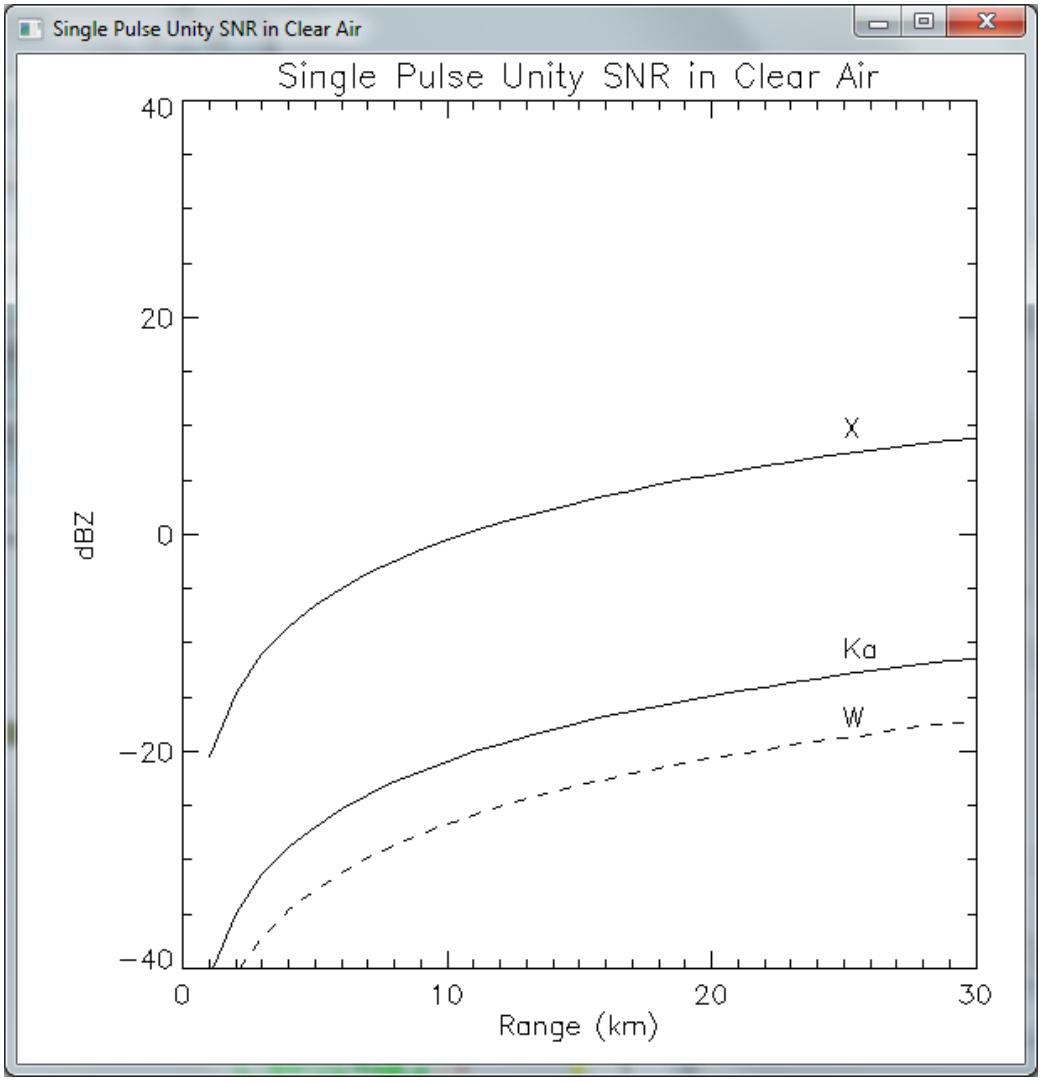

Figure 35. Single pulse, unity Signal to Noise Ratio (SNR) in clear air with 20" diameter antennas.

4.1.8 Cloud and Precipitation Model

In this section a cloud and precipitation model is presented for the evaluation the measurement range and sensitivity of various radars considered in 4.1.7. The model consists of groups of three types of size distribution: 1) Clouds using the Modified Gamma distribution model, 2) Drizzle using a modified Marshal-Palmer distribution model and 3) Rain using the Marshall-Palmer distribution [pp. 306 – 317, Ulaby et. al, 1984: Microwave Remote Sensing].

Cloud model - Modified Gamma drop size distribution:

The number of drop per cubic meter per drop radius unit interval

$$p(r) = ar^{\alpha} \exp\left(-br^{\gamma}\right) \tag{97}$$

where

r = drop radius, m,

α and γ are shape parameters,

b is a constant related to the mode radius, r_c in units of m,

$$b = \frac{\alpha}{r_c^{\gamma}\gamma} \quad \textbf{(98)}$$

and a is a function of the liquid water content, m_v, according to

$$a = \frac{3m_v\gamma b^{\beta_2}}{4\times10^6\pi\Gamma(\beta_2)} \quad \textbf{(99)};$$

$$\beta_2 = \frac{\alpha+4}{\gamma} \quad \textbf{(100)}$$

and $\Gamma(\ )$ is the Gamma function.

For this simulation the parameters were varied:

$5 \le \alpha \le 7$, $0.3 \le \gamma \le 2$, and $0.1 \le m_v \le 2$ gm^{-3}.

Drizzle and Rain model:

The number of drop per cubic meter per unit radius interval

$$p(d) = N_\circ \exp(-bd) \quad \textbf{(101)}$$

where

d is drop diameter in units of meters,

$N_\circ = 30\times10^6$ m^{-4}, $b = 5700R_r^{-0.21}$ for drizzle,

$N_\circ = 8\times10^6$ m^{-4}, $b = 4100R_r^{-0.21}$ for rain,

and rain rate, R_r was varied from 0.1 to 5 mm/hr for drizzle and 0.1 to 150 mm/hr for rain. The resulting range in Liquid Water Content as a function of rain rate is illustrated in Figure 36.

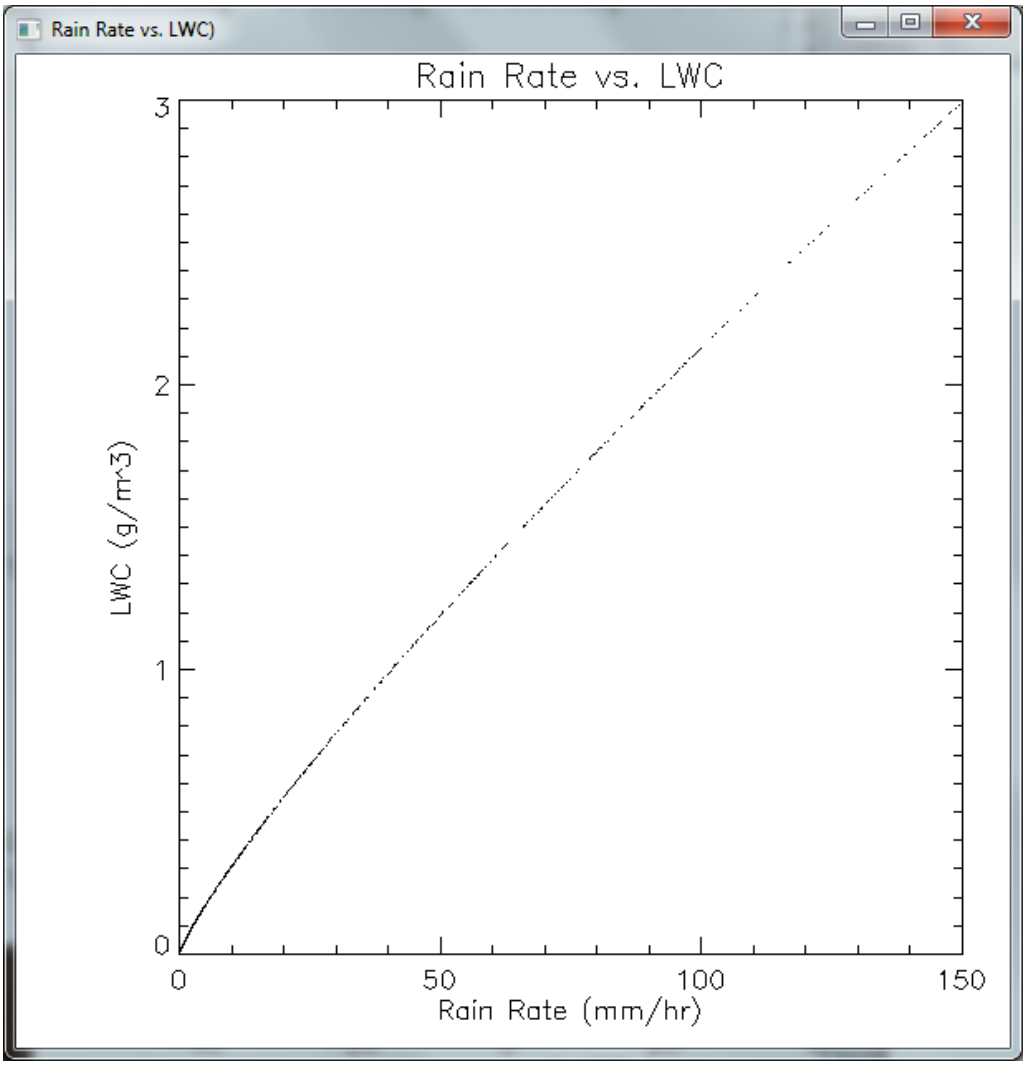

Figure 36. Drizzle and Rain data distribution of Rain-Rate vs. Liquid water Content.

A data base of drop size distributions was generated using the three models for cloud, drizzle and rain. This simulated data set was then used to estimate the measurement range and sensitivity of various radar configurations. The distribution of mean diameter and the sixth moment (mean Z diameter) of the distributions is shown in Figure 37. The deviation of the scatter plot from the straight x=y line is an indication of the spread of the drop size distribution and how the radar reflectivity is dominated by the largest drops in a volume cell. The data set distribution of radar reflectivity vs. attenuation at C, X and Ka-band is shown in Figure 38, Figure 39 and Figure 40.

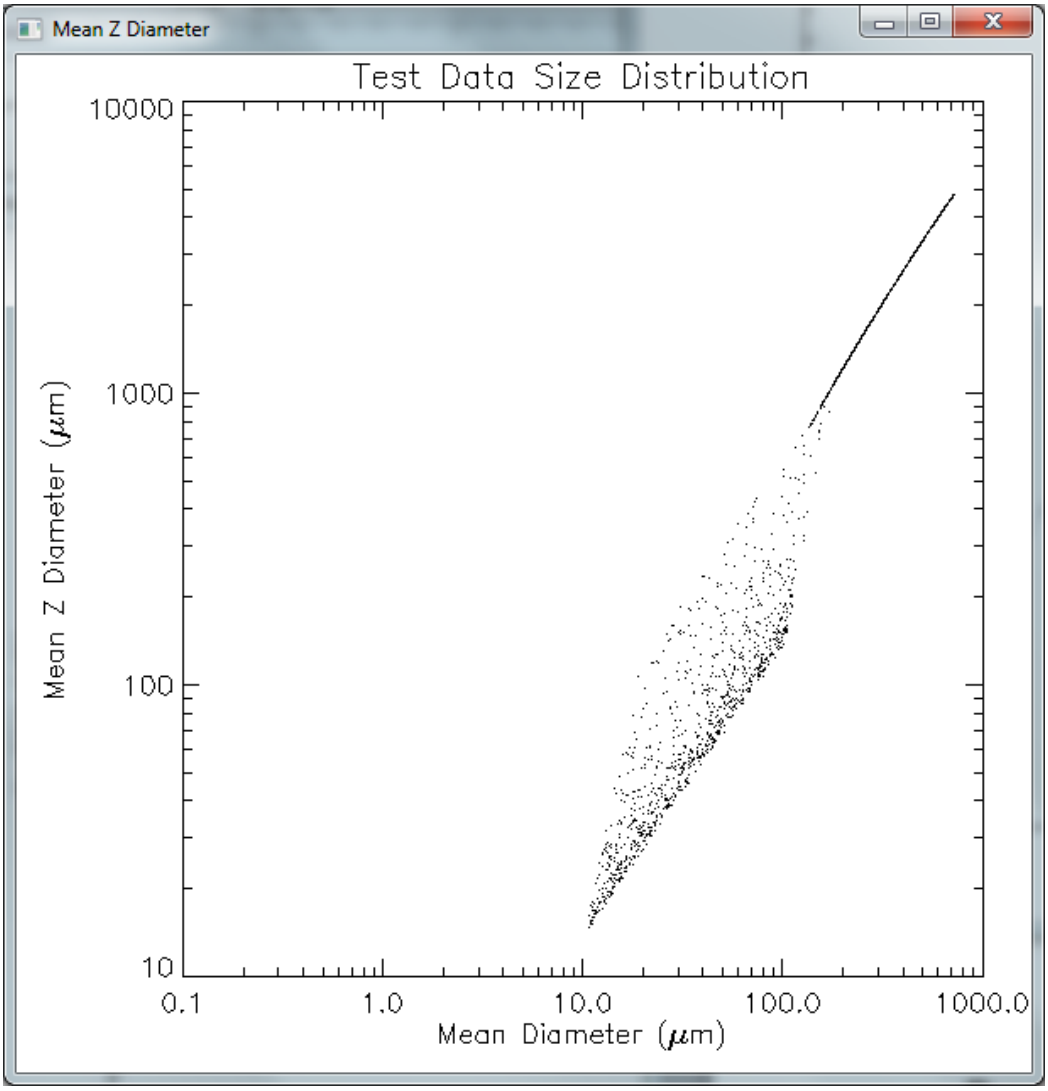

Figure 37. Combined Cloud, Drizzle and Rain data distribution of Mean Z diameter vs. Mean Diamater – an indication of the dominant drop diameter of radar reflectivity factor.

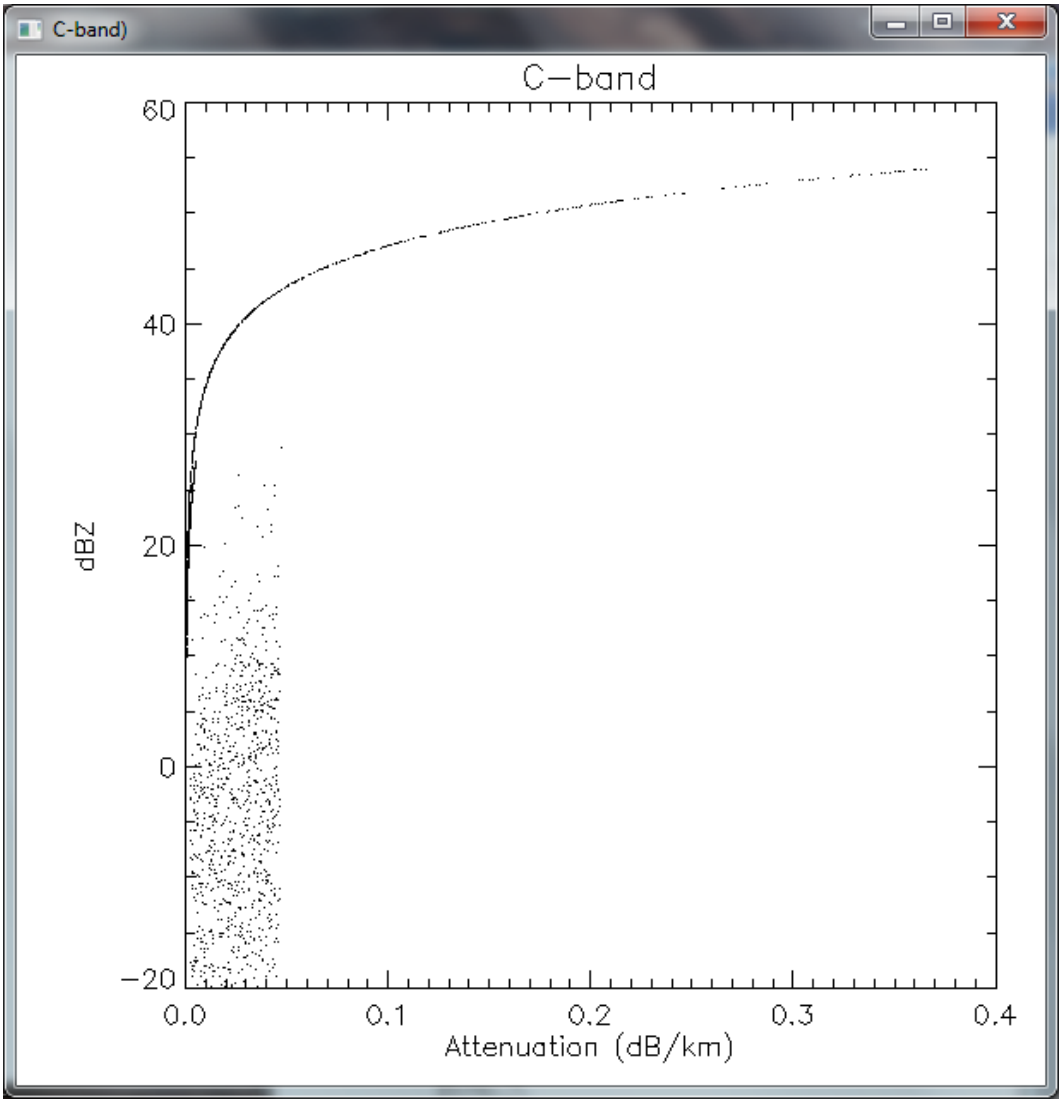

Figure 38. Combined Cloud, Drizzle and Rain data distribution of radar reflectivity factor, Z, vs. Attenuation at C-band (5 GHz).

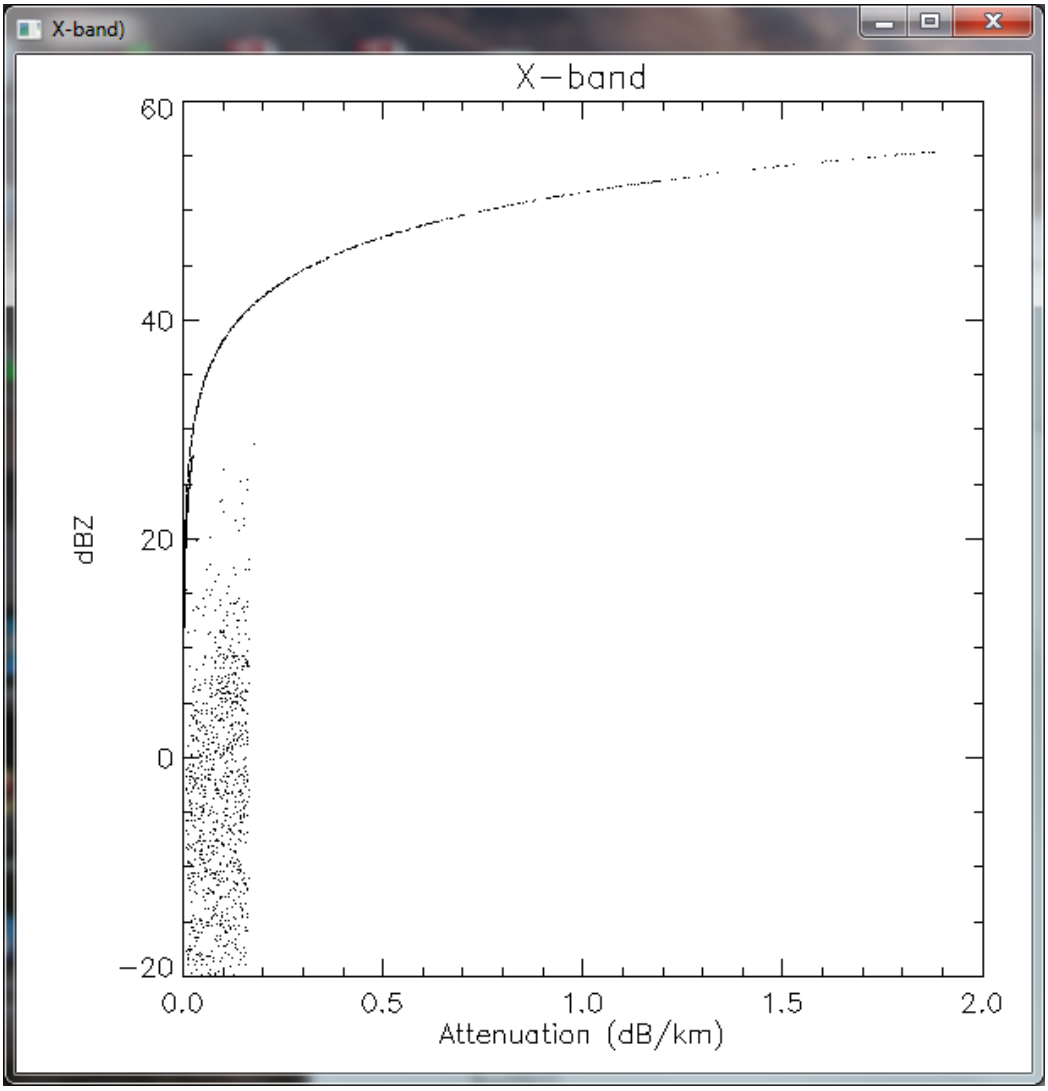

Figure 39. Combined Cloud, Drizzle and Rain data distribution of radar reflectivity factor, Z, vs. Attenuation at X-band (9.4 GHz).

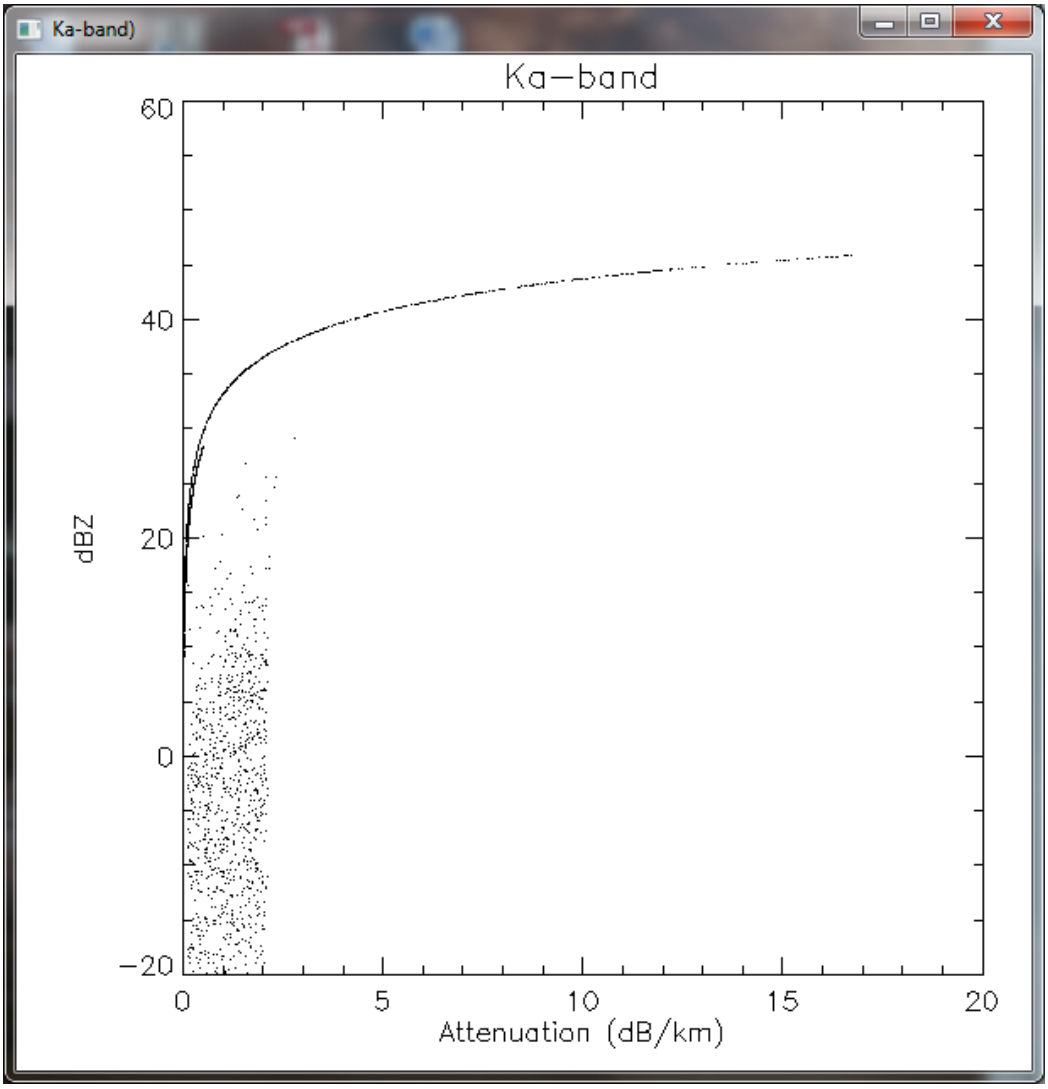

Figure 40. Combined Cloud, Drizzle and Rain data distribution of radar reflectivity factor, Z, vs. Attenuation at Ka-band (35 GHz).

The potential information content of differential frequency reflectivity measurements is illustrated in Figure 41. The cloud particles are Rayleigh scatterers at both frequencies so their differential reflectivity factor is 0 dB, irregardless of LWC – forming a line at 0 dB and indicating that LWC cannot be estimated; as was predicted in Equation (89. In the Mie (Rayleigh to Optical transition) region at Ka-band, resonnance can actually increase the radar reflectivity factor at Ka band compared to that at C-band (negative F-Zdr), but LWC (and/or drop size) estimation is still difficult because the same differential reflectivity can indicate multiple solutions to LWC. But when the higher frequency is in the optical region (the arc of points from [0 g/m^3, -0.75 dB] to [3 g/m^3, 8 dB]), LWC can be easily estimated, confirming (92.

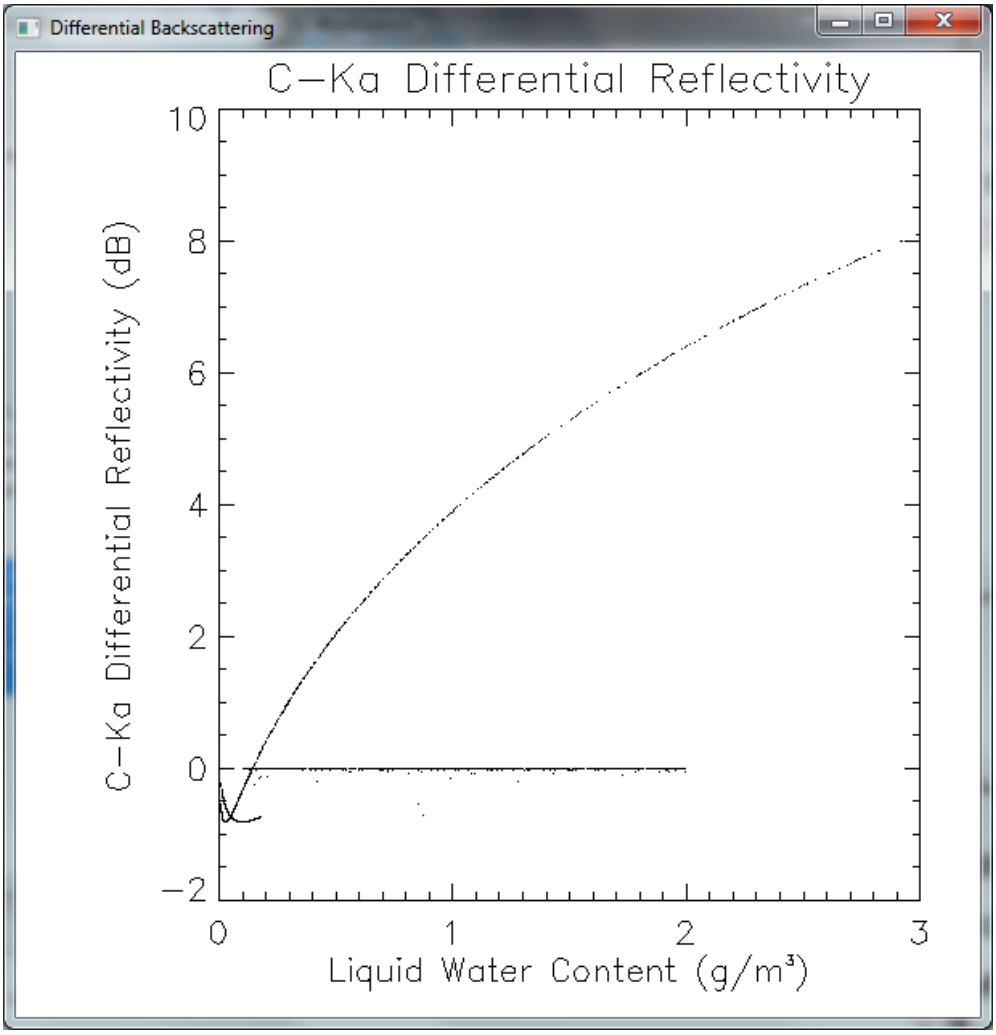

Figure 41. Combined Cloud, Drizzle and Rain data distribution of frequency differential reflectivity factor, F-Zdr, vs. Liquid Water Content (g/m^3).

4.1.9 Detection to 10 and 20 km Range

In this section, detection of the various simulated cloud, drizzle and rain cases are determined for the radar configurations (frequencies and system parameters) tabulated in Table 8 and assuming a 150 m range resolution. The attenuation rate and reflectivity was calculated for each cloud, drizzle and raindrop size distribution. Then the radar received signal to noise ratio was calculated for each simulated weather condition, considering reflectivity and the two-way attenuated propagation to 10 km and 20 km (the weather condition, and the corresponding attenuation rate, was assumed to be uniform over the two-way propagation distance). Detection was assumed for unity or greater signal to noise ratio. This detection threshold is reasonable because averaging was not accounted for, which reduces the false alarm rate. Undetected weather events (simulated data base points) are indicated by small black points through Figure 42 to Figure 44.

Multi-frequency detection to 10 km range is shown in Figure 42 and Figure 43, and to 20 km in Figure 44. The scatter plots clearly show that the lower frequency radars are best suited for the heavier precipitation, while the higher frequency millimeter wave systems have better sensitivity at short ranges. But even from a range of 10 km, attenuation severely diminishes detection at Ka and W-bands. As expected, X-band is the best compromise between sensitivity to small scatterers and attenuation, but C-band is the only of the tested frequencies that can penetrate the heaviest precipitation cases.

The results indicate that detection of the most hazardous conditions like high LWC cloud and severe rain is not reliable at multiple frequencies. The combination of C and X bands (red and orange points in Figure 42 and Figure 44) is effective in most drizzle and weak to moderate rain events, but C-band lacks sensitivity in most clouds and small particle drizzle and X-band attenuation is too strong in the heavier rain cases. The X and Ka combination (red and purple points in Figure 42 and Figure 44) can detect more cloud cases and the weaker drizzle, but ineffective in anything stronger than moderate rain. Also, from a range of 20 km, the attenuation at Ka-band severely reduces the number of detected cases.

A better reason for multi-frequency is the option to switch to a lower frequency channel when attenuation at X-band prevents detection. This improvement in sensitivity at lower frequency in highly attenuation conditions is well illustrated in Figure 45, Figure 46 and Figure 47. C-band can detect all but the weakest drizzle and rain conditions to 20 km but very few of the clouds. X-band detects more of the clouds and just about all the drizzle but is unable to penetrate heavier rain. Attenuation at Ka-band severely limits detection to just a few low LWC cases.

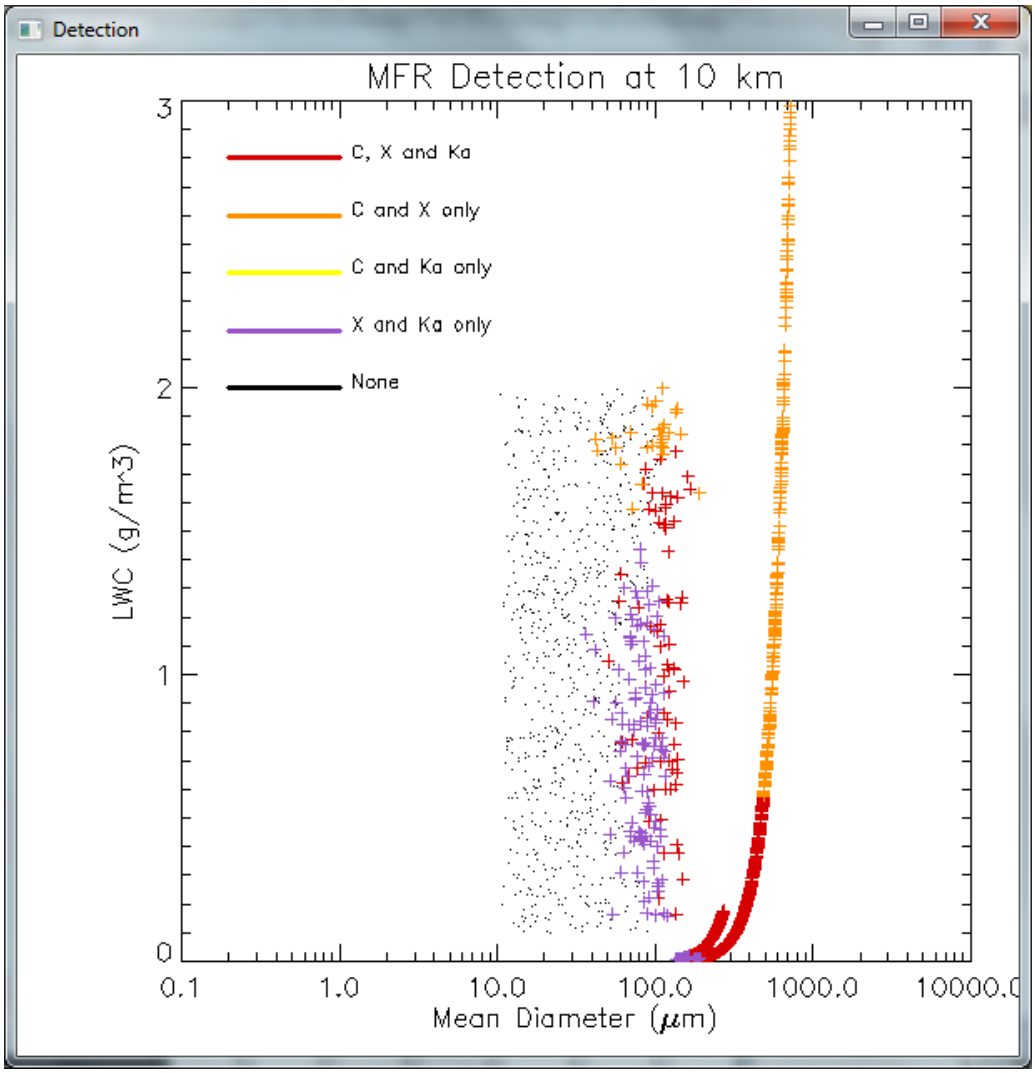

Figure 42. C, X, and Ka-band simultaneous, multi-frequency detection to 10 km range.

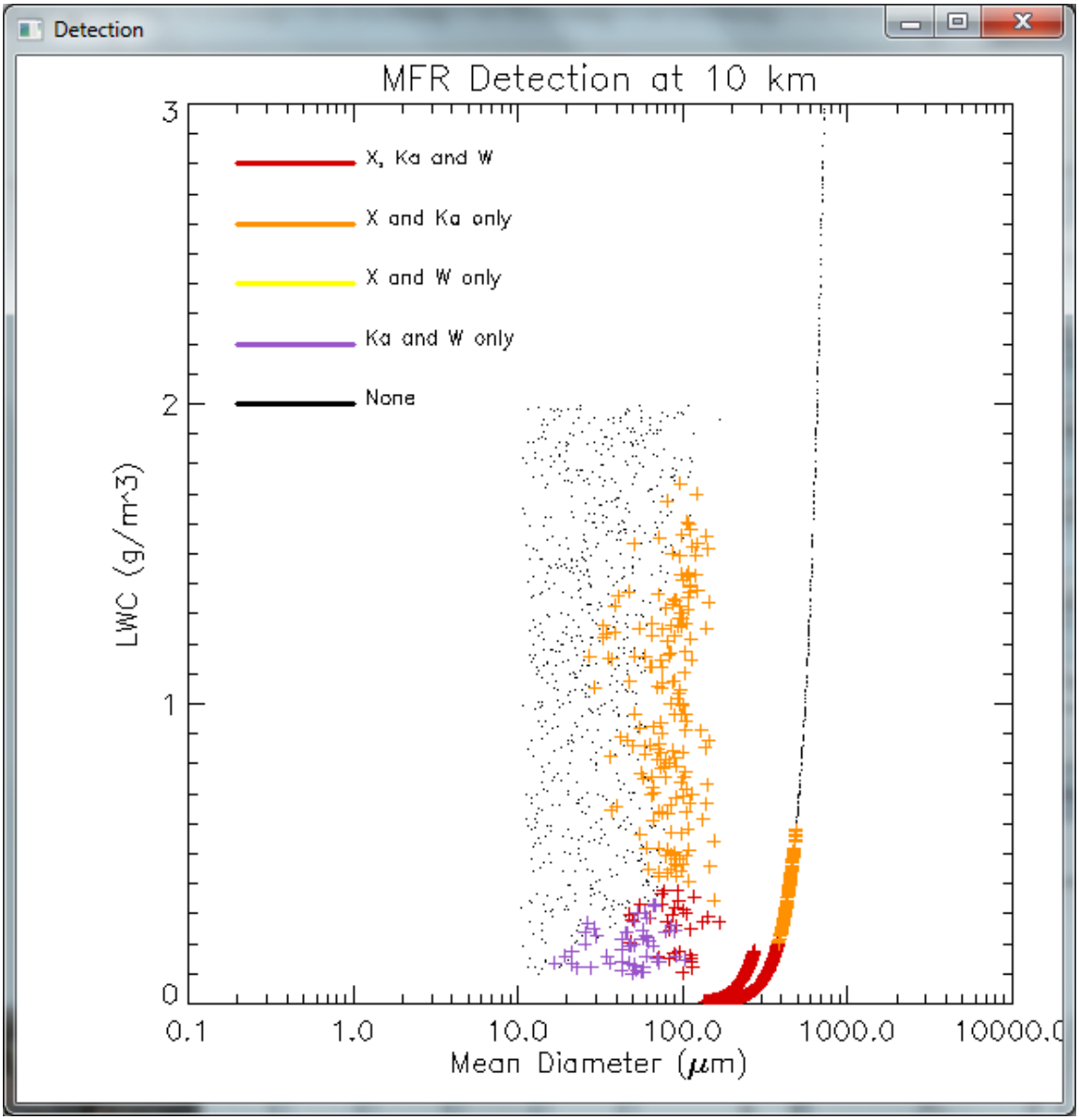

Figure 43. Simultaneous MFR detection to 20 km range at X, Ka, and W-bands.

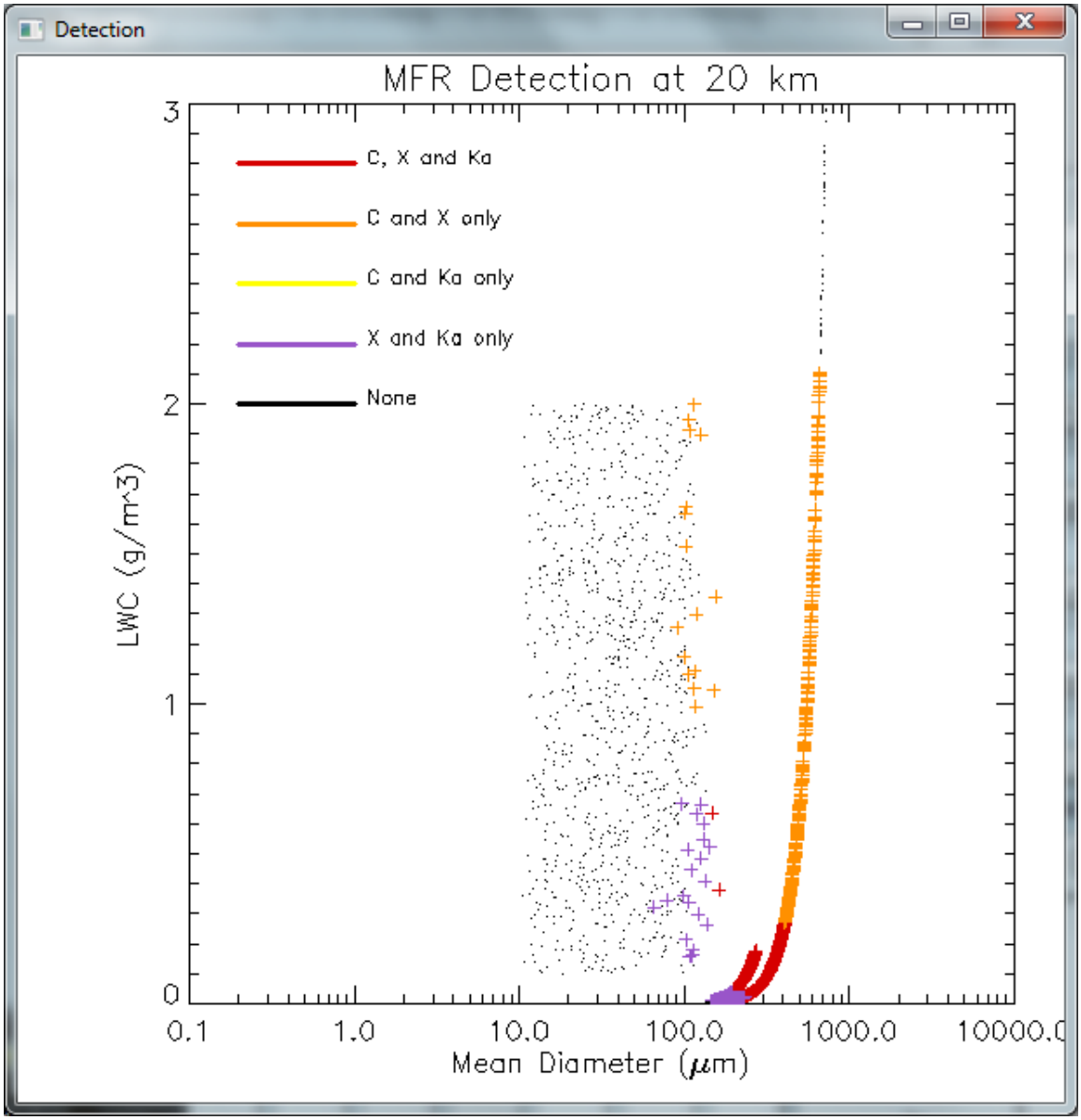

Figure 44. Simultaneous MFR detection at C, X and Ka-bands, to 20 km.

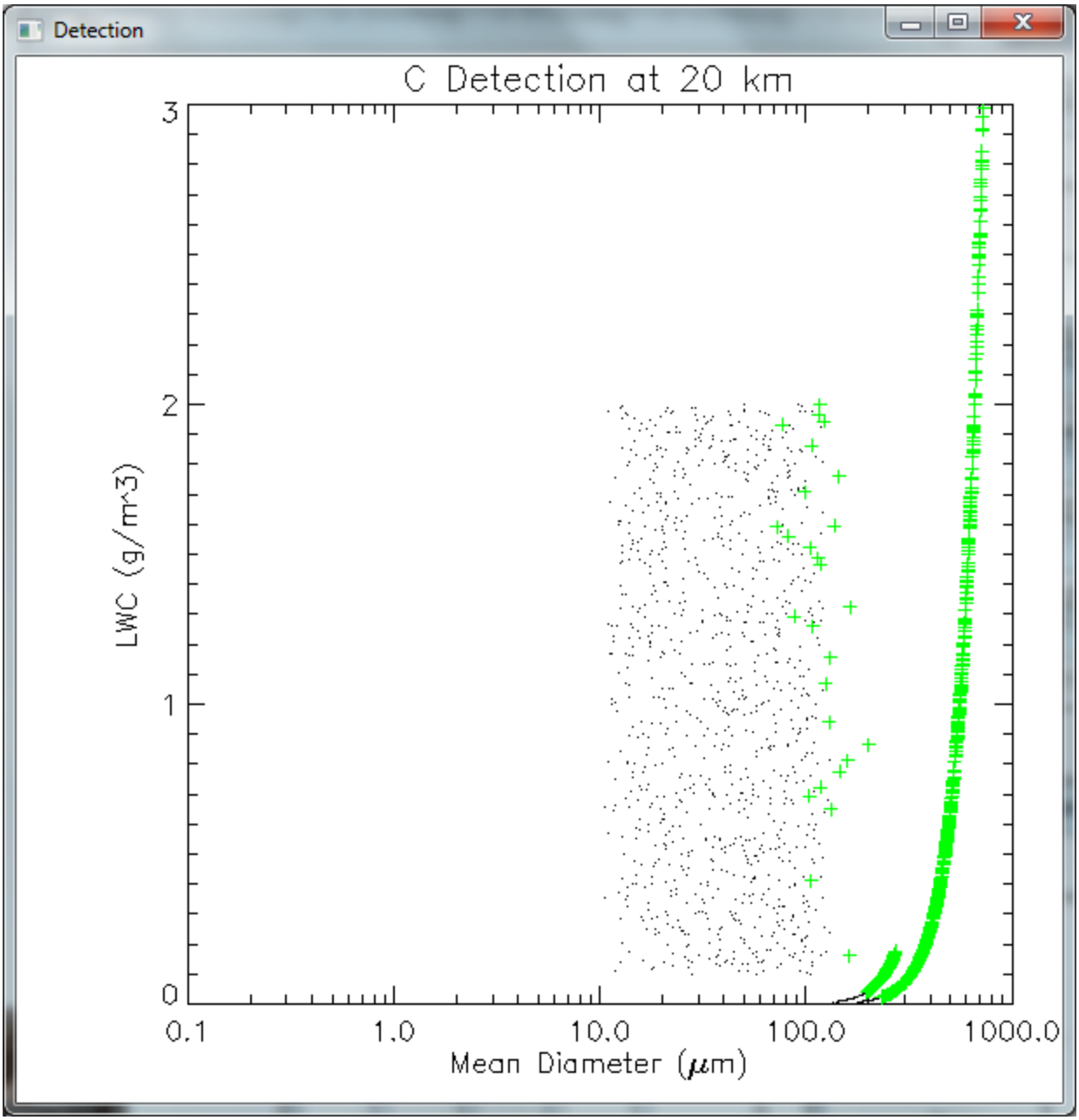

Figure 45. C-band detection to 20 km range.

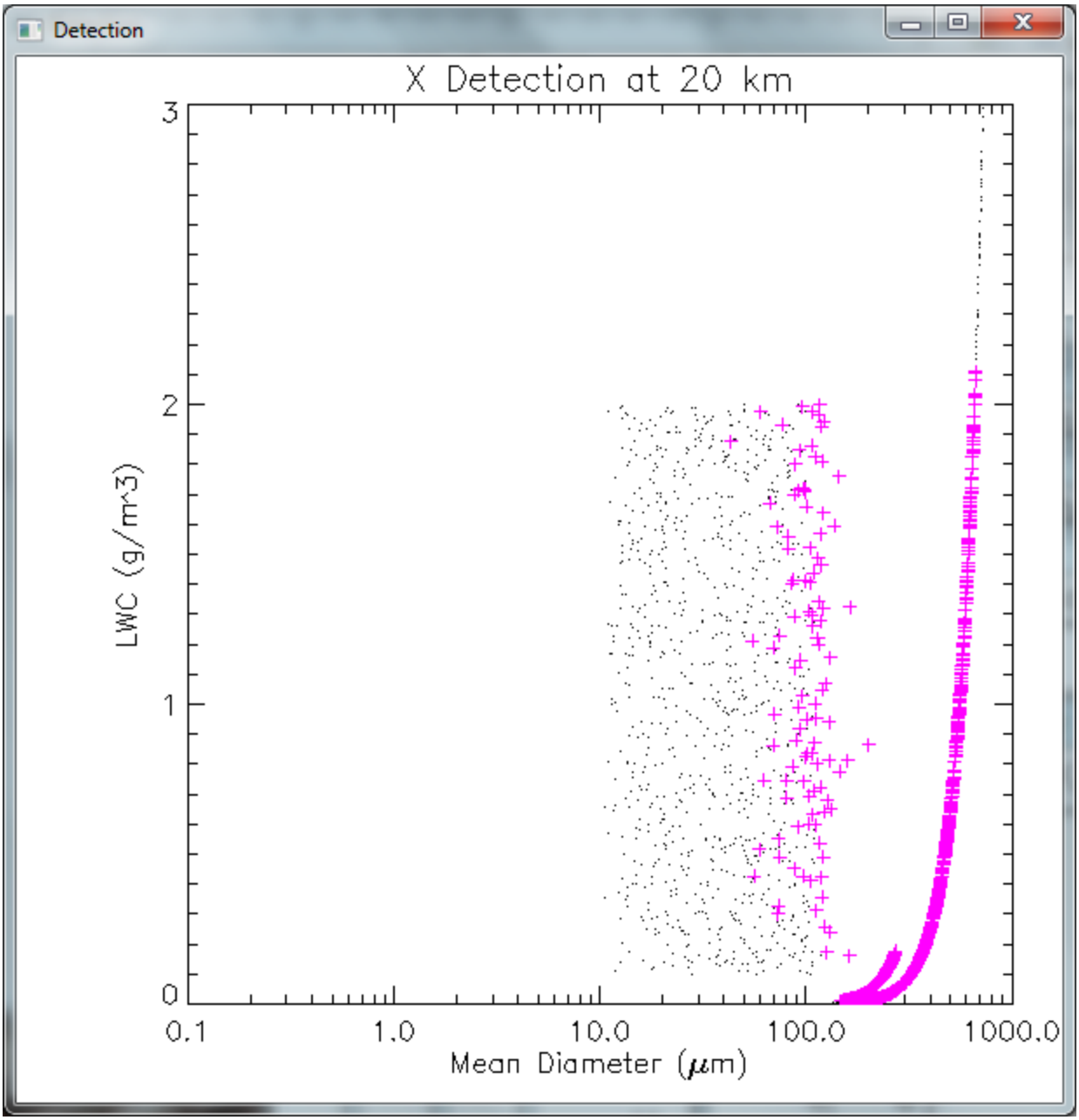

Figure 46. X-band detection to 20 km range.

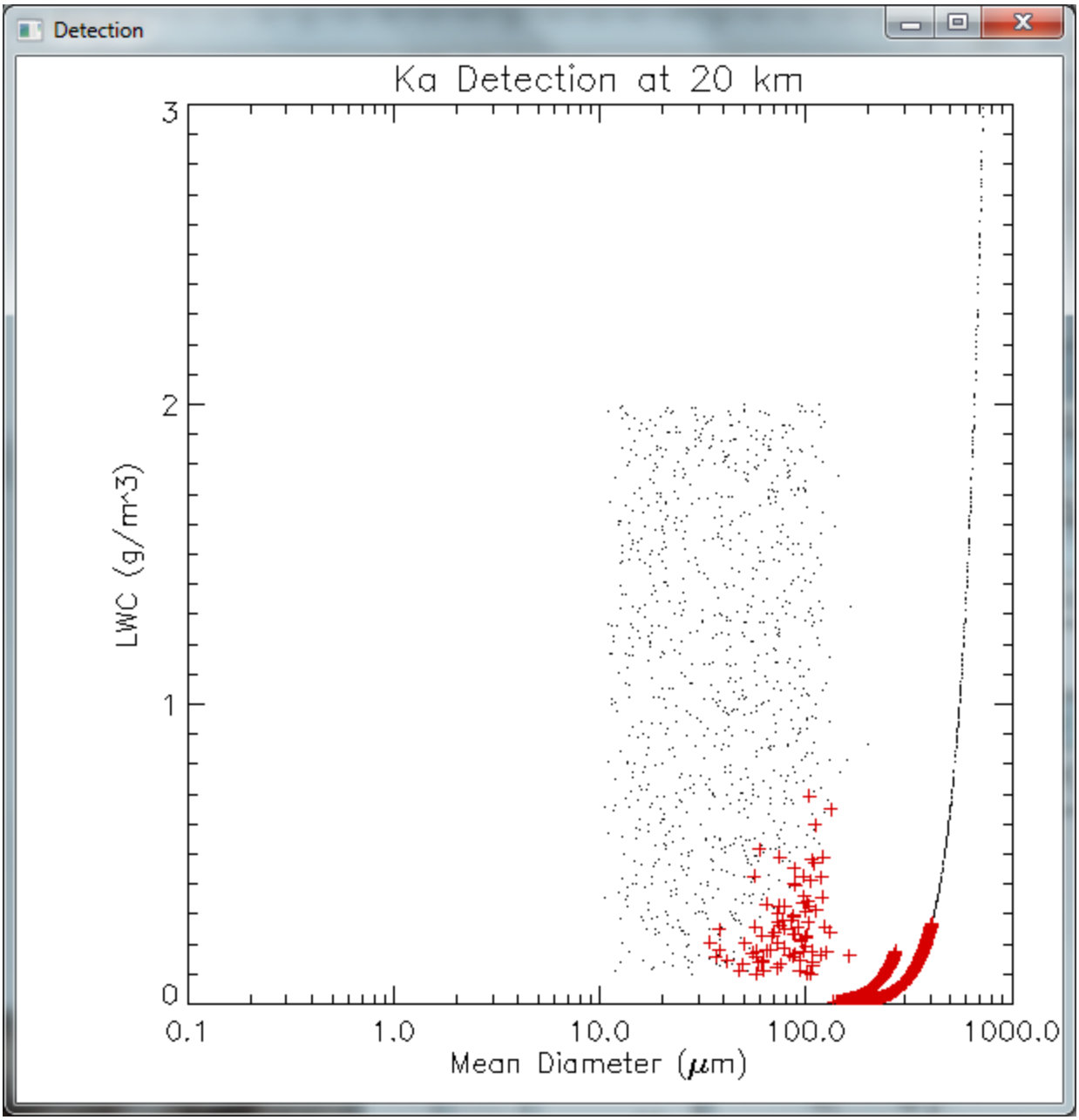

Figure 47. Ka-band detection to 20 km range.

MFR Differential Attenuation

In severe weather conditions X-band attenuation can be quite high, resulting in underestimating dangerous weather cores, but worse: can lead to the received signal diminishing below the detectable threshold. So by shifting to a lower frequency, attenuation quickly decreases. The attenuation rate (dB km^{-1} mm^{-1} hr) in rain as a function of radar frequency is illustrated in Figure 48. Attenuation is approximately proportional to f^2, so a small change in operating frequency, that is available within a

waveguide band, yields very small change in attenuation rate and thus is not worth the added cost and system complexity. However, if a C-band channel was available in heavy (50 mm/hr) precipitation, the attenuation rate decreases from 1.5 dB/km at X-band to 0.3 dB/km. Over a 10 km wide precipitation (20 km two way propagation) this adds up to a 24 dB difference in total attenuation, and approximately a 12 dB improvement in sensitivity; assuming similar radar power-aperture product. *So when X-band attenuation is so severe that attenuation correction techniques, such as polarimetric or radiometric, cannot be employed, C-band radar might still penetrate heavy precipitation and detect and identify hazardous weather cores.*

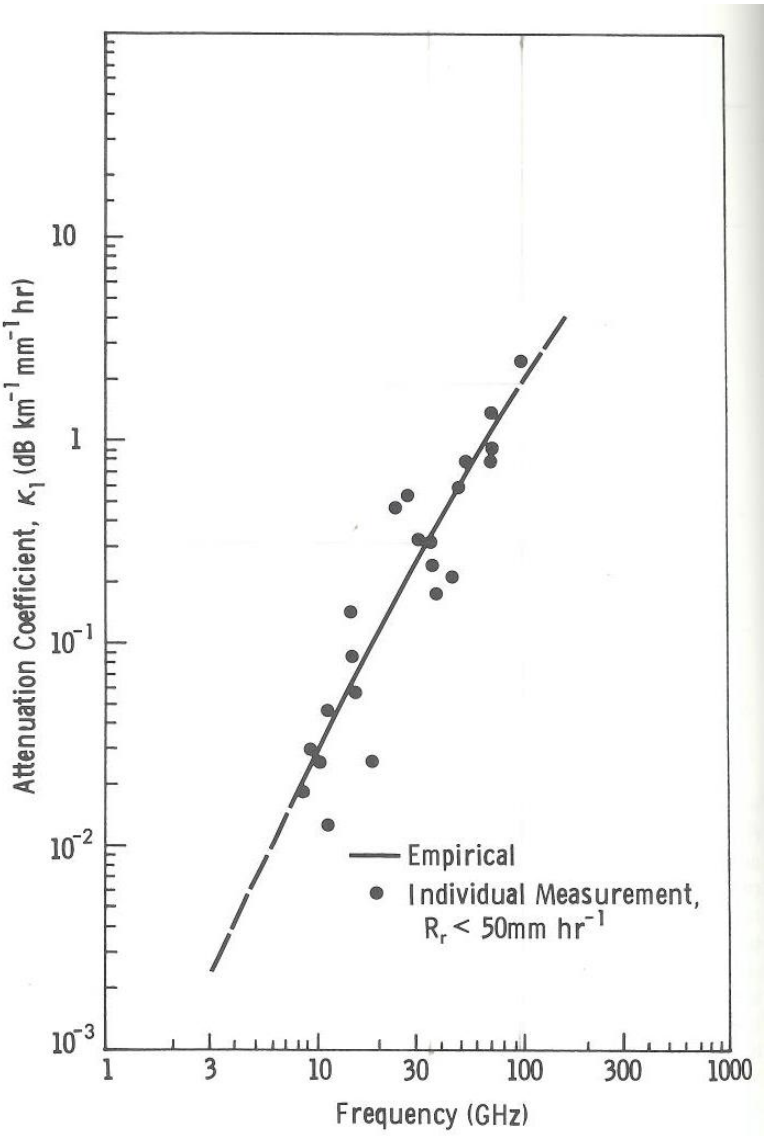

Figure 48. Attenuation rate per rain rate as a function of radar frequency (from [3]).

There is a potential benefit in adding a second, higher frequency. The backscattering efficiency of small (Rayleigh) hydrometeors increases as f^4, so for example a Ka-band (33 GHz –> 3.5 times that of a 9.4 GHz X-band) radar, given the same radar power-aperture product, receiver sensitivity and attenuation,

will have almost 22 dB more sensitivity. The problem however is attenuation. Attenuation can easily overcome this gain. The attenuation rate at X-band is approximately 0.006 dB km^{-1} mm^{-1} hr while at Ka-band is 0.3 dB km^{-1} mm^{-1} hr. So even a 10 mm/hr rain will cancel the backscattering sensitivity gain over a short, two-way propagation distance of 7.5 km (3.75 km range)! Shifting from X-band to Ka-band only makes sense when attenuation is low; i.e. for the detection and mapping of freezing drizzle/light-rain or high altitude ice clouds.

For the same reason, dual-frequency X-Ka band measurements also have limited use. Although the differential attenuation rate is sufficiently high for easy detection and estimation of rain rate and attenuation, as shown in Figure 52, in those highly attenuating conditions, dual-frequency measurement range is severely limited as confirmed by the results shown in Figure 42, Figure 46 and Figure 47.

The following calculation finds the measurement accuracy that is necessary for useful dual-frequency measurements:

$$P_m = P_s + P_n \tag{102}$$

$$\sigma_m = \frac{P_s + P_n}{\sqrt{N}} \quad ; \tag{103}$$

and

$$\sigma_n = \frac{P_n}{\sqrt{N_n}} \tag{104}$$

$$\frac{\sigma_s}{P_s} = \sqrt{\frac{\left(1+\frac{1}{SNR}\right)^2}{N} + \frac{\left(\frac{1}{SNR}\right)^2}{N_n}} \tag{105}$$

The standard error deviation E_σ of a reflectivity measurement in units of dB can be expressed as

$$dBE_\sigma = 10\log_{10}\left(\frac{P_s \pm \sigma_s}{P_s}\right) = 10\log_{10}\left(1 \pm \sqrt{\frac{\left(1+\frac{1}{SNR}\right)^2}{N} + \frac{\left(\frac{1}{SNR}\right)^2}{N_n}}\right). \tag{106}$$

In high *SNR* this expression simplifies to

$$dBE_\sigma = 10\log_{10}\left(1 \pm \frac{1}{\sqrt{N}}\right). \tag{107}$$

The estimation of differential attenuation (ΔA) requires four reflectivity measurements:

$$\Delta A(f_1, f_2) = \frac{\left(dBZ_{f_2}(r_2) - dBZ_{f_2}(r_1)\right) - \left(dBZ_{f_1}(r_2) - dBZ_{f_1}(r_1)\right)}{r_2 - r_1} \quad \textbf{(108)}$$

Consequently, the expected error in the measured differential attenuation, $dBE_{\Delta A}$, in high signal to noise ratio conditions can be expressed as

$$dBE_{\Delta A} = \frac{\sqrt{4} \times dBE_{\Delta A}}{\Delta r} \quad \textbf{(109)}$$

.

If we are satisfied with a 1 km range resolution and a 1 dB/km differential attenuation as a practical goal, then the measurement standard deviation should be no more than 0.5 dB. To achieve this accuracy, the required number of independent samples is

$$0.5 = 10\log_{10}\left(1 \pm \frac{1}{\sqrt{N}}\right) \rightarrow N \approx 67 \quad \textbf{(110)}$$

Note that the resulting measurement quality is still poor since the 0.5 dB error corresponds to a single σ deviation, yielding only a 68% of the measurements within 0.5 dB of the actual differential attenuation, as shown in Figure 49. To increase the confidence interval to 95%, 287 samples are required. Another way to look at this is that if the differential attenuation is 1 dB, then our measurements should have much smaller than 1 dB standard deviation. If 287 samples are averaged, then the resulting differential attenuation measurement standard error (deviation) will be approximately ±0.25 dB. But if ~300 independent samples are required for a single differential attenuation measurement, then a complete volume scan ahead of an aircraft would take a long time.

If an AWR has a PRF of 5 kHz (30 km maximum range), then approximately 17 (5000/300) measurements can be made in a second, so a 100 point volume scan would take about 6 seconds. But this calculation assumes that all the samples are independent at all the frequencies. At X-band the approximate decorrelation time of precipitation due to differential motion of the particles, is ~10 ms. A rate 50 times slower than the 5 kHz PRF assumed above. So either much longer integration time is required, or each radar has to be equipped with frequency agility to force decorrelation by shifting the operating frequency by at least the transmitted pulse bandwidth [25]. Even if all these obstacles are overcome, what frequency combinations and what weather conditions would have 1 dB/km or greater differential attenuation?

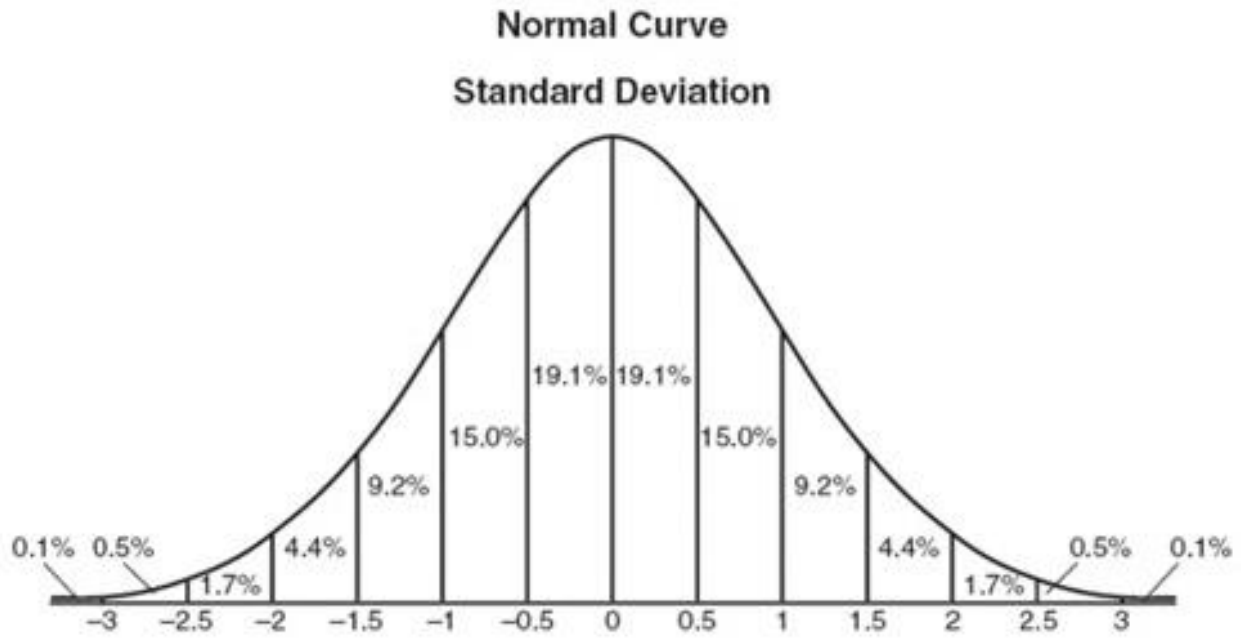

Figure 49. Gaussian distribution as a function of standard deviation, σ. The $\pm\sigma$ interval corresponds to about 68% of the samples, while $\pm 2\sigma$ corresponds to 95% and $\pm 3\sigma$ to 99.7%.

The cloud, drizzle and rain model established in Section 4.1.8 is used again to investigate differential attenuation of various frequency combinations. The results are shown in Figure 50 through Figure 52.

Only the heavier rain produces a differential attenuation rate more than 1 dB/km at X-C and X-Ku frequency combinations. The X-Ka frequency combination is sufficient in most rain and higher LWC cloud conditions, but attenuation also diminishes the sensitivity of a Ka-band radar at longer ranges as shown in Figure 50 and Figure 51.

We can conclude that useful differential reflectivity measurements are quite difficult. The differential attenuation needs to be quite high, often resulting in impractically short maximum detection range at the attenuating frequency, a large number of independent samples are required, and the resulting retrievals have coarse range resolution.

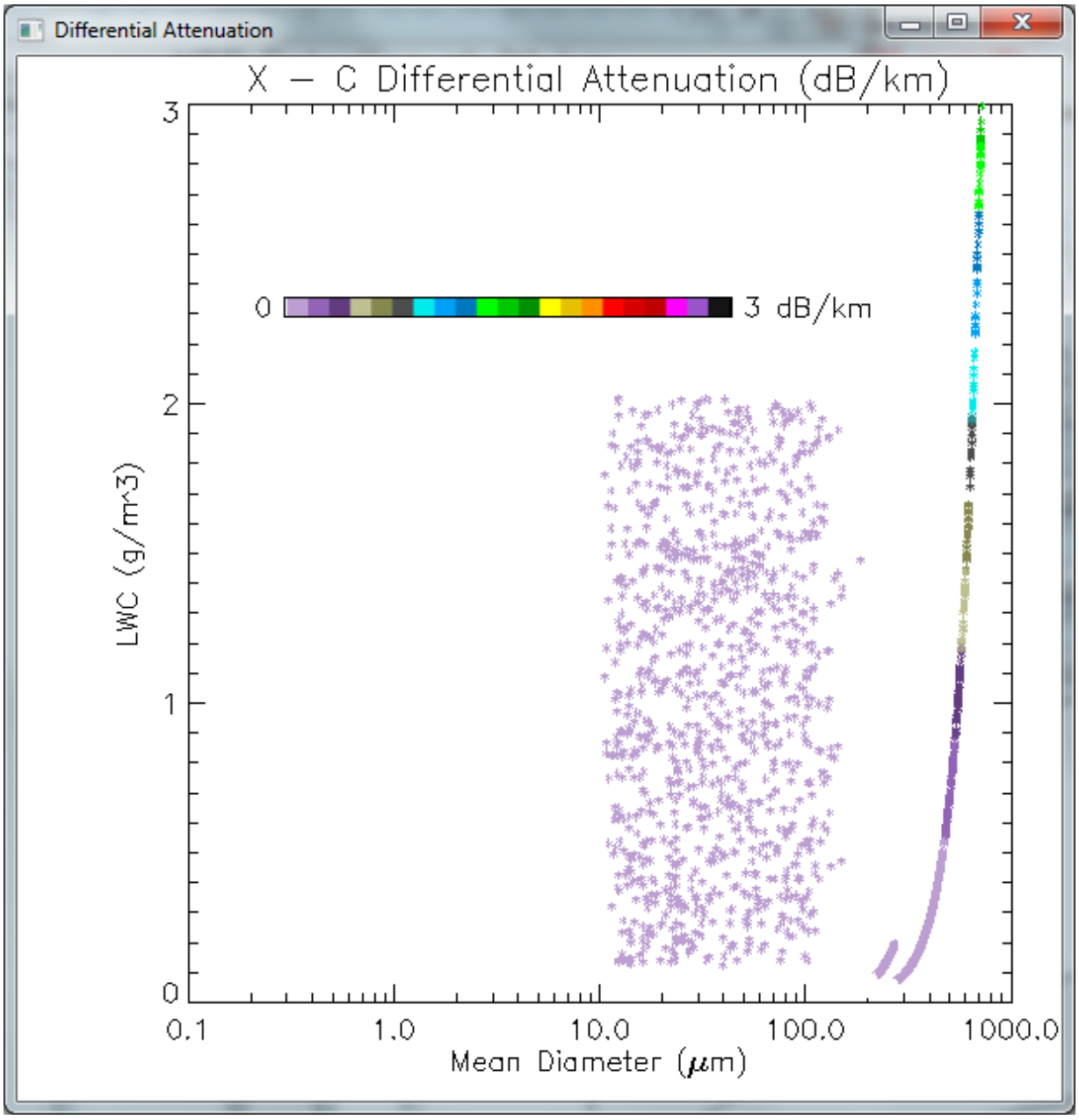

Figure 50. X vs. C-band differential attenuation for a range of cloud, drizzle and rain conditions.

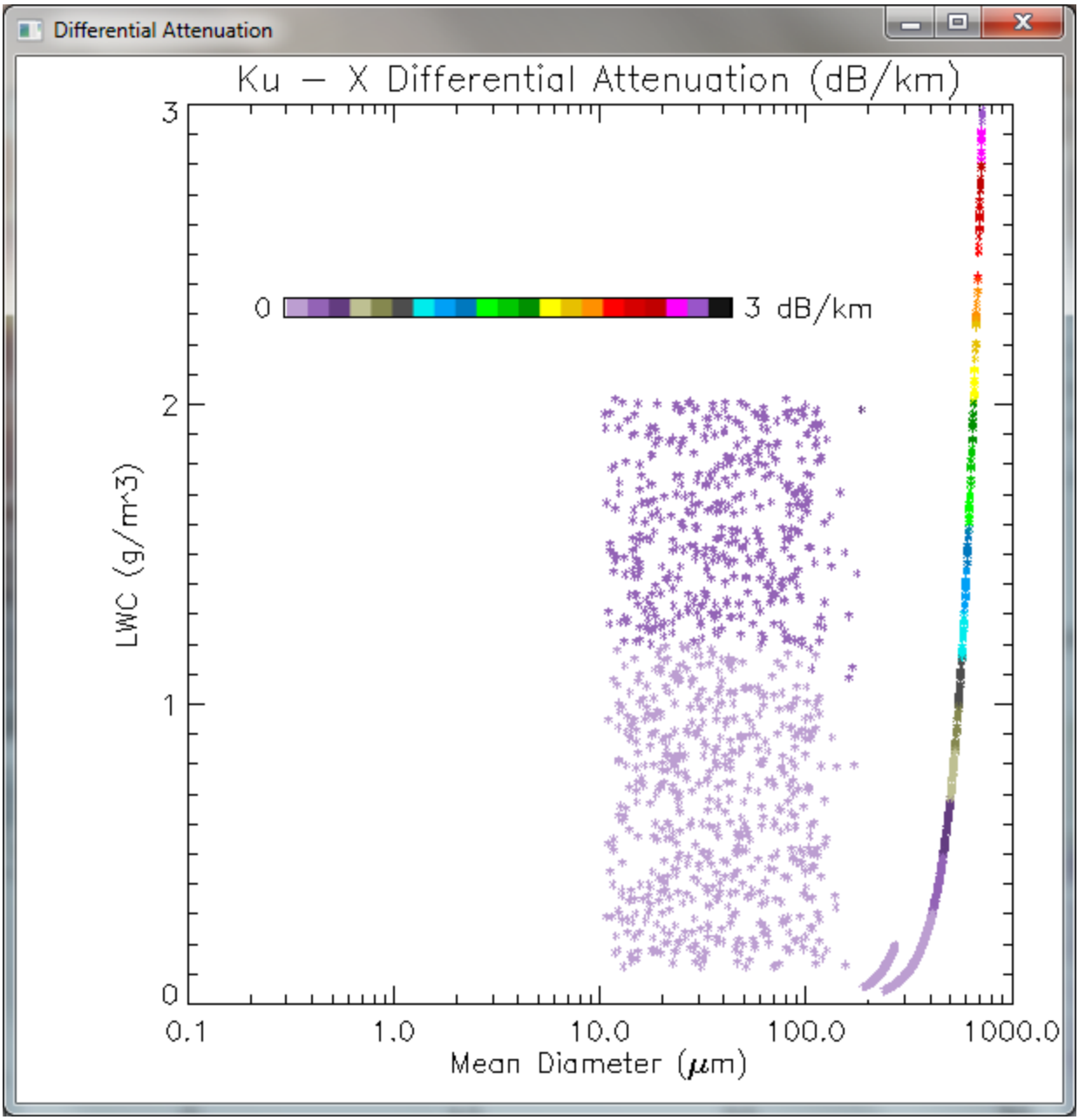

Figure 51. Ku-X differential attenuation estimates are less than 0.5 dB/km for clouds and drizzle, and only reach 2 dB/km in the heavier rain conditions. More frequency separation is needed for MFR retrieval.

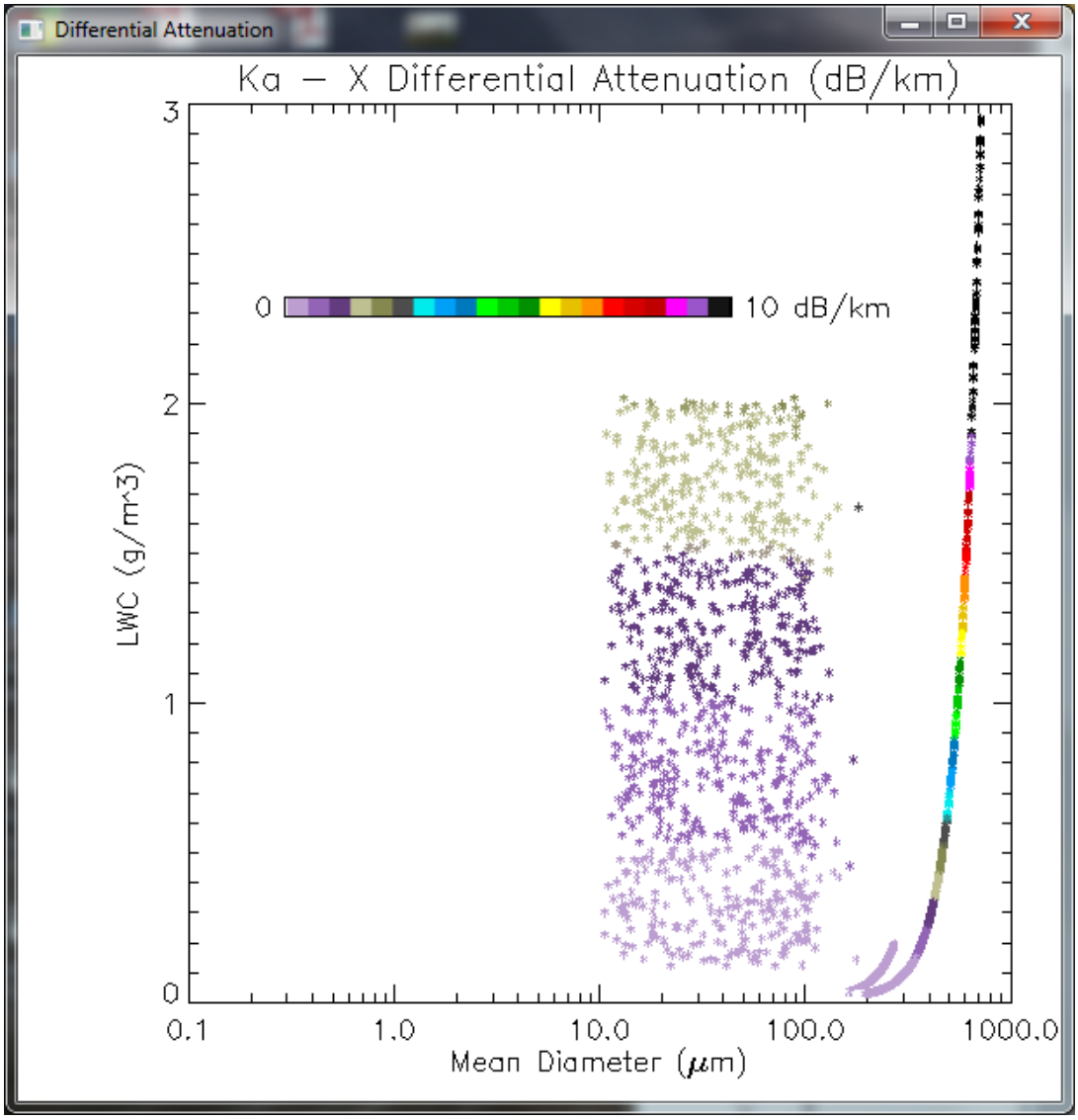

Figure 52. Ka-X Differential attenuation.

5 Sensitivity

A limitation of X-band weather radar is often the lack of sensitivity due to either low scatterer cross section (e.g.: high altitude ice crystals or volcanic ash), high attenuation (severe thunderstorms) or a combination of both (freezing drizzle and rain). The only remedy to attenuation is to shift to a lower frequency, but improving sensitivity through adjusting the radar operating parameters and improved signal processing will always improve the probability of detection. A few of these methods are presented next.

Following is the explanation why the easiest and quickest way to boost the sensitivity of a weather radar is to degrade its range resolution. Low radar cross section is primarily due to the small size of scatterers, but low index of refraction can also be an important factor (glass composite of volcanic ash). From (76), the received power from a volume scatterer can be expressed as:

$$P_r = \frac{P_t A_{eff} c\tau}{32r^2}\eta \quad . \tag{111}$$

The corresponding thermal noise floor, P_n, is:

$$P_n = kTBF = \frac{kTF}{\tau} \quad , \tag{112}$$

where k is Boltzman's constant (1.38E-20 mW/K*Hz), T is temperature is deg. K, F is the receiver noise figure and B is the receiver bandwidth (in units of Hz) matched to the transmit pulse length τ .

Signal to Noise Ratio (*SNR*) is a key factor of detection, in addition to averaging and setting a threshold level to an acceptable probability of false alarm rate. *SNR* is a ratio of the measured signal and receiver thermal noise floor:

$$SNR = \frac{P_r}{P_n} = \frac{\frac{P_t A_{eff} c\tau}{32r^2}\eta}{\frac{kTF}{\tau}} = \frac{P_t A_{eff} c\tau^2 \eta}{32r^2 kTF} \quad . \tag{113}$$

Note the square of the transmit pulse length in the numerator of the expression for *SNR*. This indicates that for a given weather radar with fixed peak transmit power, antenna aperture and noise figure, degrading range resolution, i.e. transmitting longer pulses, is the most effective way to improve sensitivity. *With a receiver bandwidth matched to the transmitted pulse, the measurement signal to noise ratio improves as square of the range resolution.*

Another method of improving sensitivity is through signal processing. In low turbulence regions, a combination coherent (FFT) and non-coherent (power) integration can boost the probability of detection without lowering the false alarm rate. The comparison of conventional non-coherent averaging and a combination of coherent (FFT) and non-coherent averaging is illustrated in Figure 53. A W-band ground-based radar was used to collect data from a non-precipitating cloud on February 9, 2012 in Amherst MA. The radar was configured to transmit at constant PRF and data blocks from 10240 transmit pulses were processed three ways: 1) the top figure shows the combination of FFT and non-coherent averaging, where the 10240 data points where broken up into groups of 128 for FFT processing and the 80 power spectrums where averaged (non-coherently); 2) the middle figure illustrates the conventional power averaging of all 10240 data points and the 3) bottom figure is commonly called *Coherent Power*, generated by forming 620 single lag pulse-pairs and averaging those complex correlations and displaying the magnitude of the resulting average.

The false alarm rates are quite similar in all three methods, but the FFT shows the best detection, followed by the power average and the coherent-power close third. The Coherent Power image could have been improved by forming 10239 pulse pairs from the 10240 pulse train, which likely would have resulted in an image quality similar to that of the power average, but with more uniform false alarm background.

An even better method of detecting weak scatterers is using the Doppler velocity image. Figure 54 shows the same data but processed to velocity using the FFT processing (top) and pulse-pair (bottom). The coherent integration of the FFT processing still has the best detection, but even the pulse-pair velocity image surpasses all three power image detection methods of Figure 53.

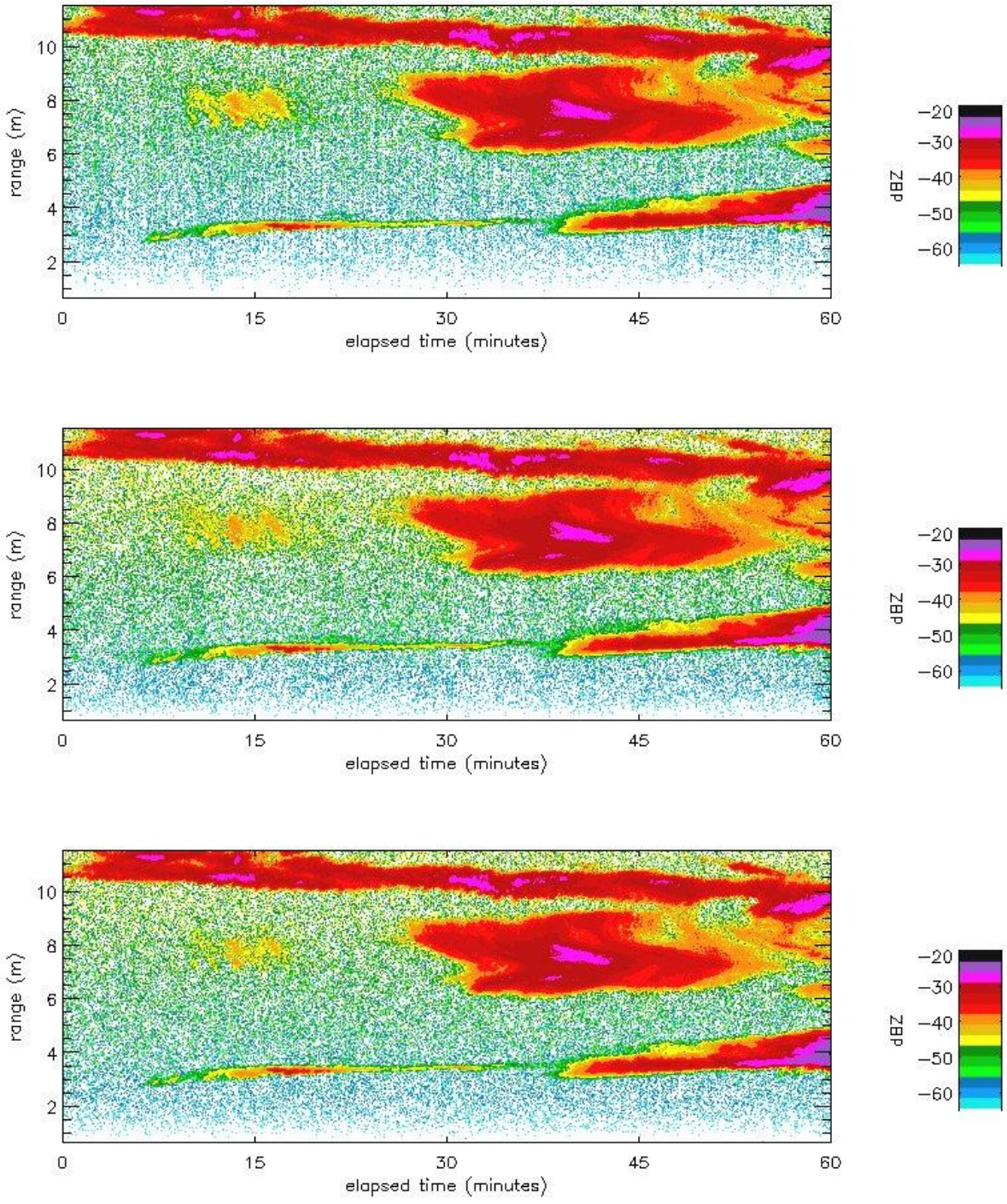

Figure 53. Top: Feb 9 09:00 UTC W-band co-pol FFT-based dBZ (top); non-coherent dBZ (middle); pulse-pair lag 1 dBZ (bottom). Conditions: p_{fa}=0.5; PRF: 4.960 kHz; FFT: N=128; M=80; non-coherent and pulse-pair lag 1: NM=10240. Data gathered at an elevation angle of 145 degrees.

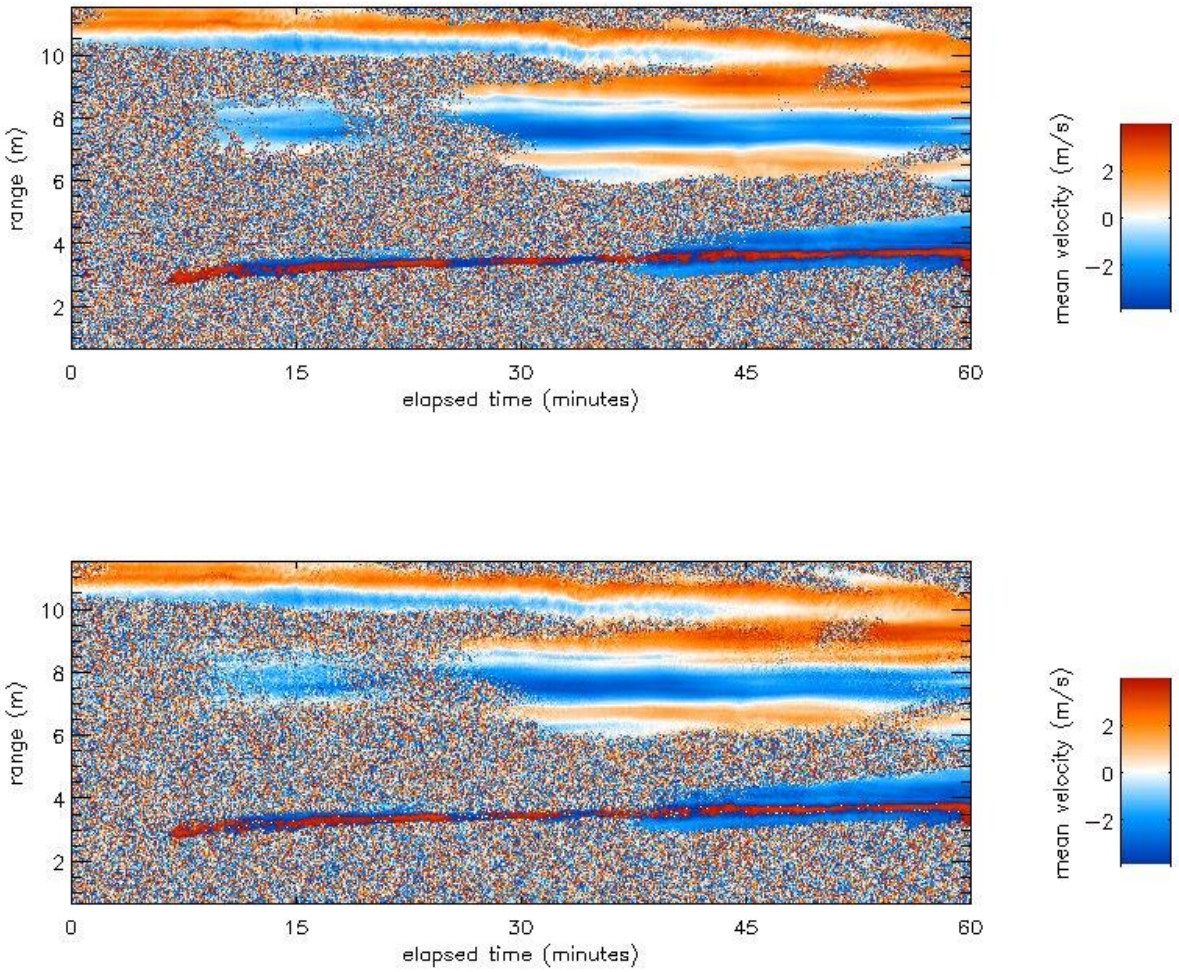

Figure 54. Top: Feb. 9 09:00 UTC W-band co-pol data FFT-based velocity (top); PP velocity (bottom).

6 References

[1] Doviak, R. J., and D. S. Zrnic, **WSR-88D Radar for Research and Enhancement of Operations: Polarimetric Upgrades to Improve Rainfall Measurements** (.pdf, 7.01 MB), NOAA/NSSL Report, 1998, 110 pp., [**Supplements and errata** (.pdf, 156 kB) — updated 7 Aug 2013].

[2] Ryzhkov, A., **Rainfall Measurements with the Polarimetric WSR-88D Radar** (.pdf, 12.1 MB), NOAA/NSSL Report, 2003.

[3] F. Ulaby, R. Moore, A. Fung, Microwave remote sensing: Active and Passive, Vol I, *Microwave Remote Sensing Fundamentals and Radiometry*: Artech House, Dedham MA, 1986.

[4] C. S. Ruf, S. M. Gross, S. Misra, "RFI Detection and Mitigation for Microwave Radiometry With an Agile Digital Detector, IEEE Trans. Geosci. Remote Sens., vol. 44, no.3, pp.694-706, Mar. 2006.

[5] Goodberlet, M.A. and I. Popstefanija, "RFI Mitigation Using Two-Scale Estimators for Statistical Variance," *IEEE Trans. Geosci. Remote Sens. Letters*, Vol. 10(4), Jul. 2013.

[6] G. Mie, *Ann. Physik.*, 25, pp. 377-445, 1908.

[7] "Rain" at http://en.wikipedia.org/.

[8] *Specific attenuation model for rain for use in prediction methods*, Recommendation ITU-R P.838-3, International Telecommunications Union (ITU), 2005.

[9] C. Balanis, *Antenna Theory: Analysis and Design*, Chap 1: Harper & Row Publishers, New York, 1982.

[10] Anagnostou, M.N., et al., "Performance evaluation of high-resolution rainfall estimation by X-band dual-polarization radar for flash flood applications in mountainous basins," *J. Hydrol.*, 2010, doi:10.1016/j.jhydrol.2010.06.026.

[11] Park, S.-G., Maki, M., Iwanami, K., Bringi, V.N., Chandrasekar, V., "Correction of radar reflectivity and differential reflectivity for rain attenuation at X band. Part I: theoretical and empirical basis," *J. Atmos. Ocean. Technol.*, 22, 1621–1632, 2005.

[12] Delrieu, G., H. Andrieu and J. Creutin, "Quantification of Path-Integrated Attenuation for X- and C-Band Weather Radar Systems Operating in Mediterranean Heavy Rainfall," *J. of App. Meteor*, Vol. 39, pp. 840-850, 1999.

[13] Matrosov, S., C. A. Clark, and D. A. Kingsmill,, "A polarimetric radar approach to identify rain, melting-layer, and snow regions for applying corrections to vertical profiles of reflectivity," *J. Appl. Meteor. Climatol.* , 46, 154–166 2007.

[14] Matrosov, S. "Evaluating Polarimetric X-Band Radar Rainfall Estimators during HMT," *J. Tech.*, Vol. 27, pp 122-134, 2010.

[15] Matrosov, S.Y., Kingsmill, D.E., Martner, B.E., Ralph, F.M., "The utility of X-band polarimetric radar for quantitative estimates of rainfall parameters," *J. Hydrometeorol.*, 6, 248–262, 2005.

[16] Matrosov, S.Y., K. A. Clark, B.E., Martner, A. Tokay, F, "X-Band Polarimetric Radar Measurements of Rainfall," *J. Applied Meteor.*, 6, 941–952, 2002.

[17] Matrosov, S.Y., R. A. Kropfli, R. F. Reinking, B. E. Martner, "Prospects for Measuring Rainfall Using Propagation Differential Phase in X- and Ka-Radar Bands," *J. Atmos. Ocean. Technol.*, 38, 766–776, 1999.

[18] Bringi, V. N., and V. Chandrasekar, *Polarimetric Doppler Weather Radar*: Cambridge University Press, 636 pp, 2001.

[19] Zhao et al., "Improving the rainfall rate estimation in the midstream of the Heihe River Basin using raindrop size distribution," *Hydrol. Earth Syst. Sci.*, 15, 943–951, 2011.

[20] Tobias Otto: “Advances in polarimetric X-band weather radar,” Power Point Presentation, 2012. Available http://ieeexplore.ieee.org/.

[21] Wang, Yanting and V. Chandrasekar, “Polarization Isolation Requirements for Linear Dual-Polarization Weather Radar in Simultaneous Transmission Mode of Operation,” *IEEE Trans. Geosci. Remote Sensing*, 44, 2019–2028, 2006.

[22] Anagnostou, M.N., Anagnostou, E.N., Vivekananda, J., “Correction for rainpath specific and differential attenuation of X-band dual-polarization observations,” *IEEE Trans. Geosci. Remote Sensing*, 44, 2470–2480, 2006.

[23] Gorgucci, E., Scarchilli, G., Chandrasekar, V., Bringi, V.N., “Rainfall estimation from polarimetric radar measurements: composite algorithms immune to variability in raindrop shape–size relation,” *J. Atmos. Ocean. Technol.*, 18, 1773–1786, 2001.

[24] Ulaby, More and Fung, *Microwave Remote Sensing*, Artech House, 1989.

[25] Doviak and Zrnic, *Doppler Radar and Weather Observations*, Academic Press, 1984.

[26] Yu-Jiun Ren and Yan Zhang, “Ultra-lightweight dual-polarized X-band array antenna for airborne weather radar applications,” *Microwave and Optical Technology Letters*, May 2009, Vol. 51, Issue 5, pp. 1324–1326, May 2009.

REPORT DOCUMENTATION PAGE

Form Approved
OMB No. 0704-0188

1. REPORT DATE *(DD-MM-YYYY)*	2. REPORT TYPE	3. DATES COVERED *(From - To)*
01- 08 - 2014	Contractor Report	

4. TITLE AND SUBTITLE

Investigation of Advanced Radar Techniques for Atmospheric Hazard Detection With Airborne Weather Radar

5a. CONTRACT NUMBER

5b. GRANT NUMBER

5c. PROGRAM ELEMENT NUMBER

6. AUTHOR(S)

Pazmany, Andrew L.

5d. PROJECT NUMBER

5e. TASK NUMBER

NNL12AA44C

5f. WORK UNIT NUMBER

648987.02.04.07.22

7. PERFORMING ORGANIZATION NAME(S) AND ADDRESS(ES)

NASA Langley Research Center
Hampton, Virginia 23681

8. PERFORMING ORGANIZATION REPORT NUMBER

9. SPONSORING/MONITORING AGENCY NAME(S) AND ADDRESS(ES)

National Aeronautics and Space Administration
Washington, DC 20546-0001

10. SPONSOR/MONITOR'S ACRONYM(S)

NASA

11. SPONSOR/MONITOR'S REPORT NUMBER(S)

NASA/CR-2014-218510

12. DISTRIBUTION/AVAILABILITY STATEMENT

Unclassified - Unlimited
Subject Category 06
Availability: NASA CASI (443) 757-5802

13. SUPPLEMENTARY NOTES

Langley Technical Monitor: Robert T. Neece

14. ABSTRACT

In 2013 ProSensing Inc. conducted a study to investigate the hazard detection potential of aircraft weather radars with new measurement capabilities, such as multi-frequency, polarimetric and radiometric modes. Various radar designs and features were evaluated for sensitivity, measurement range and for detecting and quantifying atmospheric hazards in wide range of weather conditions. Projected size, weight, power consumption and cost of the various designs were also considered. Various cloud and precipitation conditions were modeled and used to conduct an analytic evaluation of the design options. This report provides an overview of the study and summarizes the conclusions and recommendations.

15. SUBJECT TERMS

Aircraft icing; Multi-frequency radar; Polarimetric; Radar; Radiometry; Weather radar

16. SECURITY CLASSIFICATION OF:			17. LIMITATION OF ABSTRACT	18. NUMBER OF PAGES	19a. NAME OF RESPONSIBLE PERSON
a. REPORT	b. ABSTRACT	c. THIS PAGE			STI Help Desk (email: help@sti.nasa.gov)
					19b. TELEPHONE NUMBER *(Include area code)*
U	U	U	UU	90	(443) 757-5802